

The Effect of Liquid Crystal Inclusions on the Mechanical Properties of Liquid Crystal Elastomers

by

Sahad Vasanji

A thesis

presented to the University of Waterloo

in fulfillment of the

thesis requirement for the degree of

Master of Applied Science

in

Chemical Engineering

Waterloo, Ontario, Canada, 2024

© Sahad Vasanji 2024

Author's Declaration

I hereby declare that I am the sole author of this thesis. This is a true copy of the thesis, including any required final revisions, as accepted by my examiners.

I understand that my thesis may be made electronically available to the public.

Abstract

The synergy between materials with differing mechanical properties is an evolutionary adaptation for survival that pervades all of biology. Recognizing these masterstrokes of the natural world has inspired composite materials that enhance all aspects of quality of life. Composite design is particularly important for soft robots, which have advantages over their rigid-bodied counterparts for precision medicine, aquatic locomotion, and human interaction broadly. The relatively inferior mechanical properties of contemporary soft robots are not yet sufficient to replace hard-bodied robots and must be enriched for high load-bearing situations. Liquid Crystal Elastomers (LCEs) hold much promise as a candidate material for soft robotic bodies due to their rapid and reversible stimuli-responsive shape change. Solid fillers, interpenetrating polymer networks, and microstructural modulation have been employed to stiffen and toughen LCEs, yet these strategies substantially hinder extensibility or the liquid crystalline (LC) order. Liquid metal inclusions have recently been harnessed to profoundly increase the elastic modulus and toughness, though the isotropic droplets still compromise LC order. Ever elusive is a method for amplifying mechanical properties that elevate LC order without substantially compromising extensibility.

In this thesis, a stiffened and toughened LCE composite is developed by doping with low molecular weight liquid crystal solvents. First, the influence of the nematogen 4-cyano-4'-pentylbiphenyl, 5CB, is studied. Through miscibility, thermal, and crystallographic studies, the enhanced mechanical properties are shown to emanate from strain-induced short-range smectic order (i.e., cybotacticity) and nanoscale phase separation of the LC solvent from the matrix. Uniquely, cybotacticity arises from components possessing no individual smectic ordering. Improvements of 570% and 370% in stiffness and toughness are conferred and extensibility only decreases by 20%. The first study is built upon by examining LCE modification with the smectogen 8CB (4-cyano-4'-octylbiphenyl). Markedly larger improvements are displayed in the stiffness (760%) and toughness (415%) while retaining 90% of the neat LCE's elasticity. Strain-induced charge transfer is discovered as another factor responsible for the improved mechanical properties. Designing a stiffer, tougher, and lighter LCE with anisotropic liquids will facilitate the development of more effective soft actuators and attract more interest to the theory and application of liquid inclusion stiffening.

Acknowledgments

I would like to thank my supervisor, Professor Hamed Shahsavan for his guidance through this eclectic project, and for the opportunity to set up his laboratory from scratch. I will always be grateful for these experiences. Thank you to Professors Elisabeth Prince and Milad Kamkar for serving as my examiners and for your insightful questions and feedback.

Without our collaborators, this work would not have been possible. From Kent State University, Professor Antal Jakli and Professor Marianne Prevot provided instrumental insight and access to the X-ray Scattering facilities. Dr Arwa Alyami, thank you for all your effort in performing WAXS measurements and discussion on the experimental setup. Within Waterloo, I also received plenty of support. Professor Mekonnen was kind enough to provide access to the DMA, and Binh Minh Trinh provided the training and troubleshooting insight. Professor Parsin Haji-Reza kindly permitted access to all optics tools for measuring transmission, and Dr. Channprit Kaur was invaluable in sharing her expertise on optics theory, laser alignment, and experimental setup. I am grateful to Charles Dal Castel for his discussions on FTIR and DSC studies, and for his help in performing SEM analysis. I am indebted to Pranav Gavirneni for performing SEM in the Giga-to-Nanoelectronics Lab. From the SMART-Lab, Rasool Nasserri often gave his time and knowledge in miscibility characterization and phase behavior. It was also a pleasure having such nice people to work alongside in the lab.

I am grateful to have had a remarkable social support system to lean on in KW. Rebecca, Jon, and Michelle—just as with airplanes, green gift bags, and meteors, great things often come in trifectas. Yasaman, you were welcome company during the late nights in the lab. Thank you Andrée for your energy these past two years. I have also been privileged to receive mentorship from Professor Joanna Aizenberg, Dr. Amos Meeks, Professor Genki Yoshikawa, and Dr. Kota Shiba, who helped spur this academic journey.

Finally thank you to my family—Adeem, dad, and mom—and Karina for your ever-present support throughout the journey.

Dedication

Dedicated to Adeem, Muneerah, Shaynoor, and Karina for all their love.

Table of Contents

Author’s Declaration.....	ii
Abstract	iii
Acknowledgments	iv
Dedication.....	v
List of Figures.....	ix
List of Tables	xi
Chapter 1 Introduction	1
1.1 Motivation	1
1.2 Research Objective and Thesis Outline	2
Chapter 2 Background	4
2.1 Liquid Crystals	4
2.1.1 Common Mesophases	5
2.1.2 Properties of Liquid Crystals.....	7
2.2 Liquid Crystal Elastomers (LCEs)	8
2.2.1 Thiol-Acrylate Liquid Crystal Elastomers.....	10
2.3 Conventional Methods of Stiffening and Toughening LCEs	12
2.3.1 Stiffening with Solid Fillers	12
2.3.2 Interpenetrating Polymer Networks.....	13
2.3.3 Phase Modulation	14
2.3.4 Stiffening with Liquid Inclusions	15
2.4 Cyanobiphenyls.....	16
Chapter 3 Materials and Methods.....	17
3.1 Materials.....	17

3.2 Methods.....	17
3.2.1 LCE Synthesis.....	17
3.2.2 Miscibility.....	19
3.2.3 Thermal Analysis.....	23
3.2.4 X-Ray Diffraction.....	24
3.2.5 Mechanical Tests.....	25
Chapter 4 Nematogen Loaded Liquid Crystal Elastomers.....	28
4.1 Design Considerations.....	28
4.1.1 LCE Selection.....	28
4.1.2 Dopant Selection.....	28
4.2 Results and Discussion.....	28
4.2.1 Polymerization with 5CB.....	28
4.2.2 Miscibility.....	29
4.2.3 Thermal Analysis.....	37
4.2.4 Determining the Mesophase Nature.....	47
4.2.5 Nanoscale Order Influence on Mechanical Properties.....	59
4.3 Conclusions.....	67
Chapter 5 Smectogen Loaded Liquid Crystal Elastomers.....	69
5.1 Polymerization with 8CB.....	69
5.2 Selection of Dopant Loading: Optimal Mechanical Properties.....	70
5.3 Miscibility.....	72
5.3.1 Swelling.....	72
5.3.2 8CB Surface Energy and Group Contribution Theory.....	73
5.3.3 Cross-Sectional Cryo-SEM.....	73

5.4 Thermal Analysis	75
5.4.1 Differential Scanning Calorimetry (DSC)	75
5.4.2 Dynamic Mechanical Analysis (DMA)	76
5.4.3 Coefficient of Thermal Expansion.....	78
5.5 Investigating 8CB's Endowed Microstructure.....	79
5.5.1 WAXS and Order Parameter.....	80
5.5.2 D-Spacings and Correlation Length.....	82
5.5.3 FTIR-ATR	84
5.5.4 Size of Phase Separated Domains.....	86
5.6 Bulk Mechanical Properties.....	87
5.6.1 Polydomain Tensile Property Evolution with Time.....	88
5.6.2 Polydomain-Monodomain Alignment Onset	89
5.6.3 Monodomain Tensile Tests.....	91
5.7 Conclusions	92
Chapter 6 Conclusion and Outlook	93
6.1 Conclusion.....	93
6.2 Outlook	94
References	95

List of Figures

Figure 2-1: Molecular organizations for a) Crystalline Solid, b) Smectic A, c) Smectic C, d) Nematic, and e) Isotropic (liquid) phases.	6
Figure 2-2: Molecular Structure of 5CB, 8CB and 10CB	7
Figure 2-3: Properties of Liquid Crystal Elastomers. a) Order-disorder transition induced deformation, b) soft elasticity, c) programming methods, d) mesogen connectivity (green: Main Chain, purple: mesogenic crosslinker, yellow: end-on side chain, brown: side-on side chain).....	10
Figure 2-4: Dipropylamine catalyzed Thiol-Michael addition mechanism.....	11
Figure 2-5: Polydomain tensile data for composites comprised of main-chain nematic LCEs and side-chain smectic-LCEs.....	15
Figure 3-1: LCE Synthesis Schematic. A) Monomers and LC solvent structures, B) Polydomain LCE Chain Conformation, C) Monodomain (Aligned) LCE.	18
Figure 3-2: Microscopy Setup for Swelling and Dopant Leakage.	20
Figure 3-3: Goniometer setup. From left to right: light source, stage, dispensing syringe, camera.	21
Figure 3-4 Diagram (left) and Picture (right) of Transmission Measurement Setup. The power meter is to the right of the tensile apparatus (not pictured).	27
Figure 4-1: Initial and Swollen m_0 in 5CB. (Graph paper square edges are 3mm).	30
Figure 4-2: Initial and Final Dimensions of M5CB70 after 33 hours.....	31
Figure 4-3: 5CB Contact Angle Measurement.....	32
Figure 4-4: SEM of Samples without any extraction performed.	36
Figure 4-5: DSC Heating Cycle for 5CB Formulations. Endothermic transitions are labeled above their peaks. Cold crystallization is denoted with a dashed line.....	38
Figure 4-6: DSC Cooling Cycles for 5CB Formulations. Endothermic transitions are labeled below their peaks. 5CB's transitions are denoted with dashed lines.....	39
Figure 4-7: 5CB Formulations' Storage Moduli as a function of temperature.....	41
Figure 4-8: $\tan\delta$ for p0, p5CB10, and p5CB30 with labeled T_g , T^* and T_{NI}	42
Figure 4-9: $\tan\delta$ for p5CB50 and p5CB70 with labeled T_g and T^*	42
Figure 4-10: $\tan\delta$ and Normalized Amplitude for a) p5CB30, b) p5CB50, c) p5CB70	43
Figure 4-11: Thermal Expansion of m_0	45
Figure 4-12: Thermal Expansion of m5CB10.....	45
Figure 4-13: Thermal Expansion of m5CB30.....	46

Figure 4-14: Thermal Expansion of m5CB50.....	46
Figure 4-15: Thermal Expansion of m5CB70.....	47
Figure 4-16: 2D Diffraction Patterns for 5CB Doped LCEs.	50
Figure 4-17: 1D Integrated Intensities for 5CB Loadings.....	51
Figure 4-18: Representative Transverse Correlation Length due to Nematic Ordering.	53
Figure 4-19: Phase-separated 5CB domain dimensions in p5CB30 polydomain (Left) and monodomain (Right) LCEs.....	58
Figure 4-20: Five Day Tensile Data of p0.....	60
Figure 4-21: Five Day Tensile Data of p5CB10.	60
Figure 4-22: Five Day Tensile Data of p5CB30.	61
Figure 4-23: Five Day Tensile Data of p5CB50.	61
Figure 4-24: Five Day Tensile Data of p5CB70.	62
Figure 4-25: Overlaid Stress-Strain Data of all Polydomain 5CB Formulations.	63
Figure 4-26: Transmission Coefficient Evolution with Strain.....	65
Figure 4-27: Monodomain Tensile Data for LCEs stretched a) Parallel and b) Perpendicular to the programmed Director.....	66
Figure 5-1: Polydomain Tensile test of 8CB-doped Formulations.....	71
Figure 5-2: Digital Microscope Images of m0 before (left) and after (right) immersion in 8CB.	72
Figure 5-3: Heating and Cooling Cycles of a) p0, b) p5CB30, and c) p8CB30.....	75
Figure 5-4: p0, p5CB30, p8CB30 temperature dependent storage moduli.	77
Figure 5-5: p0, p5CB0, and p8CB30 $\tan\delta$ with labeled T_g , T^* , T_{NL}	78
Figure 5-6: Thermal Expansion Graphs for 5CB0, m5CB30, and m8CB30 formulations. Length changes parallel (perpendicular) to the director are denoted as negative (positive) strains.	79
Figure 5-7: 2D Diffraction Patterns and 1D Radially Integrated Curves for p0, p5CB30, p8CB30. ...	81
Figure 5-8: FTIR Spectra of a) Polydomain and b) Stretched to monodomain p0, p5CB30, p8CB30. 85	
Figure 5-9: Strain-induced molecular packing schematic for p8CB30.....	87
Figure 5-10: Five Day Polydomain Tensile Data of p8CB30.....	88
Figure 5-11: Polydomain Tensile Data form Day 5 for p8CB30, p5CB30, p0.....	89
Figure 5-12: Strain Dependence of Transmission Coefficient. Solid (dashed) lines show the parallel (perpendicular) coefficients.....	90
Figure 5-13: Monodomain Tensile Curves for m8CB30, m5CB30, m0.....	91

List of Tables

Table 3-1: Naming convention of all synthesized formulations based on their alignment, dopant, and dopant concentration.....	19
Table 4-1: Solvent Contact Angles with LCE	32
Table 4-2: Solubility Parameters and Differences for 5CB and the LCE	33
Table 4-3: SEM of Samples that underwent extraction.	37
Table 4-4: Transition Temperatures from DSC Heating and Cooling Cycles	39
Table 4-5: Transition Temperatures from DMA.....	44
Table 4-6: Order Parameters of 5CB-doped LCEs.....	52
Table 4-7: D-spacings (d) and Correlation Lengths (ξ) for p_1 and p_3	55
Table 4-8: Comparison of Moduli between P0 and P5CB30. The failure strains for p_0 and p_5 CB30 are 370% and 297%, respectively.....	63
Table 5-1: Solubility Parameters for 5CB, 8CB, and the LCE.....	73
Table 5-2: SEM Images of p_8 CB30 and p_8 CB70 cross-sections at 500 \times and 1000 \times magnification...	74
Table 5-3: Transition Temperatures of p_8 CB30 and p_5 CB30	75
Table 5-4: Transition Temperature Comparison for p_8 CB30 and p_5 CB30	78
Table 5-5: Strain-Dependent Order Parameters for p_0 , p_5 CB30, and p_8 CB30.	82
Table 5-6: D-spacing and Correlation Length Comparison for p_8 CB30, p_5 CB30, p_0	83

Chapter 1

Introduction

1.1 Motivation

Automation in the form of robotics has become indispensable in decreasing healthcare wait times, whether it is through mitigating personnel burnout or improving myriad medical procedures (1, 2). Particularly in precision medicine, large robotic systems such as Da Vinci or NeuroArm have surpassed human capabilities and successfully performed millions of surgeries (3, 4).

Medical robots of the 21st century are hard-bodied machines composed of contemporary rigid mechanical joints and linkages. Consequently, they are expensive, bulky, and possess limited degrees of freedom (5, 6). Such anatomies also bring a greater risk of inadvertent patient harm due to mechanical mismatch between their metal components and soft bodily tissues (6). Drawing inspiration from evolutionary adaptations sparked the development of soft robots, whose bodies are comprised of soft and continually deformable materials. Soft robots have emerged as a next-generation solution to overcome the detriments inherent to hard-bodied robots (5, 6). The principal drawback of soft robots is their comparatively weaker mechanical properties which are requisites for performing effective work (6, 7). As such, the development of a soft robotic actuator (SRA) is necessary to initiate this paradigm shift from conventional robots to soft robots in medical practices.

One of the most promising classes of materials for SRAs is Liquid Crystal Elastomers (LCEs). This is because, compared to other materials, they are easier to program with large, fast, and directional deformation that can be controlled through many stimuli (8, 9). Such desirable properties are due to the coupling between the monomers' liquid crystalline order, and the network's elasticity (10). Moreover, LCEs have a facile synthesis, such as those based on thiol-Michael click chemistry which reaches high conversions and has low environmental sensitivity (10, 11). Strategies to improve LCE mechanical properties have involved incorporating liquid metals, solid fillers, interpenetrating polymer networks, and crystallization (12–15). While these stiffen or toughen the LCE, they substantially impede the phenomena underscoring the ability to program in deformation, often resulting in decreased actuation strain. What remains elusive is a stiffened LCE whose programmability and extensibility are not substantially compromised compared to the base formulation.

An exciting new method of stiffening soft materials has been to incorporate immiscible liquid droplets—liquid inclusions—with sizes below a characteristic length scale relating the dopant's surface

tension to the host solid's elastic modulus (16). Considering this work was conducted with droplets within an isotropic solid, of interest to the scientific community was whether this stiffening method functions for anisotropic solids such as LCEs. Doping LCEs with immiscible liquid metal droplets produced instances of stiffening 22-fold or toughening 61-fold (12, 17). However, metal-polymer physical interactions also contributed to the enhancements alongside liquid inclusion stiffening. Additionally, the material properties engendering programmability were still substantially compromised as evidenced by actuation strains below 55% (12, 17). The enhanced LCE without substantially compromised actuation strain remained elusive.

1.2 Research Objective and Thesis Outline

This thesis' objective is to study the question, "Can a substantially stiffened LCE be developed using the liquid inclusion method?" It is hypothesized that the design of such an LCE is realizable by employing an anisotropic liquid dopant such as a liquid crystal solvent. This is because low molecular weight LC solvents are known to phase separate out from LCEs during the polymerization (18). Such a process may generate liquid crystal inclusions. Further, it is anticipated that the LC solvent facilitates chain movement with less resistance, mitigating adverse effects on failure strain (19). The research question is first approached by judiciously selecting a candidate solvent and LCE chemistry, followed by investigating the dopant's incorporation within the network and determining an optimal loading. Next the dopant's impact on the LCE's microstructure is elucidated and the theory of liquid inclusion stiffening is addressed. Subsequently, the resultant stiffness and toughness are studied. Secondly, a dopant with a similar structure to the first but possessing more molecular order is introduced, and the same procedural study is conducted.

The structure of the following chapters is herein outlined. Chapter 2 summarizes the properties and applications of liquid crystals and liquid crystal elastomers, followed by detailing methods of improving LCE mechanical properties. This Chapter's last section introduces cyanobiphenyl liquid crystals as a candidate dopant for stiffening. Chapter 3 documents the utilized materials and exercised experimental methods. Chapter 4 commences with the design choices of dopant and LCE, and then discusses the dopant's modulation of the LCE's thermally dependent properties. The nanoscale structure is probed through X-ray analysis to fully elucidate the molecular order, and the Chapter concludes with the dopant's impact on bulk mechanical properties. Chapter 5 studies the same methods as Chapter 4 but

for an LCE loaded with a dopant possessing a more ordered mesophase. Finally, Chapter 6 presents the concluding remarks.

Chapter 2

Background

2.1 Liquid Crystals

The Liquid Crystal (LC) phase is a physical state of matter possessing properties of both solids and liquids. Consider the ordering of molecules in a solid. All molecules exist in a defined arrangement and are oriented in a particular direction—they have high degrees of positional order and orientational order, respectively (20, 21). Possessing both types of order results in strong attractive interactions that maintain the solid structure since these forces have an additive effect. Consequently, substantial amounts of energy are required to disrupt this arrangement. While this description is most apt for crystalline solids, amorphous solids also are comprised of molecules loosely fixed in place, but an overall lattice arrangement of molecules is not observed.

Consider, however, the converse example, of a liquid, where molecules are not constrained to a lattice structure—they are free to diffuse through the bulk liquid and occupy any orientation. A liquid consequently displays neither positional nor orientational order. The kinetic energy molecules possess is enough to prevent the attractive forces from summing together, resulting in a liquid being held together by markedly weaker interactions than a solid (20, 21). Weaker bulk interactions signify that less external force is required for a liquid to deform, or flow.

Transitions can be facilitated between the two states by adding kinetic energy to the system or increasing temperature. By elevating the temperature above a conventional solid material's melting point, sufficient kinetic energy is introduced to overcome the intermolecular forces preserving the positional and orientational order of the crystalline lattice, and a liquid phase is generated.

Now the liquid crystal state can be defined. Materials demonstrating a liquid crystal phase, upon heating from the solid state, do not lose all their orientational order and may maintain their positional order. Molecules have enough kinetic energy to flow past one another as in a liquid but still maintain overall alignment in a particular direction just as in a solid (21). While this overall alignment is less than a solid's orientational order, it is sufficiently larger than that of a liquid. LC phases are often observed when a substance becomes cloudy when heated from its solid state while still at temperatures below its melting point (21).

What molecules are most likely to be capable of forming liquid crystal phases? This is predominantly a function of molecular geometry, which can easily be tailored to promote maintaining orientational order but not having as much positional order as a solid phase. Molecules with larger aspect ratios, i.e. having a width or thickness that is notably smaller than its length, tend to self-organize due to the anisotropy of van der Waal forces and form liquid crystal phases (22). Considerable structural integrity is necessary to maintain such large aspect ratios, and this is accomplished by designing molecules to have rigid cores and flexible peripheries. Ubiquitous rigid motifs include directly bound or fused aromatic rings at the core of the molecule since they permit one of the most common forms of anisotropic organization: π - π stacking (23). Concerning the periphery groups, alkyl chains are most frequently used (8). Large aspect ratios are synonymously classified as “geometric anisotropies”. Examples of such geometries include calamitic liquid crystals—or rod-shaped molecules—and discotic liquid crystals—two-dimensional (2D), disk-shaped molecules (20). Both geometries also include multiple aromatic rings, which provide molecular rigidity to beget strong short-range orthogonal ordering and global alignment. Compounds displaying a liquid crystal phase are called mesogens (20).

2.1.1 Common Mesophases

The existence of LC phases can most chiefly depend on temperature (i.e., thermotropic) and concentration (i.e., lyotropic), where modulating these parameters elicits different mesophases (21, 24). For this work, only thermotropic LCs are described. Thermotropic LCs exhibit LC phases, or mesophases, between a certain temperature range. Below this temperature window they adopt a crystalline state, and above a conventional liquid state is observed. Within liquid crystal studies, this conventional liquid state is referred to as the isotropic phase, since all molecules are randomly (i.e., isotropically) oriented. This is because sufficient thermal energy is present to prevent the adoption of a preferred alignment direction. Transitioning from an LC phase to the isotropic phase occurs at a temperature called the clearing point.

Though several thermotropic mesophases exist, the two most common are detailed herein. The nematic phase (N) has only orientational order and no positional order. All molecules are loosely aligned in the same global direction but do not occupy a specific position with respect to their neighbors and can diffuse throughout. More distinctly, nematogenic compounds—those that only adopt a nematic mesophase—are distinguished through their characteristic fan-shaped texture seen under cross-polarizers (20). Cross-polarizers are two linearly polarized films sandwiched above and below the LC

and are oriented at 90° to one another. The Smectic mesophase (Sm) demonstrates both positional and orientational order (25). Positional order is observed whereby molecules arrange themselves in equally spaced planes, though within the two-dimensional (2D) plane no positional order exists. Furthermore, orientational order is observed, where within these layers all molecules are aligned to a higher degree than observed in the nematic phase. Though molecules are free to flow within and amongst the layers, on average the mesogens are within the planes for a longer time interval than between planes and are oriented in the same direction. Smectic mesophases are most easily distinguished by a focal-conic pattern produced under cross-polarizers (20). Smectic A (SmA) and smectic C (SmC) mesophases are two of the most common smectic phases observed (21). For the distinction between these two mesophases, the term “Director” is defined. The director, \mathbf{n} , is the average direction towards which all molecules are oriented; analogously this is considered the preferred direction of alignment. In the Smectic A phase, the director is normal to the layers, and in the Smectic C phase, the director is at a non- 90° angle. Figure 2-1 shows these three mesophases that could exist at temperatures between the solid and (isotropic) liquid phases of matter.

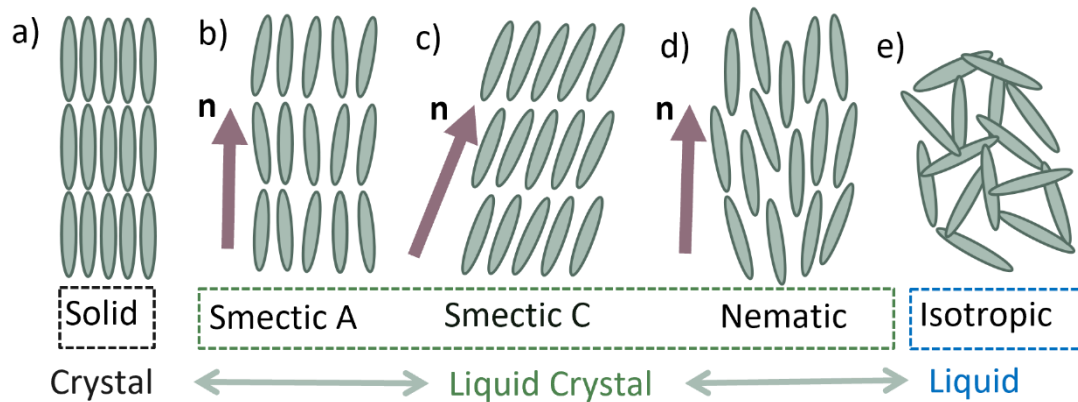


Figure 2-1: Molecular organizations for a) Crystalline Solid, b) Smectic A, c) Smectic C, d) Nematic, and e) Isotropic (liquid) phases.

Thermotropic substances exist that exhibit smectic, nematic, or both phases. Smecticity, or the quality of being smectic, is typically observed at lower temperatures than the nematic phase as the thermal energy must be small enough for intermolecular forces to facilitate the formation of 2D planes. For compounds capable of forming both phases, as the system’s thermal energy, or entropy, increases above a certain temperature more states of molecular organization become available than are present in the smectic temperature window. This coincides with the loss of positional order and transitioning to

the nematic phase. An example of such a material is 4-cyano-4'-octylbiphenyl, also called 8CB. 4-cyano-4'-n-decylbiphenyl, or 10CB, is an exemplar that only displays a smectic mesophase. Finally, a nematogenic example is 4-cyano-4'-n-pentylbiphenyl or 5CB. These three molecular structures are shown in Figure 2-2

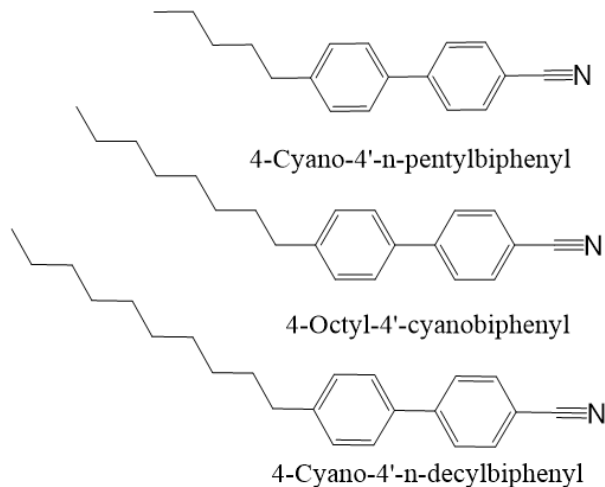


Figure 2-2: Molecular Structure of 5CB, 8CB and 10CB

Transitions to mesophases containing less order are an endothermic process, where energy is inputted to disrupt the lower entropy, higher-order state. A smectic-nematic transition temperature is denoted T_{SN} , and the clearing point (or transitioning to an isotropic liquid) is labeled T_I . In the context of a nematic-isotropic transition, this type of clearing point is labeled T_{NI} . The clearing point is easily observed when the apparently cloudy substance becomes clear, or when the substance appears black under cross-polarizers.

2.1.2 Properties of Liquid Crystals

The large aspect ratios of LCs result in many intriguing anisotropic properties in the viscosity, refractive index, dielectric constant, magnetic susceptibility, light absorbance, and thermal expansion (21, 26). Coupled with the phase dependence on light, concentration, and temperature, these properties contribute to eclectic applications being explored. These include but are not limited to, displays, optics (filters, fiber optics, lasers), biosensors, protein binding, structural color, organic electronics, energy harvesting, templating, textiles, and drug delivery (21, 27–36).

2.2 Liquid Crystal Elastomers (LCEs)

The promise of applying the highly anisotropic material properties of liquid crystals to solids was accomplished through the invention of liquid crystal polymers (LCPs). Jackson and Kuhfuss were the first to design LCPs by introducing p-acetoxybenzoic acid, a molecule with a benzene core and lateral dipoles to promote transverse packing, to poly(ethylene terephthalate) (PET) (37). Such a polymerization strategy resulted in a polymer with large anisotropies in the tensile strength and elongation with the alignment direction as the reference. LCPs also displayed anisotropies in their thermal expansion coefficients and gyration radii (37, 38). Transcending just property anisotropy, it was predicted that by crosslinking individual LCP chains, bulk shape changes could occur when transitioning through the T_{NI} (39). Lightly crosslinked LCPs, termed Liquid Crystal Elastomers (LCEs), were experimentally realized shortly after (40–42). Similarly, by employing a high crosslinking density, Liquid Crystal Networks (LCNs) can also be synthesized, whose mechanical properties closely resemble a glassy polymer (8). While the terms LCEs and LCNs are often used synonymously, for the context of this work, only LCEs will be discussed.

Through the cooperative effects of organizational order and entropic elasticity, which stem from liquid crystals and polymers respectively, LCEs are unique in demonstrating phenomena not displayed by their components (43, 44). Perhaps the most captivating of these behaviors is the fast shape change of several hundred percent, which can occur in response to many stimuli and be programmed via heat, light, magnetism, pH, and chemicals (see Figure 2-3a) (26, 45). This deformation stems from the order-disorder transition occurring at the clearing point where the LCE transitions to the isotropic state, and depends on global mesogen alignment existing below the isotropic region (8). Such a phenomenon has made LCEs extremely attractive as actuators in soft robotics (44, 46–49).

Alongside the large and rapid deformation, LCEs also possess a unique property called “soft elasticity” that is not seen in ordinary elastomers (43). When LCEs are synthesized without any external alignment factors, only local LC domains exist with random orientation (45). This is called a “polydomain” state and is characterized by the LCE being visibly opaque due to the randomly oriented domains scattering light. Soft elasticity is when the LCE elongates with infinitesimal increases in stress beyond a threshold value, which is due to polymerized mesogens in a confined geometry relaxing and reorienting with the strain direction (50). The resultant global alignment of these local domains is termed a “monodomain” state, and the stress-induced reorientation is called the Polydomain-

Monodomain Transition (PMT). The PMT is also characterized by a sharp increase in the order parameter—which measures the overall alignment of all mesogens—and thus the transparency as well (10, 51). A prototypical polydomain LCE tensile response is seen in Figure 2-3b wherein the soft elastic plateau (SEP) is encircled. LCE soft elasticity has found many applications, including as dampers (52).

Mesogens can be oriented into a monodomain state with fields (i.e., electric or magnetic), temperature, mechanical stress, light patterning, surface topography, or flow (Figure 2-3c) (45). Permissible alignment techniques often depend on the LCE polymerization method, which is broadly classified into one or two-step reactions. In single-step schemes, the polymeric chains and permanent crosslinking occur simultaneously, while in the two-step process, a lightly crosslinked LCE is formed in the first reaction and permanent crosslinking takes place in the second step (53). Examples of one-step methods labeled by their reaction chemistry include acrylate homopolymerization, and two-step protocols consist of vinyl-siloxane, epoxide, aza-Michael, and thiol-acrylate reactions (44, 45). Regarding LCE structure, mesogenic groups can be incorporated into the polymer backbone (termed “main-chain”) or as pendant groups (“side-chain”). As another degree of tailoring within side-chain LCEs, the mesogen can be covalently linked to the backbone by the molecule’s end (“end-on side-chain LCP”) or its center (“side-on side-chain LCP”) (53). Finally, they can be employed as chain crosslinkers. These methods of incorporation are shown schematically in Figure 2-3d.

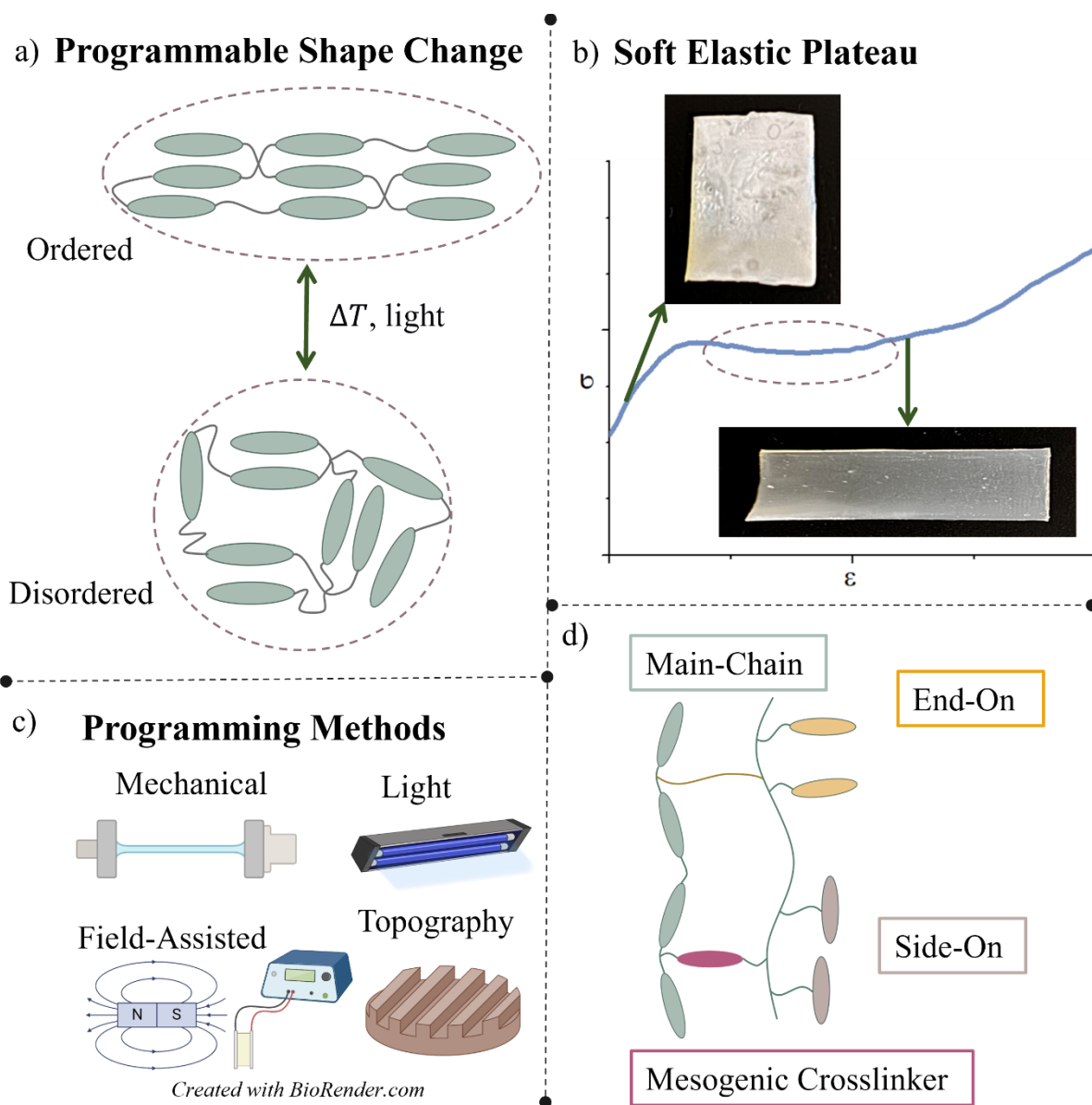


Figure 2-3: Properties of Liquid Crystal Elastomers. a) Order-disorder transition induced deformation, b) soft elasticity, c) programming methods, d) mesogen connectivity (green: Main Chain, purple: mesogenic crosslinker, yellow: end-on side chain, brown: side-on side chain).

2.2.1 Thiol-Acrylate Liquid Crystal Elastomers

One of the most promising LCE chemistries is the thiol-acrylate LCE, which employs an orthogonal two-step protocol consisting of a first-stage thiol-Michael addition, and a second-stage acrylate-acrylate

polymerization (10). This chemistry has a facile synthesis protocol and results in an LCE exhibiting large and fast deformation (10). As reported by Yakacki and colleagues, both reactions are oxygen insensitive, proceed at room temperature, and employ less toxic reagents than other LCE chemistries (10, 54). The first-stage reaction follows a base-catalyzed thiol-Michael addition, which is a click chemistry consisting of three major steps (55).

1. Deprotonation. This is where the base deprotonates the thiol (Michael Donor) to form a thiolate and conjugate acid.
2. Nucleophilic attack. The thiolate attacks the β -carbon of the vinyl group (the Michael Acceptor), producing a thioether bond and intermediate anion.
3. Protonation. The carbon-centered anion, being a strong base, abstracts the proton from Step 1's conjugate acid.

These steps are shown in Figure 2-4 for generic acrylate and thiol monomers with dipropylamine as the base. The thiol-Michael addition proceeds to high conversion and is usually conducted without liquid crystal alignment methods to produce a polydomain LCE. Pertinent chemicals include: dipropylamine as the base catalyst, pentaerythritol tetrakis (3-mercaptopropionate) (abbreviated PETMP) and 2,2'(ethylenedioxy) diethanethiol (abbreviated EDDET) as the thiol reactants, and 1,4-bis-[4-(3-acryloyloxypropoxy)benzoyloxy]-2-methylbenzene (RM257) as the acrylate contributing species. PETMP functions as a crosslinker for forming the polydomain LCE; EDDET is a flexible polymer chain extender; and RM257 is the mesogenic monomer (56).

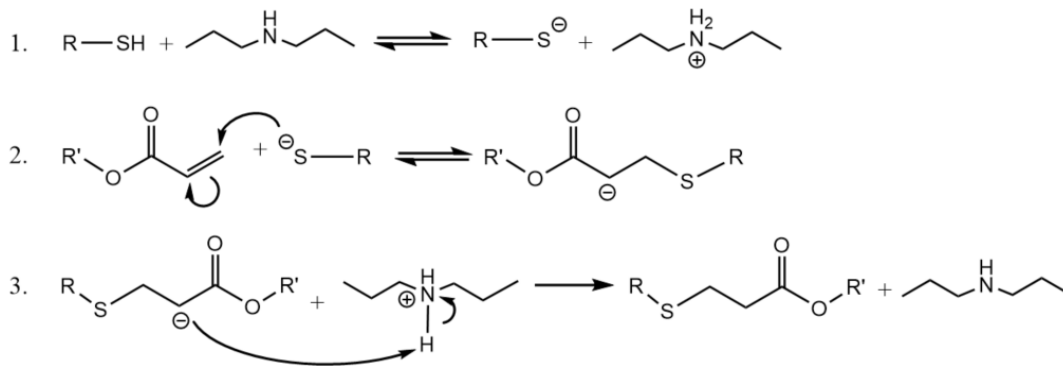


Figure 2-4: Dipropylamine catalyzed Thiol-Michael addition mechanism.

Since RM257 is a mesogenic monomer displaying only nematic and isotropic mesophases, a polydomain nematic LCE is produced at room temperature. Thiol-Acrylate LCEs (abbreviated as

TALCEs) are amenable to many alignment techniques, including mechanically induced mesogen alignment (10, 45). The aligned state can be instilled with the second-stage UV photopolymerization, which is initiated by Irgacure 651 to crosslink unreacted vinyl groups. For the second-stage reaction to take place, RM257 is incorporated in stoichiometric excess such that more acrylate groups are present than thiol moieties.

TALCEs have been designed to display many types of mesophases, including those beyond typical nematic, SmA, and SmC mesophases (45, 57–60). As well, TALCEs have also been tailored to possess responsiveness to several stimuli for applications including color-changing materials, biomedical devices, dynamic adhesion, underwater and multimodal actuators, photochemical and photochemical actuators, and electrothermal actuators (58, 61–68).

2.3 Conventional Methods of Stiffening and Toughening LCEs

As TALCEs have been extensively designed for soft robotics, there is renewed interest in improving their mechanical metrics underscoring actuation (8, 44, 53). These include the elastic modulus (or stiffness in the context of uniaxial strain), toughness, failure strain, work density, work capacity, actuation stress, actuation strain, blocking stress, and storage modulus. Elevating the crosslinking density is one of the simplest modifications to improve the LCE's elastic modulus, however, this produces a commensurate decrease in the material's extensibility (54). As such, more innovative methods to improve the mechanical properties have been studied and are discussed below.

2.3.1 Stiffening with Solid Fillers

Doping with solid fillers is a common strategy for improving the mechanical properties of polymers that can also be applied to LCEs (69). Often this is due to solid fillers suppressing crack propagation and the markedly larger elastic modulus of the dopant (69). Gold Nanorods (AuNRs) were shown by Keller and colleagues to improve the LCE's actuation strain, which is due to the photothermal effect of AuNRs improving the LCE's thermoresponsive shape change (70). Conversely, magnetic microparticle (NdFeB) doped LCEs demonstrated smaller actuation strains than the undoped LCE, though the elastic modulus was enhanced tenfold (13). Multi- and Single-Wall Carbon Nanotube (MWCNT and SWCNT, respectively) incorporation has also been observed to improve thermoresponsive actuation at low loadings and stiffen the host LCE (71, 72). Other carbon derivatives such as graphene have been used for their incredible mechanical strength to impart large actuation stresses in LCE composites (73).

Organic nanoparticles (e.g., polydopamine) have also been harnessed to increase LCE failure strain 14-fold with low loading (74). Despite all these benefits, solid fillers broadly inhibit mesogen alignment which substantially detracts from their actuation behavior, warranting other approaches for improving the mechanical properties.

2.3.2 Interpenetrating Polymer Networks

Interpenetrating Polymer Networks (IPNs) are comprised of a chemically distinct polymer network that interweaves with the main polymer network and can be used as a strategy to bolster mechanical properties. Strategies for synthesizing LCEs incorporating IPNs, herein labeled IPN-LCEs, consist of one-pot and two-stage methods. A one-pot synthesis, for example, involves concurrent orthogonal polymerizations, while a two-stage method involves first polymerizing the LCE followed by swelling with the IPN's monomer and photopolymerization (15, 75). Mechanical improvements endowed from IPN incorporation are manifold. LCE high-temperature fracture behavior was improved by incorporating a polyurethane IPN—this is because PU's mechanical properties do not diminish as substantially as those belonging to the LCE with increasing temperature (75). Extensibility was another mechanical property that could be enhanced via IPNs; polydimethylsiloxane (PDMS) as an IPN was harnessed to double the failure strain of the LCE (76). The influence of IPN sidechain length on IPN-LCE mechanical properties was studied by Ikeda and colleagues (77). By testing IPN-LCEs where the IPN was poly(methyl methacrylate) (PMMA), poly(butyl methacrylate) (PBMA), or poly(dodecyl methacrylate) (PDDMA), it was found that PMMA—which had the shortest alkyl sidechain—provided superior stiffness and toughness. Analogously, different IPN core chemistries (e.g., rigid polyacrylate and thermoplastic polyurethane) were studied by Terentjev and colleagues to maximize the blocking stress and toughness for a vinyl-siloxane-based LCE (78). Using an IPN composed of LC monomers was studied by Hong Yang's group, wherein the two liquid crystal polymer networks contributed to an elastic modulus and breaking strength in the isotropic phase of 10.4 MPa and 7.9 MPa, respectively (15). At the time of that publication, neither metric had exceeded so much as 1.4 MPa above the clearing point. In the context of actuators, IPNs have been used to augment electroactive device performance through a 31-fold increase in the IPN-LCE actuator's elastic modulus (79).

A prominent deterrent to utilizing the two-stage IPN-LCE preparation method is swelling, which results in unequal dispersion of the IPN monomer in the LCE and the LCE chain anisotropy potentially

being adversely affected (17, 79). Additionally, IPNs inhibit alignment strategies such as mechanical alignment for thiol-acrylate LCEs, reducing LC order and shape change.

2.3.3 Phase Modulation

Increasing the amount of molecular order for improving the bulk mechanical properties has been applied to TALCEs; this strategy works due to the heightened intermolecular interactions (14, 49, 57, 59). Through controlling the length of the thiol spacer, a smectic-C phase was introduced into the nematic LCE, producing an order of magnitude increase in the room-temperature storage modulus (57). In another study, using a lower molecular weight thiol chain extender, or modifying the secondary crosslinking reaction to be a thiol-ene polymerization rather than the conventional acrylate homopolymerization, enhanced the thermal actuation strain (49). Ware and colleagues discovered that letting their LCE remain at room temperature permits chain crystallization (14). Possessing both LC and semicrystalline order, this LCE displayed a 100-fold increase in stiffness and a four-fold increase in toughness. Moreover, the work capacity was 18× larger than the reported muscle contraction in mammalian muscles. As a final modification strategy, Guo and colleagues designed an LCE with SmA and nematic mesophases by incorporating smectic side-chain mesogens and nematic main-chain oligomers onto a siloxane backbone (59). Adding side-chain mesogens introduced a pronounced linear elastic region (LER) to the LCE rather than initially entering the soft-elastic plateau, and resulted in considerably steeper strain hardening. The difference in stress-strain response conferred by the side-chain mesogens is seen in Figure 2-5. They proposed the microstructure consisted of side-chain mesogen-dense regions existing as phase-separated smectic domains within the bulk nematic elastomer. Phase modulation does not inhibit liquid crystalline order as solid fillers or IPNs do, but in extreme scenarios impairs LCE shape change as demonstrated by the pure side-chain smectic LCE in Figure 2-5.

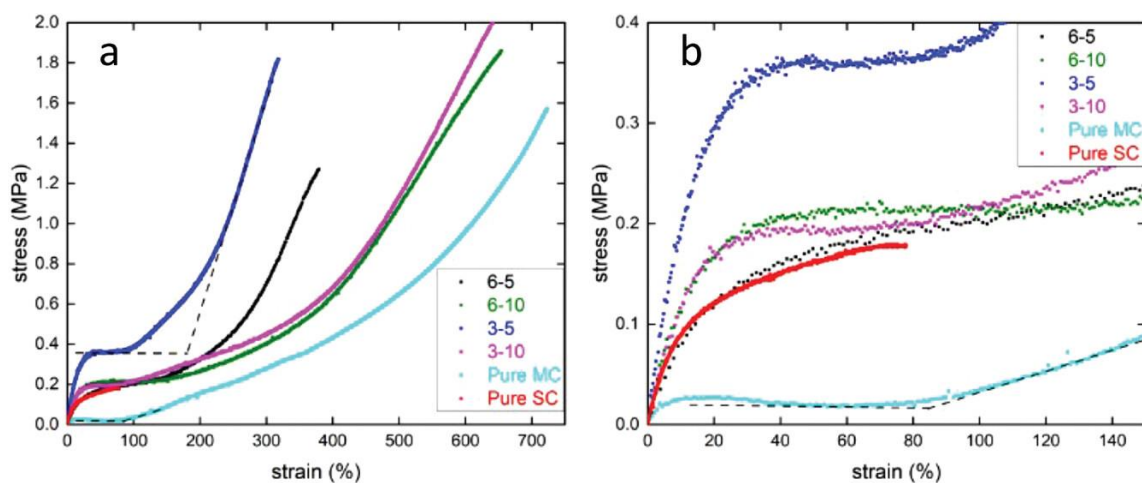


Figure 2-5: Polydomain tensile data for composites comprised of main-chain nematic LCEs and side-chain smectic-LCEs. The stress-strain data for all formulations with side-chain mesogens have a linear elastic region (navy blue, green, purple, black, red). In contrast, the pure main-chain nematic LCE has a yield stress more than 10× smaller. Reproduced with permission (59).

2.3.4 Stiffening with Liquid Inclusions

Recently, Dufresne and colleagues showed that isotropic compliant solids could be stiffened with liquid inclusions (16). This only occurs if an immiscible liquid exists in the solid as droplets smaller than a characteristic length scale. That length scale, the elastocapillary length $L = \frac{\gamma}{E}$, relates the liquid's surface tension to the solid's elastic modulus. Below L , surface energy overpowers strain energy, resulting in significantly smaller droplet deformation, and an enhanced elastic modulus (16). While this was shown with ionic liquids in silicone gel, Dufresne and colleagues developed a theory generalizing their results to gels and elastomers.

Other research groups extended liquid inclusions from isotropic to mechanically anisotropic solids—particularly LCEs. By incorporating Eutectic Indium-Gallium (EGaIn) droplets into an LCE, Carmel Majidi's group reported a sixfold increase in stiffness and a more modest improvement in tensile stress, though droplets were not less than L (80). The stiffening was attributed to physical bonding between thiol groups at the EGaIn droplets. By ensuring the metal droplet sizes were below the elastocapillary length (ca. $3.5\mu\text{m}$), they built on their study by improving the stiffness 22-fold (12, 81). Similarly, Yang et al. decreased droplet sizes even further (ca. $.195\mu\text{m}$) to augment the LCE's elastic modulus 226% and toughness 61-fold (17). Despite these benefits, the metal inclusions impeded

liquid crystal domain formation, as seen through actuation strains for Majidi and Yang's works being only <5% and 55% respectively (12, 17). A thought-provoking question that has not yet been explored to the best of our knowledge is if incorporating anisotropic liquids—such as liquid crystal solvents—into anisotropic solids could also elicit stiffening analogously to liquid inclusions.

2.4 Cyanobiphenyls

Cyanobiphenyls are a family of liquid crystals whose molecular structure is comprised of a rigid head group and a flexible tail group. A cyano group attached to two covalently bound benzene rings constitutes the rod-shaped head group, while the tail is composed of a flexible alkyl chain. The tail's length and component atoms or moieties can be easily modified to adopt different mesophases or tailor the mesophase window. Cyanobiphenyls first gained popularity due to the pentyl homolog 5CB. This is because it was one of the first single-component LCs with a room temperature nematic window (18 or 24-35°C depending on supplier), minimal toxicity, volatility, and cost. Such desirable properties resulted in 5CB becoming ubiquitous in LC studies (82–84). The octyl homolog, 8CB, is also of considerable interest due to its low temperature smectic (21.1-33°C) and nematic windows (33.5-40.5°C) (85). Both 5CB and 8CB are shown in Figure 2-2 of section 2.1.1.

Within LCE research, nonreactive cyanobiphenyls have been used as plasticizers, swelling agents, solvents for promoting alignment, and electrical modulation of polymerization conditions (19, 83, 86). Monofunctional cyanobiphenyl monomers have been used for creating auxetic LCEs—elastomers that expand instead of contracting orthogonally to the stressing direction (87). A unique phenomenon of unreactive low molecular weight (MW) cyanobiphenyls is they partially phase separate from a polymerizing network—whether liquid crystalline or non-LC polymers (88, 89). This separation results in a population of cyanobiphenyl molecules bound to the network, and another segment that is separated from the network which behaves like the bulk solvent (18). While such a phenomenon is prominently documented with 5CB, it is also documented with 8CB. Moreover, 8CB's phase separation from the network is larger due to its higher entropy of mixing (89).

Chapter 3

Materials and Methods

3.1 Materials

1,4-Bis[4-(3-acryloyloxypropyloxy) benzoyloxy]-2-methylbenzene (RM257), 4-Cyano-4'-pentylbiphenyl (5CB), and 4-Cyano-4'-octylbiphenyl (8CB) were purchased from Synthron Chemicals. Additionally, 4-Cyano-4'-pentylbiphenyl (5CB), 4-Cyano-4'-octylbiphenyl (8CB), 2,2-Dimethoxy-2-phenylacetophenone (IG 651), and formamide were purchased from TCI Chemicals. Trichloro(1H,1H,2H,2H-perfluorooctyl)silane, 2,2-(ethylenedioxy)diethanethiol (EDDET), ethylene glycol (EG), pentaerythritol tetrakis(3-mercaptopropionate) (PETMP), 4-methoxyphenol (MEHQ), dipropylamine (DPA), chloroform, dimethyl sulfoxide (DMSO), and hexane were purchased from Sigma-Aldrich. All chemicals were used as received. Silicone oil was purchased from Thermo Fisher Scientific.

3.2 Methods

3.2.1 LCE Synthesis

3.2.1.1 LCE Cell Preparation

Cells in which the LCE mixture was poured during synthesis were comprised of two hydrophobic glass slides (Globe Scientific) sandwiching spacers of 0.5mm thick Shim Stock (McMaster Carr). Glass slides were cut into pairs of one 35×25mm and one 30×25mm slide. They were cleaned with acetone, isopropanol, and deionized water followed by 15 minutes of UV ozone cleaning (Ossila). Hydrophobic glass slides were produced from silanization using the silane listed in section 3.1 under vacuum for 45 minutes. Unless specified otherwise, 0.5mm thicknesses were always used for polydomain LCEs.

3.2.1.2 LCE Synthesis

The polydomain base formulation was prepared as follows by modifying a previously published method (56). A precursor solution was prepared of PETMP (28.3mg), EDDET (63.3mg), RM257 (300mg), MEHQ (.8mg), and chloroform (120mg). MEHQ acts as an inhibitor to prevent premature polymerization of RM257 molecules prior to UV curing. This mixture was heated above RM257's T_{NI} using a heat gun (Tacklife HGP73AC) until all components were dissolved, and then the photoinitiator

IG 651 (1.5mg) was added. To initiate the base-catalyzed reaction, a 2wt% catalyst solution of DPA in chloroform (19 μ L total) was added to the precursor mixture. This was followed by immediate vortexing and placement under a vacuum for bubble removal. The mixture was promptly filled into 0.5mm thick cells on a hot plate at 64°C via capillary filling. Once filled, the cell was immediately removed from the hot plate and the reaction proceeded for three days at room temperature (23°C). Finally, the top glass slide was cleaved with a razor and the sample was placed under vacuum (25inHg) for 12 hours to remove chloroform and quench the reaction. Herein, the LCE's age is measured from when the sample was removed from the vacuum for quenching the reaction.

Polydomain LCEs doped with 5CB or 8CB followed the same protocol with two changes. Firstly, 5CB or 8CB was added to the precursor mixture before dissolving, and secondly, 30 μ L of catalyst solution was used—this was necessary for the reaction to complete within three days. The LC solvents were loaded in weight percentages based on the total mass of the utilized chemical excluding the solvent and catalyst solution. The criterion used for completion of the thiol-Michael addition was when the LCE attained sufficient mechanical properties for a facile, clean detachment of the glass cell from the specimen prior to vacuuming. Monodomain LCEs were made through uniaxially straining polydomain samples in a tensile machine (Cellscale Univert) to the desired length, and then photopolymerizing with one 365nm UV light on either side at a distance of 6cm (Spectroline E-Series). Figure 3-1 schematically shows the incorporated monomers and mesogens in part (a), a molecular schematic of the polydomain LCE in part (b), and the monodomain LCE in part (c). The unreacted excess acrylate groups are represented by beige parallel lines on the RM257 molecules, and the 5CB/8CB as droplets within the matrix. It is important to clarify that only 5CB or 8CB were individually added to a precursor mixture.

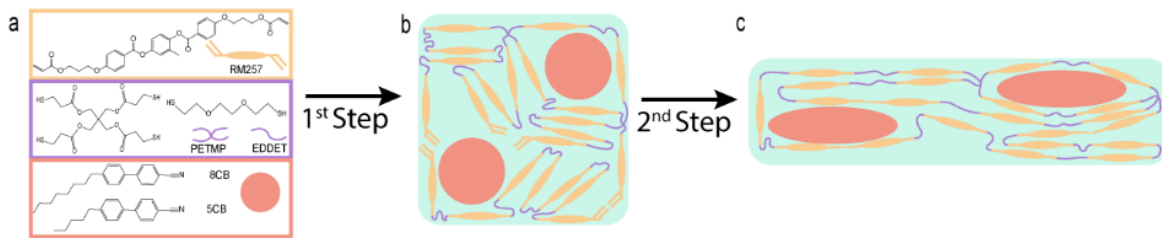


Figure 3-1: LCE Synthesis Schematic. A) Monomers and LC solvent structures, B) Polydomain LCE Chain Conformation, C) Monodomain (Aligned) LCE.

Below in Table 3-1 we delineate the naming convention used in this thesis for the 5CB and 8CB loaded formulations based on the weight percentage of dopant loaded. “M” as the prefix indicates that the formulation has been programmed with a monodomain state via the 2nd stage polymerization, and “P” indicates only the 1st stage thiol-Michael addition has occurred. The control formulation without any dopant is the same for both the 5CB and 8CB chapters and is labeled p0 if polydomain or m0 if monodomain.

Table 3-1: Naming convention of all synthesized formulations based on their alignment, dopant, and dopant concentration

	Dopant	5CB		8CB	
Loading (wt%)	Alignment	Poly	Mono	Poly	Mono
0		p0	m0	p0	m0
10		p5CB10	m5CB10	p8CB10	m8CB10
30		p5CB30	m5CB30	p8CB30	m8CB30
50		p5CB50	m5CB50	p8CB50	m8CB50
70		p5CB70	m5CB70	p8CB70	m8CB70

3.2.2 Miscibility

3.2.2.1 Swelling

A 2×2mm specimen of the monodomain control formulation was cut using a hammer and razor. A microscopy setup was designed with the following elements from bottom to top, and is shown below in Figure 3-2:

1. USB-powered light board
2. linearly polarizing film (on top of the light board)
3. purpose-built microscopy stage made of medium-density fiberboard
4. sheet of graph paper

5. glass microscopy slide
6. Dino-Lite Edge 3.0 USB microscope

Five droplets of 5CB/8CB were deposited on the graph paper using a plastic pipette, and the LCE specimen was placed atop the puddle with forceps. Images taken initially and after 20 hours were analyzed in the microscope's software (Dino-Capture) to determine the change in length and width perpendicular to the specimen's alignment direction and the swelling ratio calculated with:

$$Q = \frac{l_s^{\parallel}}{l_0^{\parallel}} \left(\frac{l_s^{\perp}}{l_0^{\perp}} \right)^2 \quad (3-1)$$

It is assumed that equivalent degrees of swelling take place in both directions perpendicular to \mathbf{n} i.e., the width and the thickness (19).



Figure 3-2: Microscopy Setup for Swelling and Dopant Leakage.

3.2.2.2 Dopant Leakage

A 2×2mm monodomain specimen of the base formulation loaded with 70wt% the total reactant mass of 5CB (i.e., m5CB70) was placed on top of a small pool (~2mL) of silicone oil, and changes in its

length and width were measured in the Dino-Capture software over 33 hours using the microscope setup in Figure 3-2.

3.2.2.3 5CB Contact Angle

A Rame-Hart 190Ca goniometer equipped with a halogen light source, SuperSpeed U4 Series 520 FPS Digital Camera, and a glass syringe with a dispensing micrometer was used for contact angle measurements. (Figure 3-3). One $10\times 10\times 0.5$ mm monodomain specimen of the control formulation was placed atop the goniometer stage, and using a 23Ga needle ten solvent droplets were dispensed on different areas. The left and right droplet contact angles were measured using the instrument's built-in software (DROPimage CA). Droplet measurement involved manually setting one line for the droplet-sample interface, and two more for the droplet's center; the software fits a line to the droplet's surface starting from the solid-liquid-vapor contact point. The contact angle was calculated by averaging the right & left angles for each droplet.

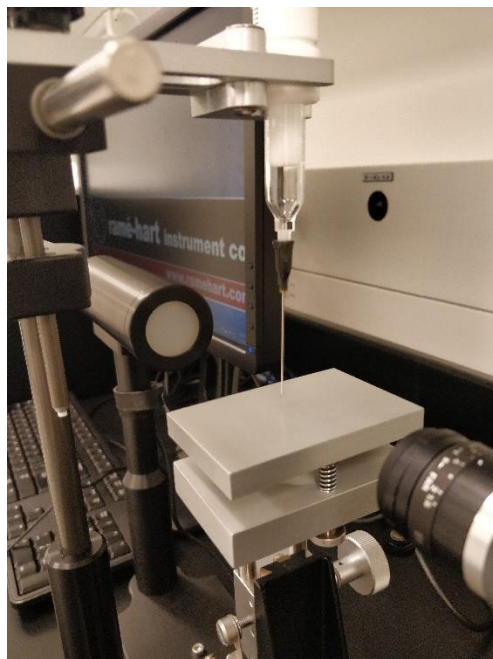


Figure 3-3: Goniometer setup. From left to right: light source, stage, dispensing syringe, camera.

3.2.2.4 LCE Surface Energy

The undoped LCE's surface energy was measured using the Owens-Wendt theory in conjunction with the contact angle of four solvents with known polar and dispersive components of surface energy

(deionized water, EG, DMSO, formamide) (90–92). Using the same contact angle calculation procedure in section 3.2.2.3, a system of four equations—each with the following format—was solved for the unknown dispersive (γ_s^D) and polar (γ_s^P) components of surface energy for the LCE (93, 94). A custom MATLAB code using the fsolve function was developed for this procedure.

$$\gamma_l(1 + \cos\theta) = 2\sqrt{\gamma_s^D\gamma_l^D} + 2\sqrt{\gamma_s^P\gamma_l^P} \quad (3-2)$$

The LCE's surface energies were compared against the same result utilizing the Wu method (95).

3.2.2.5 Group Contribution Theory (GCT)

Solubility parameters δ for each of the LCE monomers and the biphenyl dopants were obtained by summing the molar attraction constants from constituent groups of the overall molecule as reported by Small using the following formula (96). Here, M is the molecular weight, ρ the density, and F is the Molar Attraction Constant.

$$\delta = \frac{M\rho}{F} \quad (3-3)$$

Next, the squared difference was taken between the LCE monomer average, δ_p , and each dopant, δ_s . The differences for both 5CB and 8CB were compared against the LCE's monomer average to determine if they were below the cutoff criterion of $1.2 \text{ cal}\cdot\text{cm}^{-3}$ for the polymer to be soluble in the solvent (96).

3.2.2.6 Cross-Sectional Cryo-Fracture Scanning Electron Microscope (Cryo-SEM)

Cross-sectional cryo-fracture SEM (herein abbreviated Cryo-SEM) was performed to image the cross-sectional area of fractured polydomain LCE specimens. Tested formulations include p0 and moderate (p5CB30 and p8CB30) and high (p5CB70 and p8CB70) loadings of 5CB/8CB. Doped specimens (dimensions $8\times 2\times 0.5\text{mm}$) were either a) submerged in hexane for 24 hours before fracturing, b) submerged in hexane for 24 hours after fracturing, or c) unmodified before fracture. Hexane was used to remove any 5CB/8CB as a measure providing added contrast to the unmodified doped formulations. Samples were cryo-fractured as follows. For each of the following formulations (the control, 30wt%, and 70wt% cyanobiphenyl loading) one specimen was placed in a plastic petri dish and liquid nitrogen was poured over it to submerge the specimen. Once bubbles had stopped coming off the specimen, it was plastically fractured along its width through bending with two forceps.

SEM samples were prepared by taping the specimen with carbon tape to a 90° SEM stub and coating with a gold sputter since the LCE is not a conductive material. Secondary electron imaging was performed on a Hitachi SU5000 Field Emission SEM for 5CB-doped formulations and a Tescan VEGA TS-5130 SEM with a tungsten filament for 8CB-doped LCEs.

3.2.3 Thermal Analysis

3.2.3.1 Differential Scanning Calorimetry (DSC)

DSC (TA Instruments Q2000 with RCS90) measurements were taken on 8.7-9mg polydomain samples using a heating/cooling rate of 5°C/min following a heating (10°C/min) and cooling cycle (5°C/min) to reset the thermal history. A five-minute isothermal step was employed between each temperature ramping step. Hermetically sealed pans were used for all samples.

3.2.3.2 Dynamic Mechanical Analysis (DMA)

DMA (TA Instruments Q800) measurements followed a previously published protocol (54). Briefly, 15×4×0.5mm (length×width×thickness) specimens (n=3) were measured in tensile mode with gauge length 6mm under 0.2% strain and 1Hz with a heating rate of 3°C/min from -50 to 120°C. The force track was set to 125%. Specimens were thermally cycled through their T_{NI} before the temperature sweep to reset any thermal history.

3.2.3.3 Coefficient of Thermal Expansion

Thermal expansion measurements were taken on a custom-made heating stage (Polaviz) with a Dino-Lite Edge 3.0 USB microscope under cross-polarizers (for p0 and all 5CB formulations), or a Euromex iScope Polarized Optical Microscope equipped with a Pixelink PL-D752CU camera and Linkam TMS93 Temperature controller (for the 8CB formulation). 2×2mm monodomain specimens (n=4) for each formulation were heated at 3°C/min from 25°C to 140°C and then cooled down to the starting temperature. Within the heating stages, specimens were placed atop a silicone oil droplet (~1cm diameter) on top of a glass slide to prevent the sample from adhering to the slide. Images were taken every 5°C, and side length changes were measured in Tracker (Physlets.org).

3.2.4 X-Ray Diffraction

3.2.4.1 Wide-Angle X-ray Scattering (WAXS)

WAXS was performed on a Xenocs Xeuss 3.0 system with an Eiger2 R 1M detector. Operational parameters include acquisition time—30 mins, wavelength—1.54Å, temperature—25°C, sample-detector distance—.042501m, incident angle—.099975°, and q-space range—.003-3.89Å⁻¹. 1D peaks were extracted from the images using Datasqueeze and analyzed in OriginPro to obtain the d-spacings and correlation lengths. Polydomain specimens had initial dimensions of 10×10×0.5mm, and the first test involved testing these specimens without modification. The second test involves stretching each to 50% engineering strain. The third test examined formulations stretched to the following strains for inciting monodomain alignment: p0: 60%, p5CB10: 115%, p5CB30: 235%, p5CB50: 95%, p5CB70:40%, and p8CB30: 185%.

3.2.4.2 Fourier-Transfer Infrared Spectroscopy with Attenuated Total Reflection

FTIR-ATR was performed using a Thermo Nexus 670 spectrometer. Liquid nitrogen was added to the machine prior to parameter setup on the software (Omnic 8). Using a scanning range of 4000-720 cm⁻¹ and a maximum signal set between 2.5-5, the background spectra were collected. Next, polydomain samples (12×10×0.5mm) were stretched lengthwise to the strain required for monodomain alignment and fastened with masking tape over the Zinc Selenide (ZnSe) crystal. Then the spectra were measured with an average of 32 scans being reported.

3.2.4.3 D-Spacings and Correlation Lengths

D-spacings were calculated for each peak from the following equation, where q is the reciprocal-space value of the peak center (97):

$$d = \frac{2\pi}{q} \quad (3-4)$$

Correlation lengths were calculated using the following equation, where the denominator is the full-width half maximum (FWHM) (98). The FWHM was calculated using a Gauss function fit to the peaks in OriginPro with a user-defined baseline for defining the start and end instances of each peak. The Gauss fit function was chosen over Gaussian and Lorentzian functions since it had lower R² values on average than the other two functions.

$$\xi = \frac{2\pi}{FWHM} \quad (3-5)$$

3.2.4.4 Order Parameter Calculations

S, the orientational order parameter, was calculated from azimuthally integrated 1-dimensional (1D) curves of the 2D WAXS patterns using Herman's orientation function (99):

$$S = \frac{3\langle \cos^2 \theta \rangle - 1}{2} \quad (3-6)$$

Where θ is the azimuthal angle. The expectation value in the above equation is calculated from the azimuthal angle and corresponding intensities $I(\phi)$:

$$\langle \cos^2 \theta \rangle = \frac{\int_0^{\pi} I(\phi) \sin \phi \cos^2 \phi d\phi}{\int_0^{\pi} I(\phi) \sin \phi d\phi} \quad (3-7)$$

3.2.4.5 Size of Dopant Phase Separated Region

Taking the longitudinal correlation length $\xi_{1,x}$ as the ellipsoidal region's long axis, the radius of the phase-separated domain's spherical conformation in the initial polydomain state is:

$$\frac{\xi_{1,x}}{2 \times (1 + \epsilon)} \quad (3-8)$$

Here, ϵ is the engineering strain to which the LCE is stretched.

3.2.5 Mechanical Tests

3.2.5.1 Polydomain and Monodomain Tensile Tests

For polydomain samples, 12×4×0.5mm (length×width×thickness) samples with gauge length 6mm were strained in a CellScale Univert equipped with 10N load cell at 0.1mm/s until failure with 0.1N preload. A five-day study of the polydomain formulations' stress-strain curve evolution was also conducted with the same protocol. Before all tensile tests, specimens were thermally cycled above their clearing point to reset the thermal history. All formulations were subject to polydomain tensile tests in duplicate.

Monodomain tensile tests ($n=3$) in the direction parallel to alignment were performed with the same strain rate but a different length/width ratio ($16\times 4\text{mm}$), gauge length (5mm), and load cell (50N). Only m0, m5CB30, and m8CB30 were the tested formulations. Thicknesses for formulations depended on the strain at which they were photopolymerized; these were measured prior to tensile testing with a caliper. Monodomain tensile test protocol in the direction perpendicular to alignment was performed with the same strain rate and length/width ratio, but different gauge length (5.4mm) and load cell (10N). Thicknesses were measured for each formulation prior. To prevent slippage in the monodomain samples, 60-grit sandpaper was fastened to the flat of tensile clamp jaws with double-sided Gorilla tape.

3.2.5.2 Strain Induced Alignment

Measuring the strain at which LCE formulations transitioned from polydomain to monodomain was accomplished by measuring how linearly polarized light transmission changed with strain. The importance of measuring this strain value is discussed in 4.2.5.3. This experiment followed a previously reported protocol with the following modifications (100).

A custom setup was assembled for this study and its layout is shown in Figure 3-4. Briefly, linearly polarized light originates from the continuous-wave laser source (Obis LX 637nm) and passes through the following order of components (all from Thorlabs) before reaching the LCE specimen and finally the light detector (Thorlabs S120C).

1. 2×1 " diameter Differential Adjuster mounted mirrors
2. Achromatic Half-Wave plate
3. $0.5\times$ Magnification Galilean telescope

Differential adjusters were used to adjust the mirror pitch and yaw to ensure the beam height was constant and had minimal divergence (i.e., a spot size that does not increase by more than 1mm before arriving at the detector). The first criterion was measured using two pinholes $\sim 5\text{cm}$ apart, and the second criterion using a laser viewing card. The half-wave plate functions as a polarization rotator to create an incident beam that is linearly polarized with the LCE's stretching direction, or perpendicular to this direction—that is, within the plane of the table. The Galilean telescope, created with a convex lens followed by a concave lens, was used to reduce the beam size from 3mm to 1.5mm to avoid the spot size being larger than the sample width at high strains. The sample-to-detector distance is 20.50cm and the laser-to-sample distance is 27.5cm .

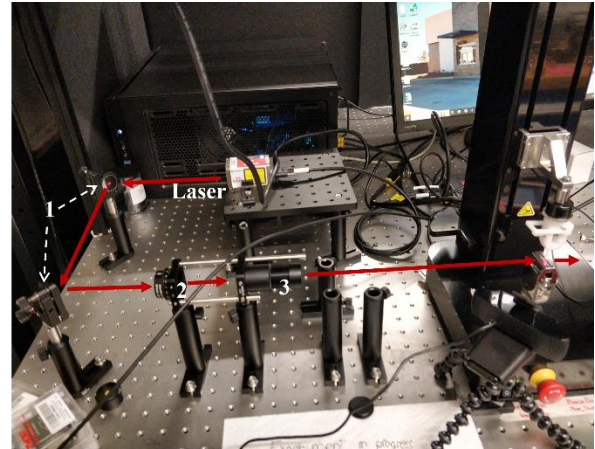
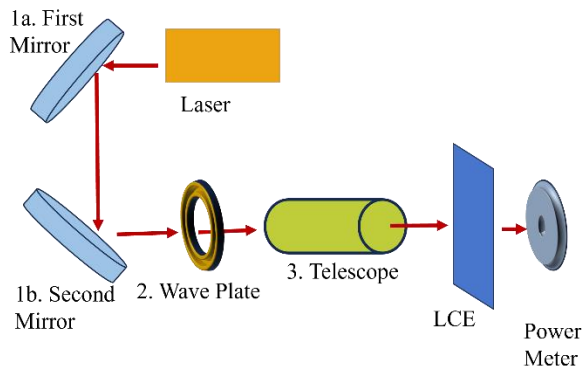


Figure 3-4 Diagram (left) and Picture (right) of Transmission Measurement Setup. The power meter is to the right of the tensile apparatus (not pictured).

First, the laser's operating power was set to 1mW and the unobstructed beam's power was recorded from the power meter for 1 minute and recorded as T_{max} for the whole study. 12×10×0.5mm polydomain specimens (three per formulation) had their thickness recorded and were thermally cycled through their T_{NI} . One specimen was then loaded into the tensile machine (gauge length 6mm) such that the beam was centered on the LCE to block the light's path to the detector. The tensile machine's parameters for the test were the same as for the polydomain tensile protocol as in 3.2.5.1. For measuring light transmission, the Thorlabs Optical Power Monitor software had a sampling interval of 0.5 seconds. To commence the test, power measurements were logged for 10 seconds before starting the tensile program. Power readings were recorded until the specimen failed. Cross-referencing the power readings' time stamps with those from the tensile program, transmission coefficients were calculated as reported previously (100).

Chapter 4

Nematogen Loaded Liquid Crystal Elastomers

4.1 Design Considerations

4.1.1 LCE Selection

To determine if an LCE can be developed that is stiffened via liquid crystal inclusions without substantially compromised extensibility, judicious selection of an LCE matrix and anisotropic liquid dopant was required. The thiol-acrylate LCE chemistry was chosen for its ease of synthesis; specifically, a recipe developed by Barnes et al. was decided upon as its reactant ratios have been optimized for fidelity and shape-programmability (56). They optimized the reactant mole percentages (mol%) for an LCE to retain its programmed conformation and adopt its original shape. These values were a 75/25 mol% ratio of $-SH$ groups being contributed by EDDET/PETMP, and 10mol% more acrylate vinyl groups than required to completely react with the thiol groups (56).

4.1.2 Dopant Selection

Concerning the choice of anisotropic liquid dopant, the candidates were narrowed down to unreactive low-molecular weight liquid crystal solvents due to their ability to partially phase separate from the network during polymerization. Specifically, 5CB was chosen for its low cost, and stable nematic phase at room temperature (22-35°C) (101).

4.2 Results and Discussion

4.2.1 Polymerization with 5CB

First, it is important to examine how the LC dopant, 5CB, mixed with the LCE when included in the polymerization process to see if the thiol-Michael reaction is adversely impacted and how the doped LCE differed from the neat formulation p0.

Observing the neat LCE's 1st stage polymerization, the viscosity substantially increases in the time after injecting the catalyst solution, vortexing, and vacuuming to remove any bubbles (total 20 seconds). When infiltrating the precursor solution to the glass cell it now resembles syrup in viscosity rather than exemplar oils as before. The LCE also develops sufficient mechanical properties within six hours—this was determined by palpating residues outside the sandwiched glass slides, which transition from a

viscid, incompletely polymerized gel, to solid and marginally sticky over six hours. In contrast, the precursor solution loaded with 5CB did not qualitatively change viscosity from catalyst solution injection to cell infiltration, and residues outside the cell remained viscid for 2-3 days post-injection. Though both had different polymerization timescales, they were left to react for 48 hours before vacuuming to remove the chloroform and quench the reaction. The tested doping percentages were 10, 30, 50, and 70wt%.

Post-vacuuming, p0 was opaque and white, which is due to the characteristic scattering of its polydomain nature. The sample was smooth when moving metal forceps across the surface, but when pressing into the sample the forceps adhered. Meanwhile, the doped LCEs were a cloudier and milkier white, which is the room-temperature appearance of 5CB. Such visible characteristics were increasingly prominent in higher weight percentage formulations. Forceps also adhere to the dopant-loaded formulations, though the samples felt slippery in contrast to p0's distinct smoothness. All doped formulations except the p5CB70 were visibly macroscopically homogenous and did not contain regions differing in appearance from the opaque cloudy white. P5CB70 had separate, more translucent regions from the white portions, suggesting that regions with more 5CB than LCE existed. Nevertheless, it was imperative to study the miscibility of 5CB and the LCE to garner a more complete understanding of their interaction. This is examined in the next section.

Qualitative differences in mechanical properties were also examined. P0 also has qualitatively higher notch toughness than any 5CB-doped formulation, an attribute discerned from cutting specimens with a razor. Qualitative extensibility tests through stretching specimens with forceps were conducted to ensure sufficient chain length was developed for undergoing the polydomain-monodomain transition (PMT). All 5CB-doped formulations contain sufficient chain length for exhibiting the PMT. When stretched with forceps all formulations underwent this transition, with p5CB30, p5CB50, and p5CB70 initially resisting the stress but then stretching and retaining their final length for small strains. Meanwhile, p5CB10 did not maintain the extended length and decreased slightly, which is similar behavior to p0.

4.2.2 Miscibility

A liquid inclusion is a liquid that is immiscible with its host matrix, and is a key feature of the soft materials stiffening detailed by Eric Dufresne (16). To examine 5CB's miscibility with the LCE, it can be experimentally understood to varying degrees. Swelling behavior and dopant leakage, contact angle

measurements, and cross-sectional cryo-fracture SEM serve as qualitative measurements of miscibility, while group contribution theory (GCT) is a quantitative metric of solvent-polymer interactions. Each method is examined in the following subsections.

4.2.2.1 Swelling

The degree to which 5CB can swell the LCE qualitatively describes the dopant miscibility with its host matrix. This is especially important to inform the liquid inclusion stiffening hypothesis because 5CB substantially swells acrylate-based LCEs as evidenced by swelling ratios of 110-246% (19, 102, 103). Swelling was tested on monodomain specimens of the control formulation (m0) since polydomain LCEs swell isotropically, rendering shape change not as visible (104). Figure 4-1 shows the LCE initially placed in the 5CB pool on the left, and the swollen state after 20 hours on the right. Positive (16%) and negative (17%) length changes were measured in the direction perpendicular and parallel to the director \mathbf{n} , respectively. Assuming the same length change in the direction perpendicular to alignment occurs along the sample thickness, the calculated swelling degree is 135%, which is in the lower half of 5CB's swelling range of acrylate chemistry-based LCEs. Of noteworthy importance is that the specimen does observe conservation of volume, and minor discrepancies between this phenomenon and the measured percentages are attributed to the LCE edges not being exactly normal to the microscope. The ambient temperature during this study was 23°C at which 5CB is in its nematic phase. This temperature corroborates why the graph paper was visible through the 5CB liquid.

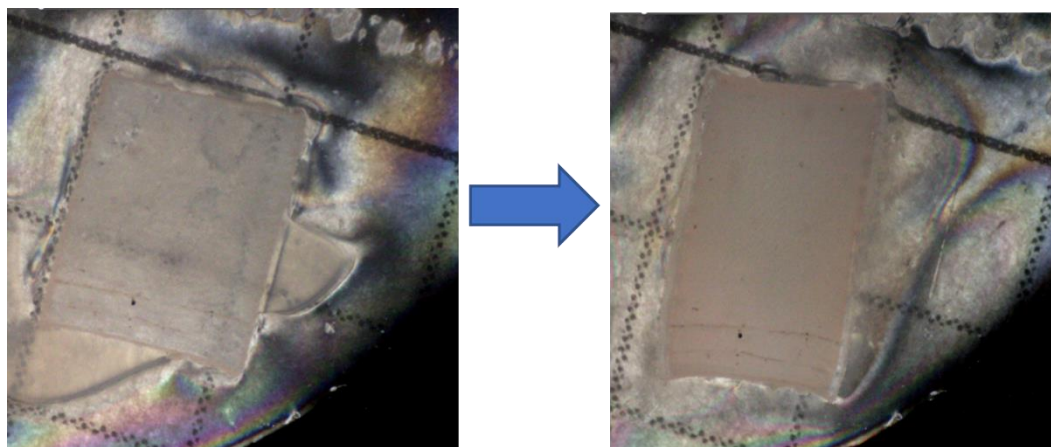


Figure 4-1: Initial and Swollen m0 in 5CB. (Graph paper square edges are 3mm).

4.2.2.2 Dopant Leakage

In a similar vein to solvent swelling, the extent to which 5CB leaks out of an LCE with high cyanobiphenyl loading qualitatively informs the strength of interactions between the two. Only the highest loaded formulation was tested since if this formulation did not have any leakage, it can be assumed that the formulations with less loading do not leak 5CB. Only m5CB70 was tested, and its initial state and final state after 33 hours are shown on the left and right of Figure 4-2. Minor positive (2%) and negative (2%) length changes are observed parallelly and perpendicularly confirming that minimal 5CB leakage occurs.

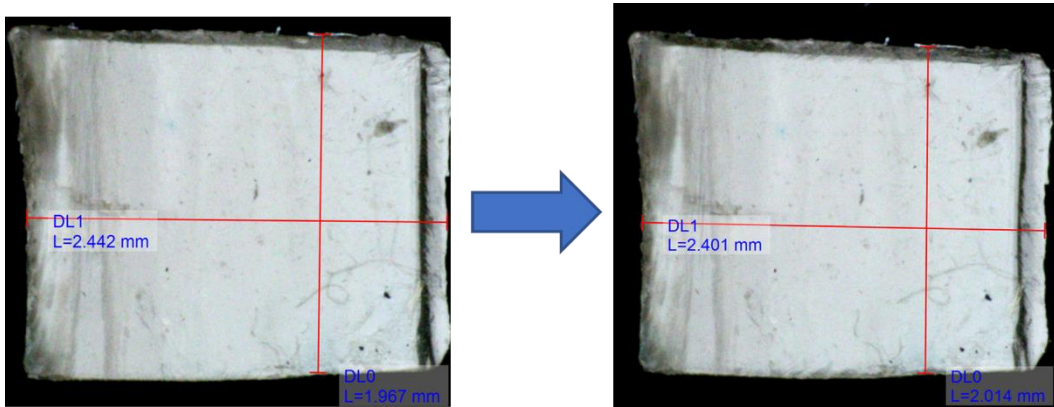


Figure 4-2: Initial and Final Dimensions of M5CB70 after 33 hours.

4.2.2.3 Contact Angle and LCE Surface Energy

Thus far 5CB's interaction with the LCE has been qualitatively studied. From a quantitative vantage, contact angle measurements provide an indication of miscibility, where the solvent wetting the neat LCE confirms thermodynamically favorable interactions. Averaging across the left and right contact angles of ten droplets, 5CB's contact angle was measured to be $35.5^\circ \pm 2.9^\circ$, corroborating the previous two experiments by wetting p0. Figure 4-3 shows a 5CB droplet wetting the LCE surface, with line segments for the curve fitting.

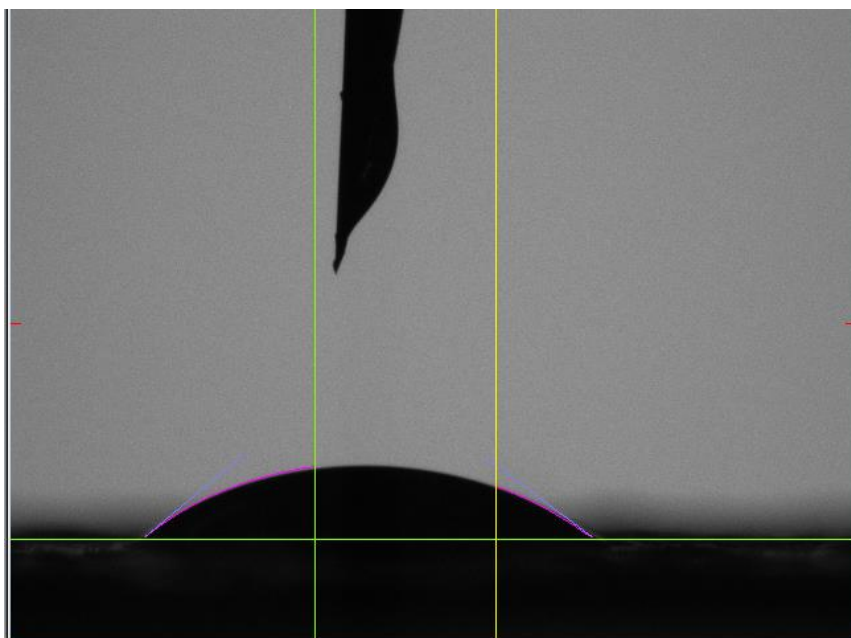


Figure 4-3: 5CB Contact Angle Measurement.

A more quantitative description of this wettability was obtained from the LCE surface energy calculation, where the measured contact angles are tabulated below:

Table 4-1: Solvent Contact Angles with LCE

Solvent	Deionized water	Ethylene glycol	DMSO	Formamide
$\theta(^{\circ})$	72.1	61.2	41.0	68.9

The calculated LCE surface energies from the Owens-Wendt and Wu theories were 30.7 and 34.5 mN/m, respectively. Considering 5CB's surface tension is 35.1 mN/m at 25°C, the LCE and dopant indeed have favorable interactions (105). However, a more quantitative study is necessary to comprehensively describe 5CB's miscibility with the matrix.

4.2.2.4 Group Contribution Theory

It was endeavored to quantify the interactions between the LCE and 5CB beyond a qualitative label of wetting or swelling, and definitively quantify the dopant's miscibility with the LCE. A Group Contribution Theory (GCT) developed by Small provides a means to additively determine solvent miscibility with a polymer using Molar Attraction Constants (96). As seen in Table 4-2, the difference

between 5CB and the LCE solubility parameters is markedly less than the cutoff criterion of $1.2 \text{ cal} \cdot \text{cm}^3$ for the LCE to be soluble in the solvent. This reinforces the miscibility between the dopant and the matrix determined in previous sections. As a counterexample, a solvent such as glycerol is expected to be immiscible since its $\delta_s = 16.5 \text{ (cal} \cdot \text{cm}^{-3})^{.5}$, substantially differing from that of the neat LCE and exceeding the solubility criterion.

It is important to note that no Molar Attraction Constants were found for a trisubstituted phenyl, as is the case with the central benzene in RM257. Consequently, the Molar Attraction Constant for phenylene was used in this instance with the methyl group also added. Considering the Molar Attraction Constants tabulated in Small's work, a trisubstituted phenyl ring would not result in failing the cutoff criterion.

Table 4-2: Solubility Parameters and Differences for 5CB and the LCE

Component	$\delta_p \text{ (cal} \cdot \text{cm}^{-3})^{.5}$	$\delta_s \text{ (cal} \cdot \text{cm}^{-3})^{.5}$	$(\delta_s - \delta_p)^2$
LCE	9.52	-	-
5CB	-	10.01	.24
Glycerol	-	16.5	48.72

4.2.2.5 Cryo-Fractured Cross-Sectional Scanning Electron Microscopy (Cryo-Fracture SEM)

All miscibility sections thus far have established 5CB as being miscible with the LCE through qualitative and quantitative examination. Recalling the theory of liquid inclusion stiffening, is this not adverse, since the liquid must be immiscible? Firstly, 5CB's swelling of this LCE chemistry is considerably less than with other chemistries. Secondly, the GCT criterion does not indicate how well the solvent solubilizes the LCE. While macroscopic phase separation is not noticeable save for in p5CB70, there are instances of LCEs having nanoscale phase separation due to differences in molecular ordering, suggesting that it is still possible to have phase separation and some degree of immiscibility (57, 59).

Currently, it is not known if the LC solvent is fully trapped within the network or if it exists in a phase-separated manner within the LCE; it was only known that 5CB partially swells the LCE, and that the LCE is soluble in the LC solvent from a GCT standpoint. Observing no evident macroscopic phase

separation under digital microscopy, the next level of abstraction for determining visual phase separation was imaging the microstructure. Consider the scenario of 5CB existing within the network in a phase-separated manner. If the LCE was left immersed in a solvent that dissolves, the dopant could be extracted and the remaining voids contained in the matrix could be imaged using Scanning Electron Microscopy (SEM). As such, SEM of the cross-section of cryogenically fractured samples was conducted to determine if these voids existed.

The chosen formulations for imaging were undoped (the control, or p0), moderate doping (p5CB30), and the highest loading levels (p5CB70). Hexane was the solvent of choice for dissolving and removing the 5CB due to the similar structure and its volatility. 8×2×0.5mm specimens of the p5CB30 and p5CB70 were weighed and then submerged in hexane in closed 5mL vials for 24 hours before being left to dry on lab wipes for 30 minutes before weighing. P5CB70 decreased in mass by 9%, indicating the removal of some unreacted molecules. Of the chemicals that could be removed, RM257 and 5CB comprise the resounding majority. Since the thiol-Michael addition achieves high conversion and hexane is known not to swell polymerized RM257, most of this extracted mass is inferred to be 5CB (54, 106). Comparatively, the p5CB30 sample mass changed less than 2% after extraction (~0.2mg), conveying that substantially less 5CB was removed.

Concerning the cryo-fracturing process, p0 and p5CB30 specimens were noticeably more difficult to fracture than p5CB70 on account of their lower LC solvent fractions. Secondary electron imaging was performed on the following seven samples:

1. p0 without extraction
2. p5CB30 without extraction
3. p5CB70 without extraction
4. p5CB30 fractured before extraction
5. p5CB30 fractured after extraction
6. p5CB70 fractured before extraction
7. p5CB70 fractured after extraction

Images of the first three samples taken with 300-500× magnification are seen in Figure 4-4. All formulations show cracks generated from the fracturing process comprising the surface topography and

no phase separation is seen. SEM images for formulations drowned in hexane (p5CB70 at 500× magnification and p5CB30 at ~1000×) are shown in Table 4-3, and also display the surface roughness from cracks. However, of greater importance are the darker regions observed in the p5CB70 sample cryo-fractured after extraction since these are not displayed in other formulations that underwent extraction with hexane. These darker regions could be evidence of the postulated voids created from phase-separated 5CB removal via hexane. At 70wt% loading, there may be sufficient 5CB for the formation of micron-sized domains that phase-separate from the LCE. A rationale for why voids are not visible in the p5CB30 is such phase-separated domains are too small for detection at this resolution. Attempts to image 1µm resolution or less degraded the specimens within seconds and it was not possible to obtain images. Verifying that smaller phase-separated domains exist is examined in the x-ray scattering section. This pattern of light and dark regions does not resoundingly confirm phase separation, however, since the pattern is notably not visible throughout the whole sample. Soaking the samples before cryo-fracture is seemingly the best method for imaging phase separation. This is because cryo-fracturing preserves the created voids from soaking in hexane, whereas any voids generated during hexane extraction—but after the cryo-fracturing process—are prone to collapsing due to capillary forces when the hexane is dried or evaporates away. Of noteworthy importance is confocal microscopy was also attempted for visualizing phase-separation with a rhodamine-based dye polymerized to the LCE and pyrene dissolved in 5CB before the first-stage polymerization. Imaging of monodomain LCE specimens with each dye's respective excitation wavelength did not conclusively show phase separation.

In summary, the miscibility section developed 5CB's adequate miscibility with the LCE, and possible phase-separated regions of 5CB were observed in p5CB70. Though these studies show that 5CB does not meet the immiscibility criterion for liquid inclusion stiffening, it is still possible to have phase separation that has not been detected—for example nanoscale phase separation.

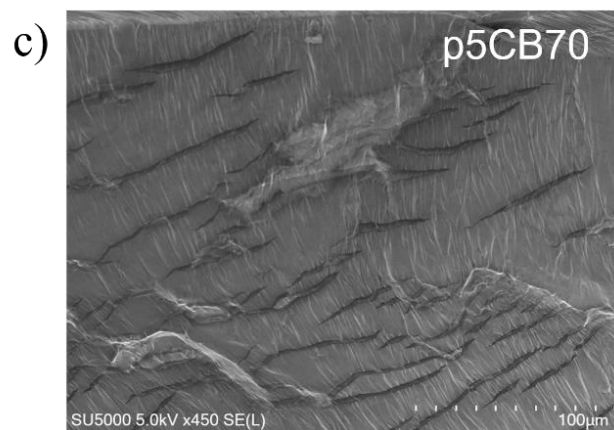
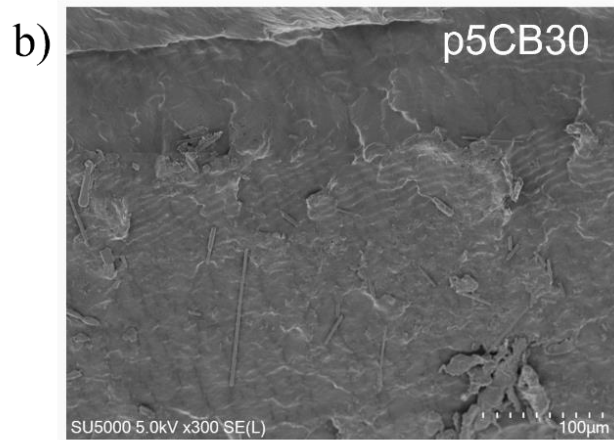
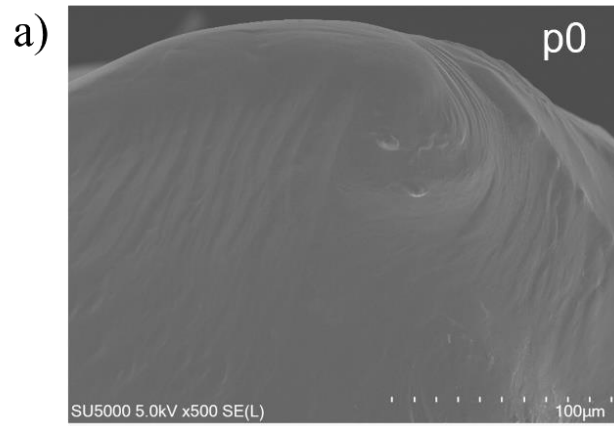
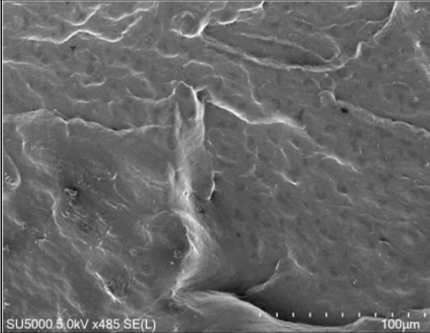
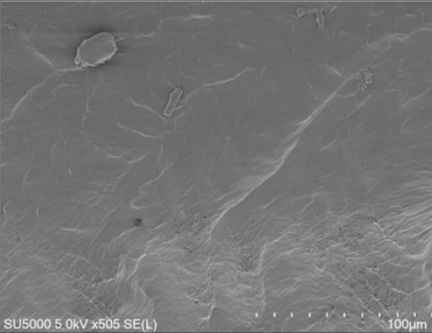
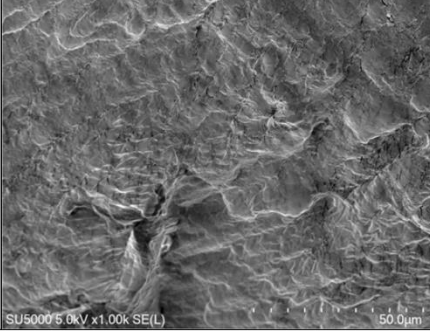
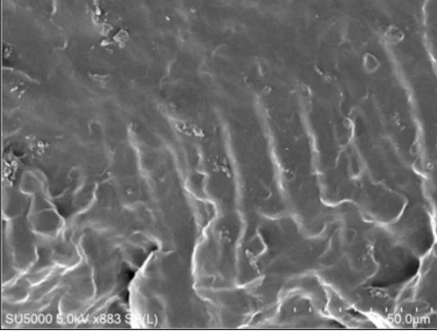


Figure 4-4: SEM of Samples without any extraction performed.

Table 4-3: SEM of Samples that underwent extraction

Formulation/ Magnification		Extraction Before Cryo-Fracture	Extraction After Cryo-Fracture
p5CB70	500		
p5CB30	~1000		

4.2.3 Thermal Analysis

4.2.3.1 Differential Scanning Calorimetry (DSC)

In a thermotropic LCE, shape programmability and molecular ordering—which engenders the mechanical properties—stem from temperature-dependent LC phases. This fact underscores the importance of probing 5CB’s impact on the LCE mesophases. Figure 4-5 and Figure 4-6 show Differential Scanning Calorimetry (DSC) heating and cooling cycles for the polydomain formulations. 5CB’s melting and clearing points are denoted with black dashed lines in Figure 4-5. All formulations exhibit a cold crystallization peak, T_{cc} , at 34°C/30°C in the heating/cooling cycles. This phenomenon is previously observed in thiol-acrylate LCE chemistries (107, 108). Cold crystallization has been shown to appear only in the heating cycle and not the cooling cycle in some chemistries, which potentially explains p5CB30 having no T_{cc} in its cooling cycle (14). The cold crystallization peak is labeled with a dashed line in Figure 4-5. Noting that the T_{NI} for 5CB is 35°C, if 5CB’s nematic-isotropic

transition were being observed, this would manifest as an endothermic peak in the heating cycle, which is not the case. A step representing the glass transition (T_g) is also observed and changes with 5CB loading. Of more interest was the transition in p5CB30, p5CB50, and p5CB70 just below p0's Nematic-Isotropic temperature (T_{NI}). The clearing point was confirmed by an observed opaque-transparent shift indicative of the polydomain nematic-isotropic transition (10, 54). These three formulations possess transitions with two local extrema above the T_{NI} of 5CB in both the heating and cooling cycles, indicating the presence of two mesophases below the matrix's clearing point (57). The values of these transitions are reported in Table 4-4 alongside the transitions from other formulations. The transition temperatures were taken from the heating cycle as the transitions are more distinct than in the cooling cycle. Since the lower transition temperature's phase is unknown, we denote it as T^* . Slight differences in recorded temperatures for these transitions exist since they are kinetically governed events. At slower ($2^\circ\text{C}/\text{min}$) or faster ($10^\circ\text{C}/\text{min}$) ramp rates, the T^* transitions were not discernible. All transitions being above 5CB's T_{NI} can be explained by most LC solvent molecules being strongly complexed to the network, such that no detectable population of free dopant molecules exists, which is reinforced by the absence of a transition at the dopant's T_{NI} (18, 57). 5CB's molecular ordering will be examined in more detail as we strive to determine the lower mesophase's nature, which will warrant x-ray scattering and correlation length measurement.

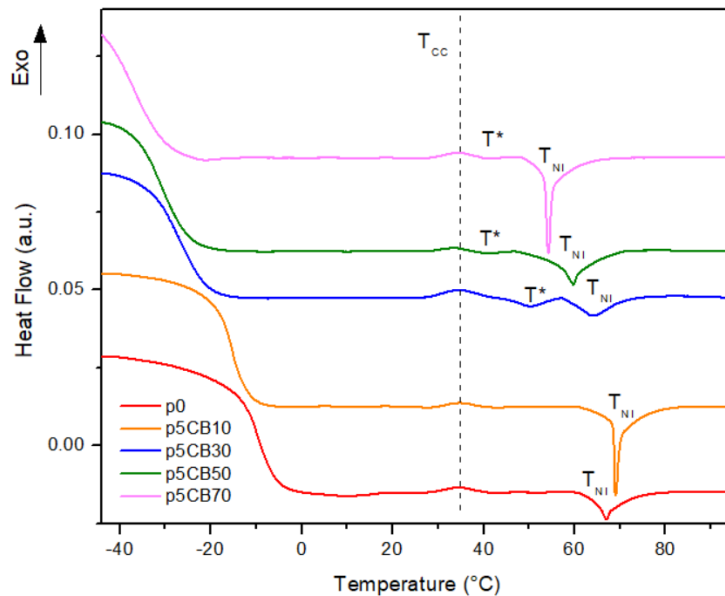


Figure 4-5: DSC Heating Cycle for 5CB Formulations. Endothermic transitions are labeled above their peaks. Cold crystallization is denoted with a dashed line.

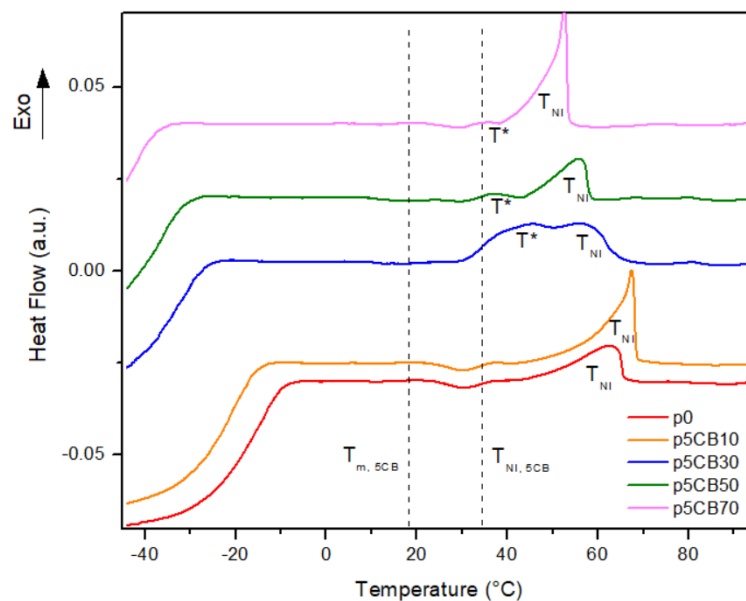


Figure 4-6: DSC Cooling Cycles for 5CB Formulations. Endothermic transitions are labeled below their peaks. 5CB's transitions are denoted with dashed lines.

Table 4-4: Transition Temperatures from DSC Heating and Cooling Cycles

	Heating			Cooling		
	T_{CC} (°C)	T^* (°C)	T_{NI} (°C)	T_{CC} (°C)	T^* (°C)	T_{NI} (°C)
p0	34	-	67	30	-	62
p5CB10	34	-	69	30	-	67
p5CB30	34	50	64	30	45	57
p5CB50	33	41	60	30	37	56
p5CB70	34	41	54	30	36	52

Other loading percentages also displayed this lower mesophase to varying degrees. P5CB10 does not showcase a secondary peak but has a sharper and larger T_{NI} peak than p0 in both heating and cooling cycles. P5CB10 has a heightened degree of crystallinity due to the larger enthalpy compared to the

virgin LCE. Expectedly 5CB lowers the T_g since its low molecular weight molecules resist chain movement to a smaller extent than the equivalent fraction of LCE chains that is present in the neat LCE. 5CB at 10wt% loading elevates the T_{NI} , which is thought to be a small enough fraction for packing between chains and sufficiently augmenting π - π stacking and induced dipole interactions. Similar increases in the clearing point due to small loadings of large aspect ratio dopants have been observed in carbon nanotubes (109).

4.2.3.2 Dynamic Mechanical Analysis (DMA)

DMA is used for measuring to what extent a polymer demonstrates viscous and elastic behavior. As DMA has been used extensively for studying LCEs, and considering our system has a large liquid component, it was important to investigate the viscoelastic properties of the 5CB doped LCEs. Crucially, DMA can also be employed to more accurately determine the behavior at the secondary DSC peaks, since comparatively larger changes occur in the mechanical properties than the heat capacity during changes in the crystal structure (110). Using a procedure from literature, the storage modulus and $\tan\delta$ as a function of temperature are graphed in Figure 4-7, Figure 4-8, and Figure 4-9 (54).

Figure 4-7 shows that all formulations exhibit typical viscoelastic behavior of LCEs. Starting with a glassy region at low temperatures, the glass transition region follows suit. The storage modulus continues to drop to a minimum, which is associated with the T_{NI} , and then increases to a plateau in the isotropic state. Uniquely, a rubbery plateau develops in p5CB30, p5CB50, and p5CB70 after the glass transition, which denotes higher degrees of crystallinity (111). Also, p5CB30 has the largest room temperature storage modulus at 2.6MPa. Curiously, by adding in liquid and removing polymer per unit volume up to 30wt%, the LCE has a better propensity for storing energy elastically.

At temperatures above this rubbery plateau, the three formulations exhibit order loss akin to a glass transition that onsets near their T^* . Resemblant behavior exists in LCEs displaying both smectic C and nematic phases, which suggests that the order loss at both the T^* can be described as a smectic-nematic transition (57). However, it is worth noting that LCE's smectic C phase was contributed by solid crystalline domains, whereas our system has a large liquid component which is not known to exhibit a smectic phase by itself. p5CB10 does not have as blatant a rubbery plateau, though it starts to develop immediately after the glass transition when the slope becomes shallower (ca. 11°C). While undetectable in our DSC measurements, DMA shows that the secondary mesophase with upper bound T^* is observed in p5CB10.

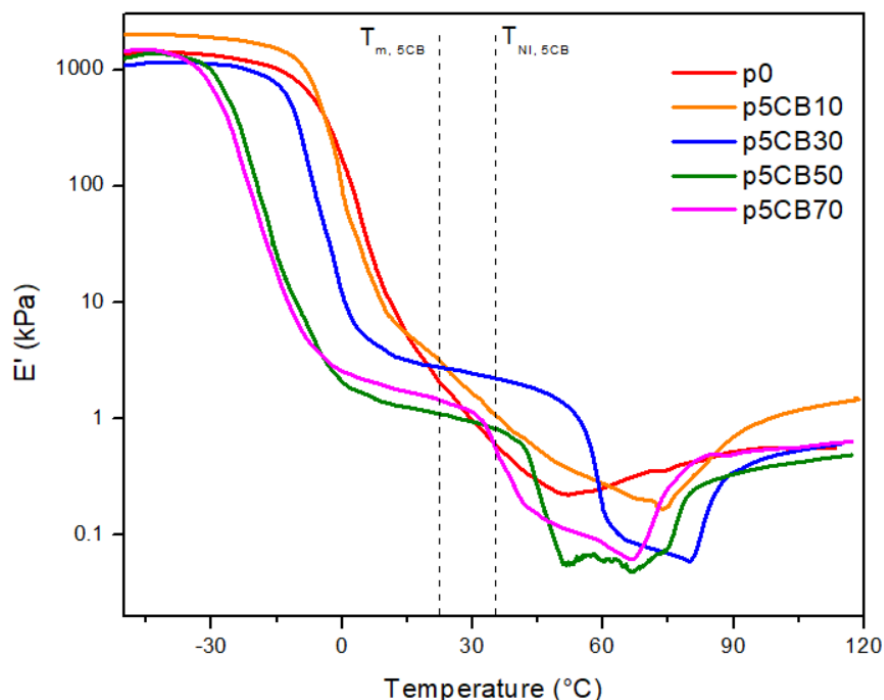


Figure 4-7: 5CB Formulations' Storage Moduli as a function of temperature.

Investigating Figure 4-8 and Figure 4-9, the $\tan\delta$ for p0, p5CB10, and p5CB30 are plotted separately from the p5CB50 and p5CB70 samples due to noise present in the latter two formulations (the source of which is discussed in the next paragraph). P0 displays the previously documented characteristic of polydomain LCEs—a heightened $\tan\delta$ plateau between T_g and T_{NI} , followed by its decline approaching the clearing point (112). All 5CB loaded formulations do not exhibit this plateau and the loss factor decreases at a slower rate—phenomena both attributable to the smaller fraction of nematic elastomer. With orientational interaction between LCE chains as the genesis for the $\tan\delta$ plateau, replacing a fraction of polymer with the LC solvent intuitively diminishes internal viscosity (113). Minor differences observed in transition temperatures between DSC and DMA are explained by differences in when changes onset in thermal and mechanical properties (110). As the temperature is increased beyond the T_g and the temperature window devoid of a $\tan\delta$ plateau, secondary $\tan\delta$ peaks are seen in all 5CB doped formulations and show that chain segmental motion is increasing. These all correspond to the decrease in slope that follows the inflection point after the rubbery plateau: they represent the secondary mesophase's transition to nematic ordering.

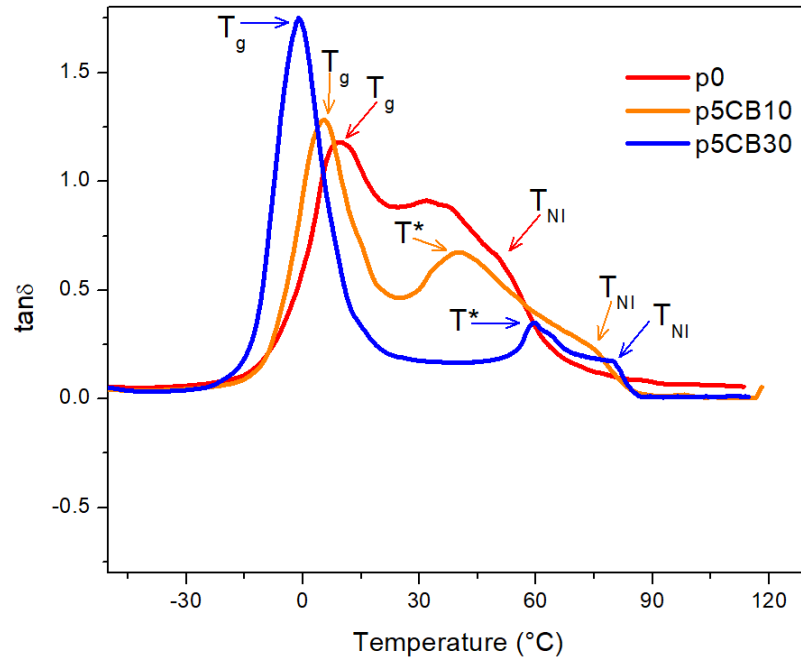


Figure 4-8: $\tan\delta$ for p0, p5CB10, and p5CB30 with labeled T_g , T^* and T_{NI} .

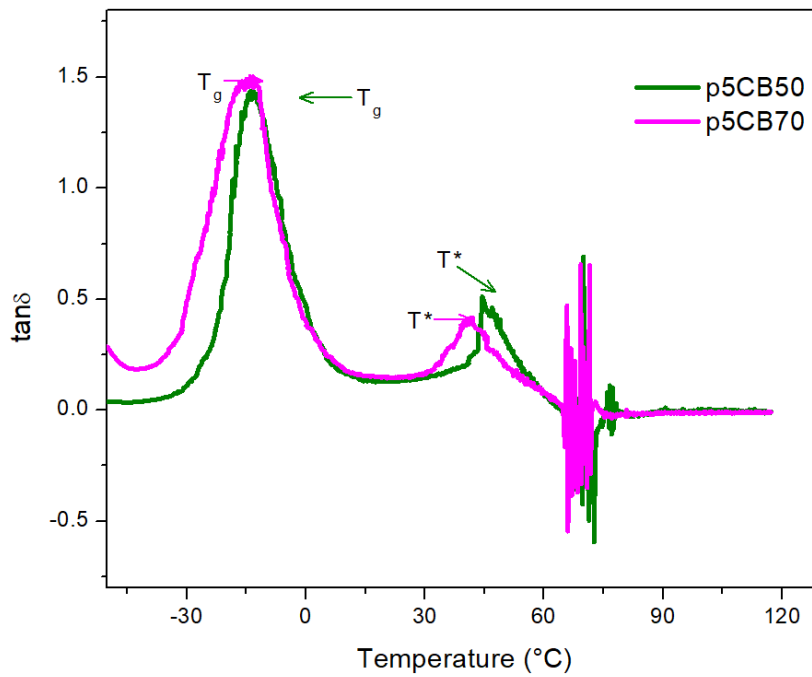


Figure 4-9: $\tan\delta$ for p5CB50 and p5CB70 with labeled T_g and T^* . The T_{NI} is not labeled here due to substantial noise preventing accurate measurement.

Tertiary $\tan\delta$ peaks are seen in p5CB10 and p5CB30 which correspond to the storage moduli' minima, or the T_{NI} . Tertiary $\tan\delta$ peaks are not recorded for p5CB50 and p5CB70 because noise overshadows these transitions. As the clearing point is approached from lower temperatures, the order-disorder transition onsets a few degrees before the E' minimum. During this transition, the sample's stiffness becomes less than the instrument's resolution which produces this noise (114). The sample starts becoming soft once elevated above the glass transition, and the sample's amplitude resulting from the force applied continually increases above T^* to a maximum at the clearing point. Only afterwards does the amplitude decrease back to pre- T^* values, once the stiffer isotropic configuration is adopted. Similar noise and amplitude behavior are registered by p5CB30 to a lesser extent. Figure 4-10 shows this amplitude behavior overlaid with the tan delta functions. Resolving the tertiary $\tan\delta$ peaks for these formulations would involve a separate temperature sweep to encompass the noise-ridden region with a Force Track better suited to such soft specimens rather than 125%. Alternatively, wider specimens with wider clamps such that the sample's stiffness is within the instrument's specifications could be used. However, these are not necessary since p5CB50 and p5CB70's T_{NI} can be obtained from the storage modulus temperature sweep.

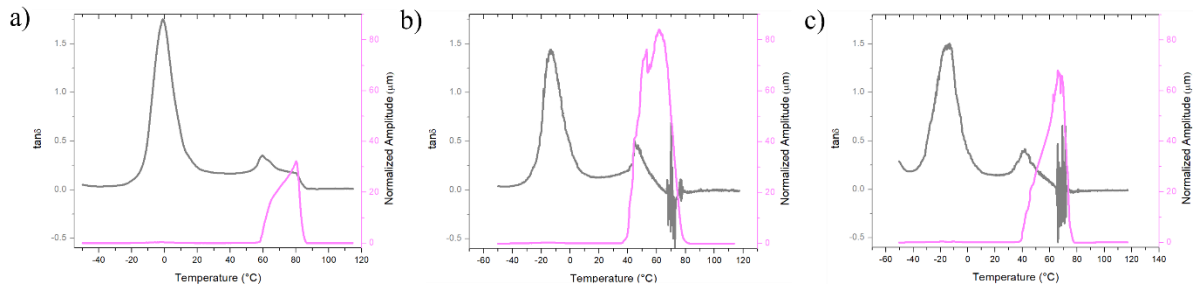


Figure 4-10: $\tan\delta$ and Normalized Amplitude for a) p5CB30, b) p5CB50, c) p5CB70

Below in Table 4-5 are the tabulated transitions, wherein the transition temperature for T_g , and T^* are taken from the $\tan\delta$ graphs and labeled in Figure 4-8 and Figure 4-9, while the T_{NI} is recorded as the temperature corresponding to the minimum right before the storage moduli's slope sharply increases. Excluding the control formulation, all transitions are recorded at higher temperatures than DSC. Aside from the enhanced sensitivity, the ramp rate employed in DMA was slower than for DSC, resulting in the transitions onsetting later. We recall that slower ramp rates for DSC, in contrast, did not resolve T^* . Taken together, there is sufficient evidence that this new mesophase has a higher degree of

crystallinity than the undoped nematic LCE. Additionally, the introduced rubbery plateau resembles LCEs boasting smectic ordering below a nematic mesophase.

Table 4-5: Transition Temperatures from DMA

	T_g (°C)	T^* (°C)	T_{NI} (°C)
p0	10	-	52
p5CB10	5	40	74
p5CB30	-6	57	76
p5CB50	-15	46	75
p5CB70	-14	41	67

4.2.3.3 Coefficient of Thermal Expansion (COTE)

To verify the additional mesophase existence in monodomain samples—as LCE soft actuators are predominantly monodomain—coefficient of thermal expansion (COTE) measurements were conducted (44). Thermal expansion measurements are substantially more evident in monodomain specimens than polydomain samples since their globally oriented state decreases as the temperature is increased to reach the T_{NI} . To prepare monodomain LCEs, each formulation was uniaxially stretched until it was fully transparent, and then photopolymerized under UV light. These strains are further detailed in 4.2.4.1 and 4.2.5.3. Parallel and perpendicular length changes in monodomain samples are seen in Figure 4-11 (m0), Figure 4-12 (m5CB10), Figure 4-13 (m5CB30), Figure 4-14 (m5CB50), and Figure 4-15 (m5CB70). Positive length changes are observed perpendicular to the alignment direction (D_{\perp}), while negative length changes occur parallel to the director (D_{\parallel}). Overall, larger shape changes are evident in 5CB-loaded formulations. Two prominent slope changes are detected in all formulations save m0. The lower and higher temperature slope changes are attributed to T^* and T_{NI} , respectively. Changes in the thermal contraction/expansion rate are known to signify mesophase transitions, confirming the new mesophase is retained in monodomain LCEs (115). While the change in deformation rate associated with T^* is close to the corresponding temperatures measured from DMA and DSC of polydomain samples, the change in this rate associated with the T_{NI} manifests at substantially larger temperatures. This is due to the 2nd stage polymerization masking the transition,

necessitating more heat to disrupt (10). Taken together, the three experiments for thermal analysis confirm the order-disorder transitions and are indicative of a new mesophase created from dopant loading.

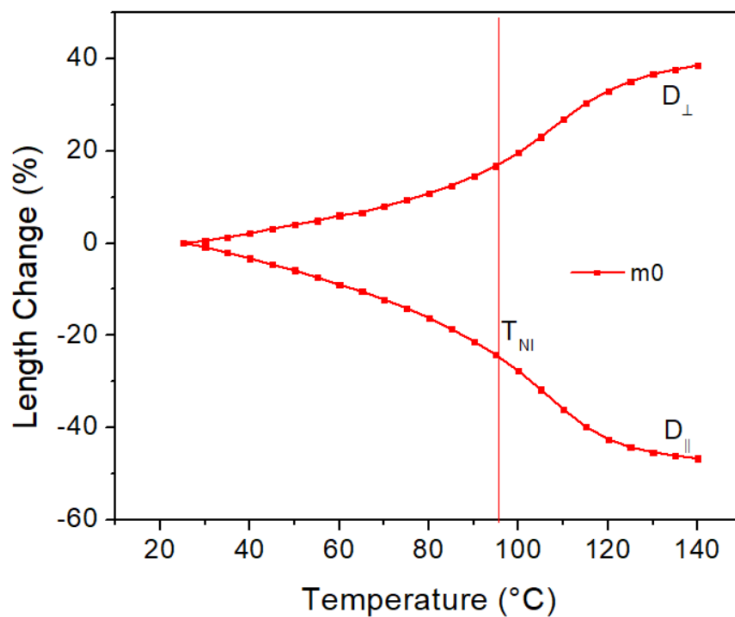


Figure 4-11: Thermal Expansion of m0.

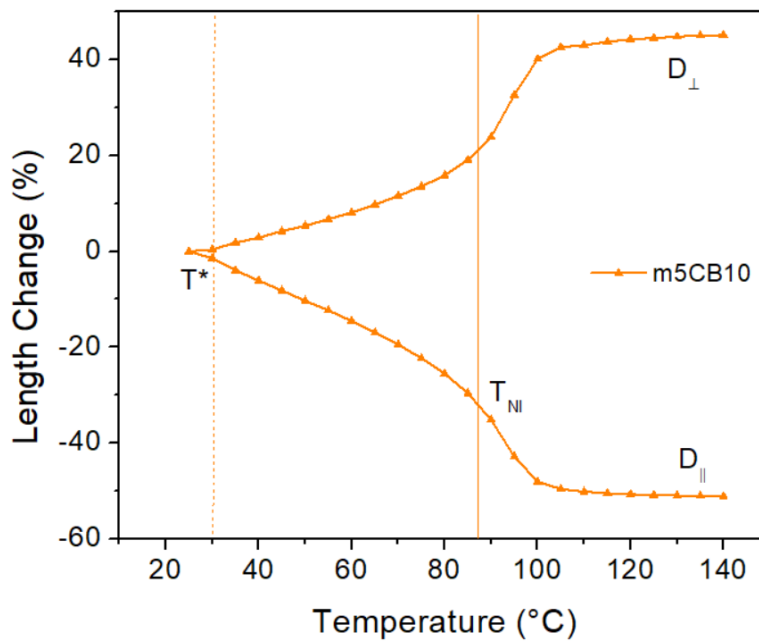


Figure 4-12: Thermal Expansion of m5CB10.

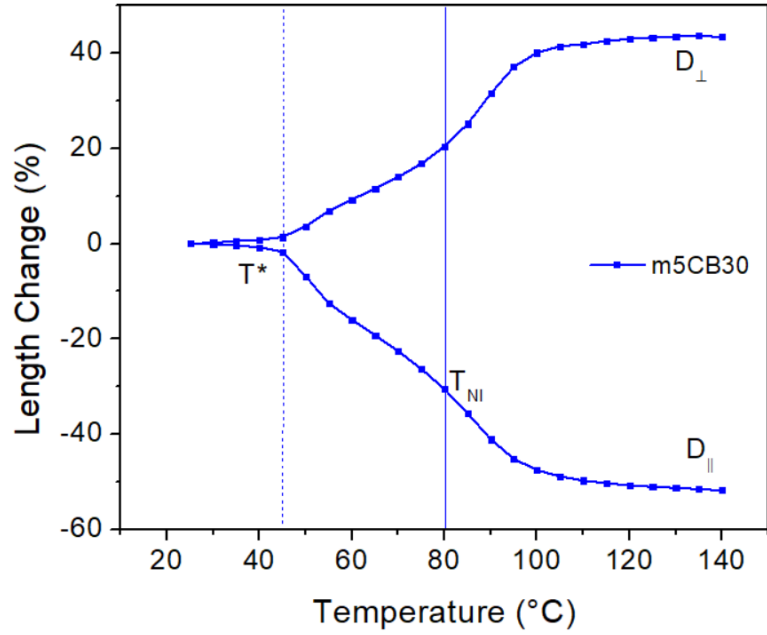


Figure 4-13: Thermal Expansion of m5CB30.

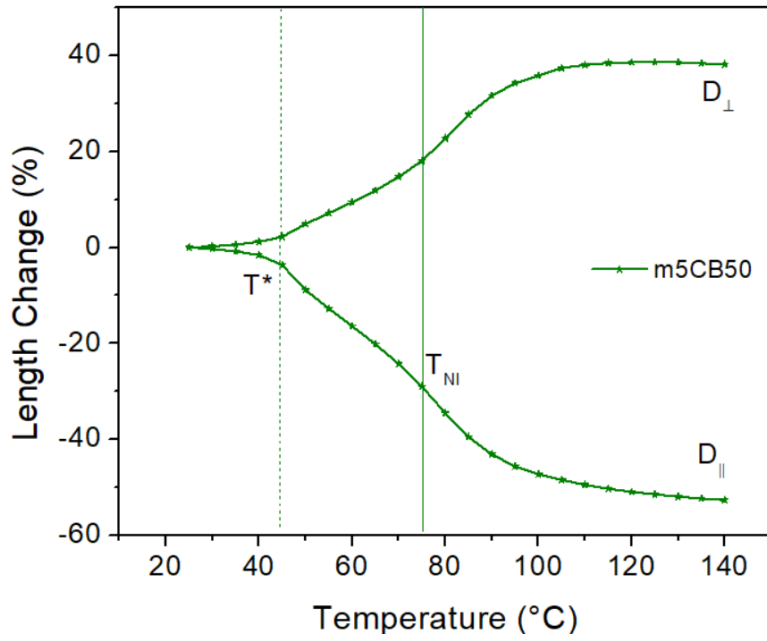


Figure 4-14: Thermal Expansion of m5CB50.

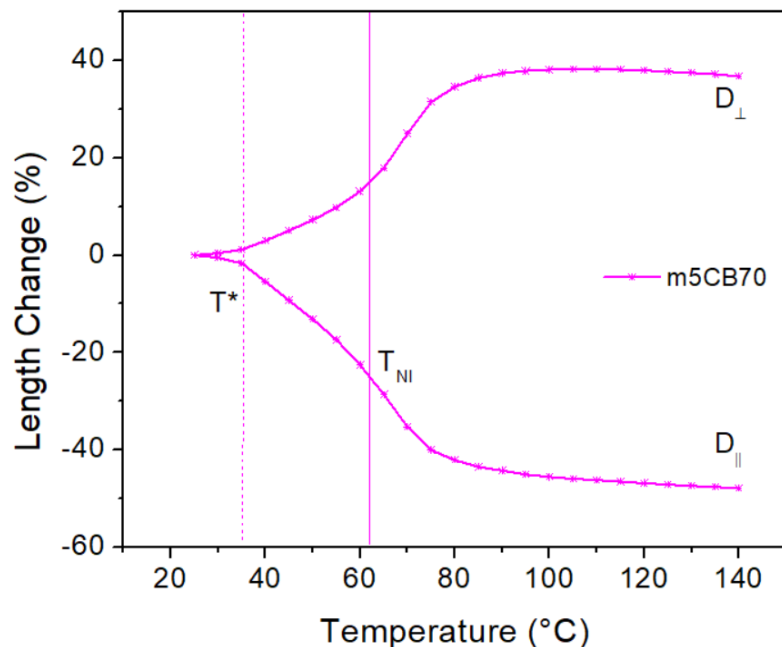


Figure 4-15: Thermal Expansion of m5CB70.

4.2.4 Determining the Mesophase Nature

In section 4.2.3 substantial evidence was obtained to confirm the existence of a mesophase at temperatures between the glass transition and the nematic phase that develops from 5CB loading. It was also established that similar trends are documented in literature for thiol-acrylate LCEs boasting microphase-separated smectic domains within a macroscopically uniform LCE. However, the trend similarity is not sufficient to claim the mesophase below T^* as smectic. This is because direct information on the microstructural ordering has not yet been acquired. Understandably, higher degrees of ordering and crystallinity were observed via the introduced rubbery plateau in DMA and the extra endothermic peaks, but such data do not precisely inform how the 5CB and thiol-acrylate macromolecules pack. Knowledge of their arrangement is imperative for elucidating what mesophase is being observed. This is done through x-ray scattering, a crystallographic technique in which mesophases elicit characteristic diffraction patterns and associated length scales.

4.2.4.1 Wide-Angle X-ray Scattering (WAXS)

Unraveling the enigmatic nature of the additional mesophase required Wide-Angle X-ray scattering (WAXS) to determine if characteristic LC patterns are observed, and to measure the distances over

which LC ordering persists. WAXS was performed at 25°C for all formulations. Figure 4-16 shows the two-dimensional (2D) diffraction patterns for unstretched polydomain samples (Column 1), samples at 50% engineering strain (Column 2), and samples at the minimum strain for becoming entirely monodomain (Column 3). The minimum strain for inducing full monodomain order was determined qualitatively by stretching the polydomain specimen until it became entirely visibly transparent. This threshold is more quantitatively examined later in section 4.2.5.3. The corresponding 1-dimensional (1D) radially integrated intensities are shown in Figure 4-17, with the polydomain data in Figure 4-17a, the 50% strained data in Figure 4-17b, and the fully monodomain data in Figure 4-17c.

The polydomain diffraction patterns and 1D integrated curves are discussed first. All polydomain diffraction patterns possess diffuse rings at wide angles, which result from disorder in polymerized mesogens (1.4\AA^{-1}) and flexible spacers (3.1\AA^{-1}) (116). Though not obvious, the 3.1\AA^{-1} ring is seen in Figure 4-16 where the dark blue intensity fades to black at the 2D pattern edges. The diffraction patterns of only the doped formulations show brighter regions at small angles, which correspond to the more gradual decline of the integrated curve's slope when compared to p0 (ca. $0.1\text{-}0.5\text{\AA}^{-1}$). This indicates that in the polydomain state, more molecular ordering is present over these q-values compared to p0, but without sufficient long-range order for the existence of a novel mesophase, as would be evidenced by small-angle scattering rings (59).

Through uniaxially stretching the samples 50% to introduce some monodomain order, the 2D patterns in the second column of Figure 4-16 and 1D integrated intensities in Figure 4-17b are obtained. Expectedly in all samples, the diffuse mesogen ring starts to collapse into arches from RM257 realignment with the strain, yielding the collinear global director \mathbf{n} . Intriguingly, p5CB30, p5CB50, and p5CB70 feature sharp Bragg scattering reminiscent of smectic-A ordering between $0.15\text{ - }0.17\text{\AA}^{-1}$ and $.31\text{-}.33\text{\AA}^{-1}$ (18, 117). Since the latter peak is double the q-value of the former, this 2nd order reflection evidences lamellar structuring which further confirms smectic ordering (118, 119). Though not as visible in p5CB10 (Figure 4-16e), noticeably brighter regions exist at small angles compared to its unstretched state (Figure 4-16d).

Stretching samples to strains where they are now visibly transparent and more monodomain produces the results in the third column of Figure 4-16 and Figure 4-17C. All nematic arches collapse further, and in p5CB10 a Bragg peak is now visible. Analogous strain-induced order enhancement evidenced by the development of small angle peaks is documented in literature for an LCE system with flexible

spacers and polymerized mesogens (116). However, this system from literature is smectic both in its polydomain and monodomain states and only the small angle peaks become more intense. Conversely, the 5CB loaded formulations are nematic in the polydomain state: only when strain is applied does the smectic pattern evolve. Alongside the fact that no small-angle peaks develop in the undoped LCE at any strains, it is concluded that the small-angle peaks arise from 5CB. The strain values used were: p0: 60%, p5CB10: 115%, p5CB30: 235%, p5CB50: 95%, and p5CB70:40%. The stretching direction is labeled in Figure 4-16C and is the same for all monodomain 2D patterns. All 1D peaks relevant to mesogens are labeled p_1 ($\sim 0.17 \text{ \AA}^{-1}$), p_2 ($\sim 0.35 \text{ \AA}^{-1}$), and p_3 ($\sim 1.4 \text{ \AA}^{-1}$) and are denoted in Figure 4-16I. Note the same peak naming convention is used for all formulations.

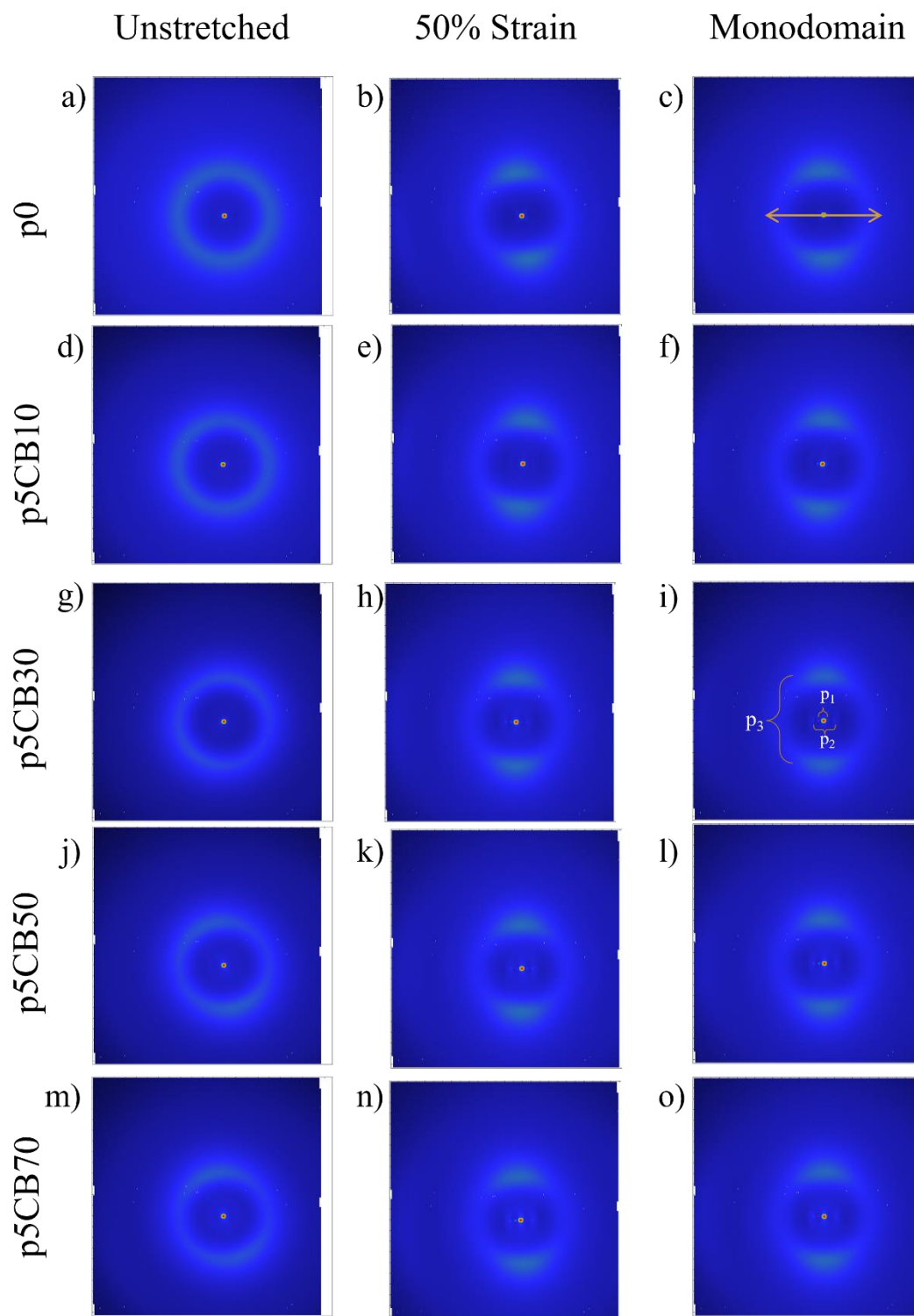


Figure 4-16: 2D Diffraction Patterns for 5CB Doped LCEs.

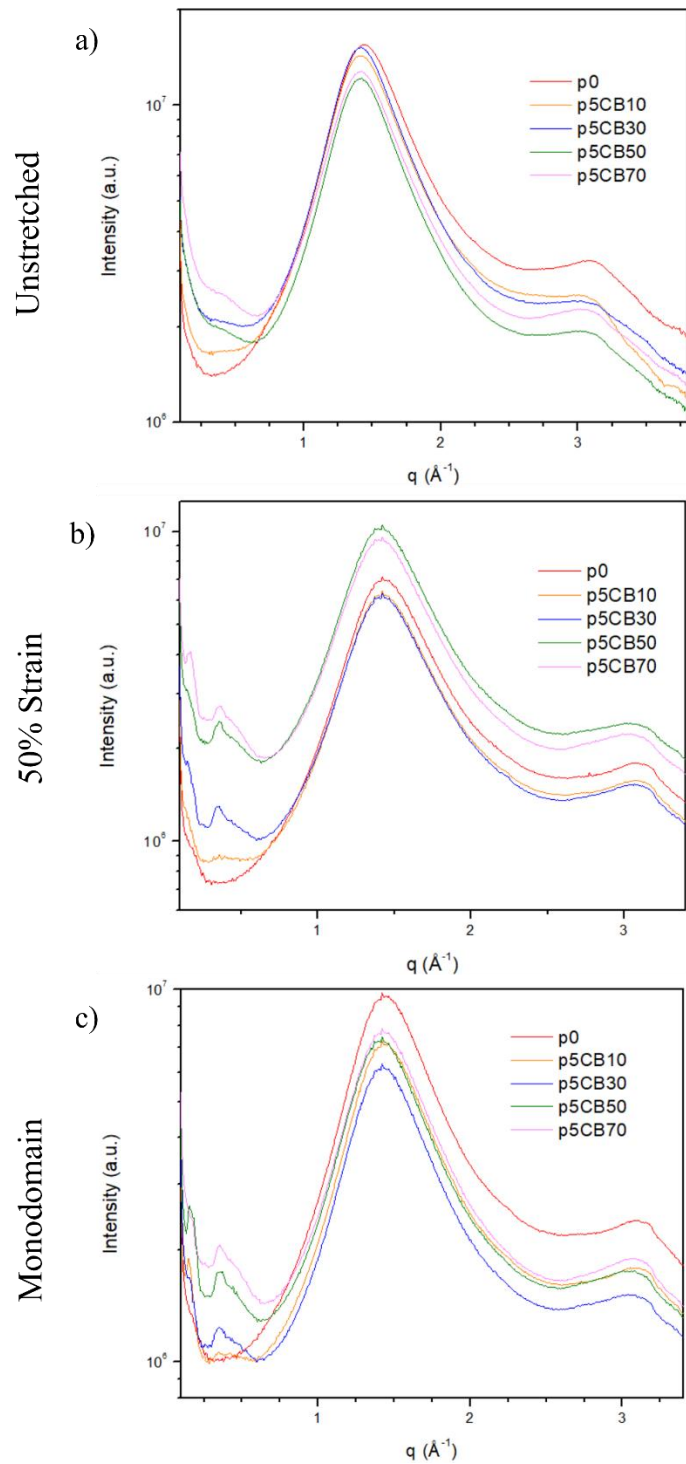


Figure 4-17: 1D Integrated Intensities for 5CB Loadings

4.2.4.2 Order Parameters

A quantitative explanation of the extent of mesogen alignment within each LCE was determined by the orientational order parameter, S . Values are tabulated below in the same arrangement as diffraction patterns in Figure 4-16. As a clarifying example, for p0, Column 1's order parameter value was obtained from an unstretched sample, Column 2's value from a sample stretched to 50%, and Column 3's from a sample stretched to the minimum requisite strain for that formulation to become visibly transparent (60%). P5CB10, p5CB30, and p5CB50 exhibit proportional increases in S with strain, which is due to the randomly oriented LC domains rotating towards the stress direction. P0 and p5CB70 also demonstrate this behavior with their second largest measured strains (50% and 40% respectively). However, when stretched 10 more percent, both their order parameters decrease. Since these strains are well below failure (see section **Error! Reference source not found.**), this behavior is unlikely due to fracture. It could be attributed to small air bubbles/defects present in the sample obstructing chain mobility as the bubbles become more oblong. Interestingly, p5CB30 has the smallest S value of all polydomain formulations but evolves to having the largest order parameter of all. A rationale to explain this behavior is discussed in the next section (4.2.4.3).

Table 4-6: Order Parameters of 5CB-doped LCEs

Formulation (Strain)	Column 1	Column 2	Column 3
p0 (0%, 50%, 60%)	0.34	0.64	0.63
p5CB10 (0%, 50%, 115%)	0.41	0.64	0.65
p5CB30 (0%, 50%, 235%)	0.28	0.65	0.67
p5CB50 (0%, 50%, 95%)	0.42	0.64	0.65
p5CB70 (0%, 50%, 40%)	0.48	0.62	0.64

4.2.4.3 D-Spacings and Correlation Lengths

We now endeavor to determine the strain-induced molecular arrangement. This is approached by first detailing the polydomain d-spacings and correlation lengths. All polydomain samples only display p_3 ($\sim 1.4\text{\AA}^{-1}$), whose d-spacing is consistently 4.4-4.5 \AA . This distance is related to an aromatic ring width—or in this system the molecular width, and describes a lateral intermolecular distance commonly

observed in nematics (97, 120). The associated correlation length ranges from 12-13Å, meaning that the transverse ordering of mesogens (i.e., along their widths) extends at most to two more neighboring LC molecules. Schematically this correlation length is illustrated in Figure 4-18.

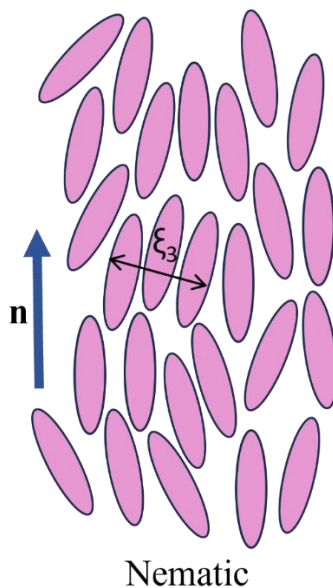


Figure 4-18: Representative Transverse Correlation Length due to Nematic Ordering.

Considering the monodomain LCEs, their d-spacings and correlation lengths for the first and third peaks are presented in Table 4-7. The first subscript denotes the peak to which the metric belongs, while the second subscript “X” is a placeholder for the corresponding formulation (e.g., $\xi_{3, p5CB10}$ is the correlation length for peak 3 of p5CB10). Peak 2 is not included since it is a reflection of Peak 1 that arises from lamellar ordering and indicates multiple stacked smectic layers. Commencing with the d-spacing of p_3 for all monodomain LCEs, this provides the intermolecular distance in the equatorial direction (i.e., perpendicular to the uniaxial strain). This value is unchanged from the polydomain samples, since 5CB and RM257 molecules are not compressible along their widths. Meridional peaks (p_1 and p_2) arise from longitudinal interlayer distances and describe the smectic layer spacing (97). Analyzing the 5CB-doped formulations’ d-spacings, for p_1 all are consistently between 37-39Å, which is comparable to the length of two 5CB molecules (40Å) when accounting for the flexibility of their alkyl chains (121). We thus postulate that the interlayer spacing of these quasi-smectic domains is approximately two 5CB molecules long. Noticing that $d_{1,x}$ maintains this range regardless of strain value suggests that the smectic layers are fixed at this separation distance. Also, recalling no pseudo-

Bragg peaks exist in p0, the matrix chains in all doped formulations can function as the lateral domain boundaries to reinforce the LC solvent packing through enhanced dipole interactions.

Correlation lengths are another WAXS peak-derived metric for how long the ordering extends in the same direction as their corresponding d-spacings. Thus, p_1 's correlation length represents how far ordering persists in the longitudinal direction parallel to stretch, and p_3 in the equatorial direction perpendicular to stretch. Considering p_1 , when all LCEs are stretched to the same strain (50%), the correlation lengths are within 7Å. We observe that this distance is relatively similar across all formulations., though the largest $\xi_{1,x}$ is displayed by p5CB30, which mirrors the order parameter measurements. $\zeta_{1,p5CB50}$ is the second largest correlation length, followed by $\zeta_{1,p5CB10}$. P5CB70 has the smallest ζ since its majority liquid fraction prevents order from transcending a longer distance compared to a system with a majority of nematic elastomer chains. Overall, 50% strain is enough to induce smectic ordering in the doped LCEs through chains reorienting and compressing the 5CB molecules into this packing arrangement due to the uniaxial stress. When samples are stretched to their respective strains required for becoming visibly transparent, $\zeta_{1,x}$ for p5CB10, p5CB30, and p5CB50 increases. $\zeta_{1,p5CB70}$ is the only one that does not increase, which is because its requisite strain for becoming monodomain is 40%. This signifies that its correlation length at 50% strain should be larger, which is indeed the case. $\zeta_{1,p5CB30}$ is substantially longer than the other correlation lengths on account of its strain for becoming monodomain being that much larger. P5CB30 requiring a markedly larger strain for becoming monodomain is also demonstrative of the smectic domains having a higher energy barrier for realignment. 30wt% loading of 5CB is inferred to be the optimal doping amount for augmenting the LCE's molecular order. This inference is supported by DSC results, where p5CB30 has the largest endothermic peak for T*, and DMA data, in which p5CB30 has the highest rubbery plateau. At this loading, 5CB enhances chain mobility by diminishing inter-chain friction, but also exists in sufficient quantities for forming longer smectic domains. Returning to the order parameter measurements, p5CB30's order parameter may be the smallest at 0% strain since smectic regions that are not aligned with the director detract from the order parameter more than unaligned nematic regions. In a polydomain state, it is more likely that smectic domains are not oriented in one global direction, whereas in a polydomain state comprised of only nematic regions, the mesogens are inherently less collinear within their domain, meaning that in the bulk there a greater probability of all molecules being oriented in a particular direction.

Similarity in the transverse correlation lengths ($\xi_{3,x}$) amongst the three formulations is observed regardless of alignment degree; this is due to the values arising from RM257's benzene rings. Only p5CB10 at its monodomain strain does not have $\xi_{3,x}$ being within 11-12Å, though it is worth acknowledging the difference of 3Å is infinitesimal.

Table 4-7: D-spacings (d) and Correlation Lengths (ξ) for p₁ and p₃

	$d_{1,x}$ (Å)	$d_{3,x}$ (Å)	$\xi_{1,x}$ (Å)	$\xi_{3,x}$ (Å)	$\frac{\xi_{1,x}}{d_{1,x}}$	$\frac{\xi_{3,x}}{d_{3,x}}$
Stretched to 50%						
p0	-	4.5	-	10.9	-	2.4
p5CB10	39.0	4.5	95.3	10.7	2.4	2.4
p5CB30	39.0	4.5	101.3	11.3	2.6	2.5
p5CB50	39.0	4.5	100.1	11.3	2.6	2.5
p5CB70	39.0	4.5	94.4	11.5	2.4	2.6
Stretched to Entirely Monodomain Strain						
p0	-	4.5	-	11.5	-	2.6
p5CB10	38.5	4.5	99.7	7.9	2.6	1.7
p5CB30	38.6	4.5	144.9	11.7	3.8	2.6
p5CB50	37.1	4.5	108.6	11.3	2.9	2.5
p5CB70	38.1	4.5	87.3	11.2	2.3	2.5

The enhanced mesophase order has been described as smectic because of the characteristic 2D pattern and the 5CB-loaded LCEs possessing similarities to LCEs with both nematic and smectic phases. However, it is not certain that this phase can be labeled as smectic. This is because it is equally important to examine the correlation length alongside the d-spacings and WAXS intensities to assess the type of induced mesophase. The length scale over which the molecular ordering persists establishes whether a long-range fully-fledged smectic phase exists, or rather short-range smectic ordering within a less ordered phase is present as is the case in cybotactic systems (97, 122). Consequently, we herein

examine the correlation lengths relative to their respective d-spacings. For p_3 the ratio of $\frac{\xi_{3,x}}{d_{3,x}}$ describes over how many molecular widths the nematic ordering persists, while for p_1 , $\frac{\xi_{1,x}}{d_{1,x}}$ defines how many smectic layers exist in these domains of higher ordering. The nematic peak (p_3) ratio is maintained regardless of formulation, suggesting any transverse ordering of LCE chains extends at most to two more neighboring LC molecules. The ratio $\frac{\xi_{1,x}}{d_{1,x}}$ allows for comparison with commensurate mesophase data in literature. Exploring the ratio related to peak 1, the correlations and corresponding d-spacings are of the same order for all 5CB-loaded formulations, which is in stark contrast to a fully-fledged smectic mesophase (97). Rather, this is characteristic of short-range smectic order within the nematic phase, or cybotacticity (122). This evidence is supported by known LCEs with long-range smectic and nematic mesophases having much more distinct endothermic peaks at their transitions (57, 59). Importantly, since no peaks were detected in the equatorial direction apart from the polymerized mesogenic rings, the transverse correlation length of the short-range smectic domains cannot be studied by analyzing the correlation length to d-spacing ratio: this is treated in the next section. Overall, the doped LCEs uniquely display strain-induced cybotacticity comprised of short-range SmA domains within the nematic phase.

4.2.4.4 Size of Phase-Separated Dopant Region

Considering there were no x-ray signals conveying the extent of transverse smectic ordering, we now aim to address this gap. The cryo-SEM study in section 4.2.2.5 showed notable phase separation only observed in 70wt% loading, with micron-sized voids darker than the LCE present. These voids are attributed to extracted biphenyl solvent, showing that dopant-rich and dopant-depleted regions exist within the macroscopically homogenous LCE. However, the measured cybotactic domain lengths in the previous section are substantially smaller than the voids seen in p5CB70's cryo-SEM study. The voids suggest that such regions in p5CB30 are smaller than the SEM's resolution capabilities. To connect the inferences from cryo-SEM with WAXS correlations, we endeavor to calculate p5CB30's phase-separated region size by determining the transverse dimension of the cybotactic regions. This lateral dimension can inform the extent of transverse smectic order. All 5CB-loaded formulations have lateral dimensions calculated in the same manner, but it was chosen to focus on p5CB30 since it has the largest order parameter and longitudinal correlation length.

Focusing on p5CB30, we consider the phase-separated 5CB to adopt spherical domains in the polydomain LCE—this is due to local LC domains having random orientation. From uniaxial stress, the LCE chains and biphenyl molecules rotate and align such that 5CB forms short-range smectic domains within the nematic elastomer. Induction of the smectic order manifests through the sphere morphing into an equivalent volume ellipsoid with the long axis $\zeta_{l,p5CB30}$. With conservation of volume in mind, the phase-separated domains' radii in the polydomain state, $r_{poly,x}$, can be back-calculated from the peak 1 correlation. For p5CB30, $r_{poly,p5CB30} = 21.6\text{\AA}$. Considering the calamitic nature of 5CB endowing the ellipsoid with equivalent short axes, the elongated cybotactic regions in p5CB30 at its monodomain strain have short axes radii $r_{mono,p5CB30} = 11.8\text{\AA}$. These monodomain radii describe the transverse extent of SmA ordering within the cybotactic domains and substantiate that short-range smectic order is present.

Figure 4-19 schematically visualizes this calculation by showing three scales of abstraction: the bulk LCE (seen under cross-polarizers), the phase-separated 5CB regions within the LCE, and the molecular arrangement within the cybotactic 5CB domains. The bulk polydomain p5CB30 is seen in Figure 4-19a (note that the polydomain LCE is dark under cross-polarizers and incident illumination was required for imaging). P5CB30's nanoscale structure is comprised of polymer chains with interspersed spherical 5CB regions of radius $r_{poly,p5CB30}$ (Figure 4-19b). Figure 4-19c shows 5CB molecules organized into clusters of at most three molecules based on $\zeta_{3,p5CB30}$ with no preferred alignment. Transitioning into the monodomain state, the bulk LCE becomes bright under cross-polarizers and does not require illumination (Figure 4-19d). This is due to the applied stress forcing mesogens to reorient, elongate, and adopt a collinear global director (Figure 4-19e). The LCE's dimensions perpendicular to the strain direction decrease, compressing the spherical 5CB regions in orthogonal directions and forcing an ellipsoidal conformation. Consequently, the 5CB molecules organize into short-range smectic domains with length $\zeta_{l,p5CB30}$, and lateral diameter $D_{mono} = 2 * r_{mono,p5CB30}$ maintained both by this mechanical compression and increased dipole interactions from myriad polar end groups in proximity (Figure 4-19f). Contributors to dipoles and induced dipoles longitudinally are the cyano, phenyl, and carbonyl groups.

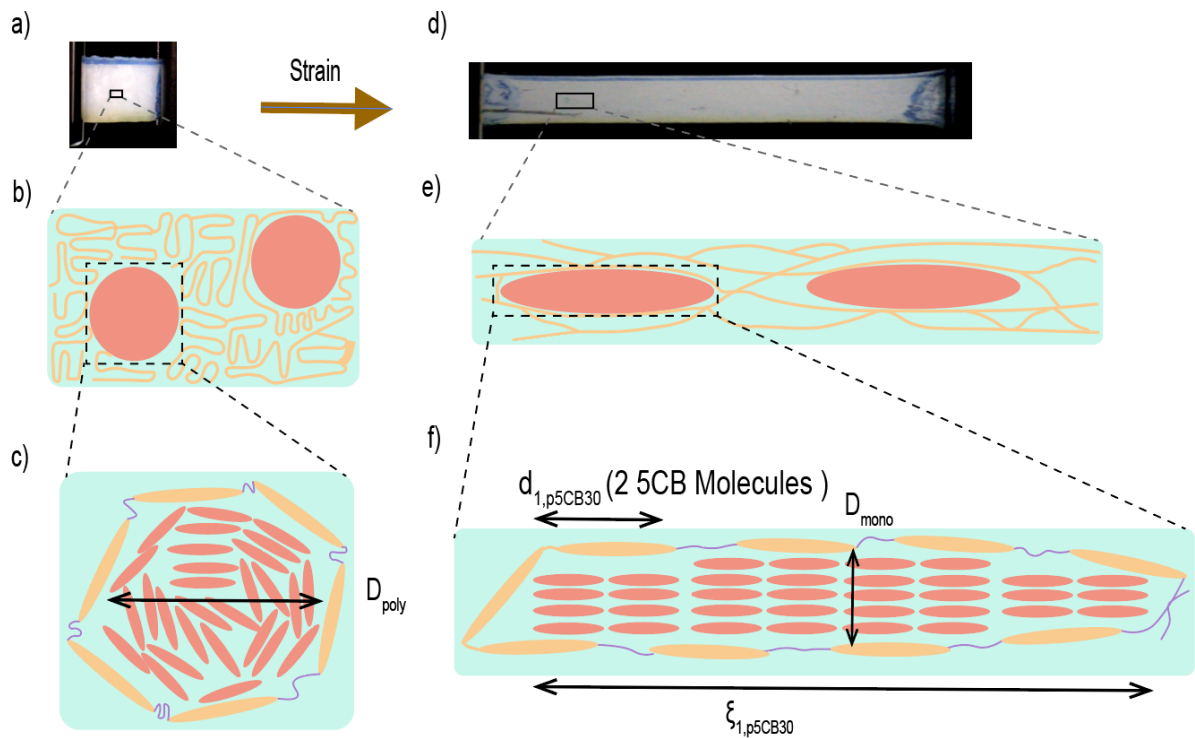


Figure 4-19: Phase-separated 5CB domain dimensions in p5CB30 polydomain (Left) and monodomain (Right) LCEs. Note in a) the POM's reflection light source is on to illuminate an otherwise dark polydomain sample under cross-polarizers, while in b) only the transmission light source is on.

Here we revisit the cryo-SEM image of p5CB70 in Table 4-3 and the possibility of the light and dark void pattern representing phase-separated 5CB. Considering the correlation length of monodomain p5CB70 (87.3\AA), the radius of the phase-separated regions in p5CB70 can be back-calculated just as with p5CB30 and is $r_{poly,p5CB70} = 31.2\text{\AA}$. Both dimensions are orders of magnitude smaller than the light and dark regions observed under cryo-SEM. However, considering the high loading percentage of 5CB and its miscibility with the LCE, both swelling and phase separation are postulated to occur (18). Phase separation is seen both in the cryo-SEM in Table 4-3 and WAXS data, albeit with different size scales.

4.2.5 Nanoscale Order Influence on Mechanical Properties

4.2.5.1 Polydomain Tensile Tests

Macroscopic augmentations conferred by the strain-induced cybotacticity on the mechanical properties were examined through tensile testing of the polydomain formulations. Since polydomain thiol-acrylate LCEs are known to crystallize over time and contain unreacted acrylate groups that can thermally polymerize, it was crucial to examine how the mechanical properties develop as a function of time. The following figures (Figure 4-20, Figure 4-21, Figure 4-22, Figure 4-23, and Figure 4-24) show how the control and 5CB-loaded formulations develop mechanical strength when tested every 24 hours for five days post-quenching ($n=2$ per formulation). Specimens were all heated and cooled above their T_{NI} on a hot plate before tensile testing to remove residual crystallization. All formulations show the development of a soft-elastic plateau (SEP) and strain hardening over the testing period, with the steepest strain hardening recorded on Day 5. As more 5CB is introduced, the SEP constitutes a larger percentage of the whole stress-strain curve. Strain hardening is associated with polymer chains becoming sufficiently uncoiled at high strain, requiring more load for further deformation. Day 5 is also when p5CB50 and p5CB30 display the highest SEP, indicative of a larger threshold stress required for uniaxial elongation with no additional stress. Intriguingly, a linear elastic region (LER) evolves by Day 3 in p5CB30 and maximizes by Day 5, implying a markedly larger resistance to initial loading. Bearing in mind that p5CB30 had the highest degree of cybotacticity, this resistance is related to a higher energy barrier for inciting rotation of the short-range smectic domains. The LER introduction can also be described as adding mechanical resiliency to the LCE, where resilience is a material's propensity to store and release energy elastically. LERs have been observed in smectic LCEs previously (51, 59, 123) and corroborate the observed behavior of p5CB30.

It is important to discuss batch variability in this study. Since the thiol-acrylate polymerization is a random process, the multiplicity of generated LC domains that comprise the polydomain state varies amongst batches. Stress-strain behavior will also vary amongst batches as a result and specimens will have different values at failure. This is why each formulation was tested with repetition. Regardless of batch variability, the behavior conferred by 5CB loading was always observed.

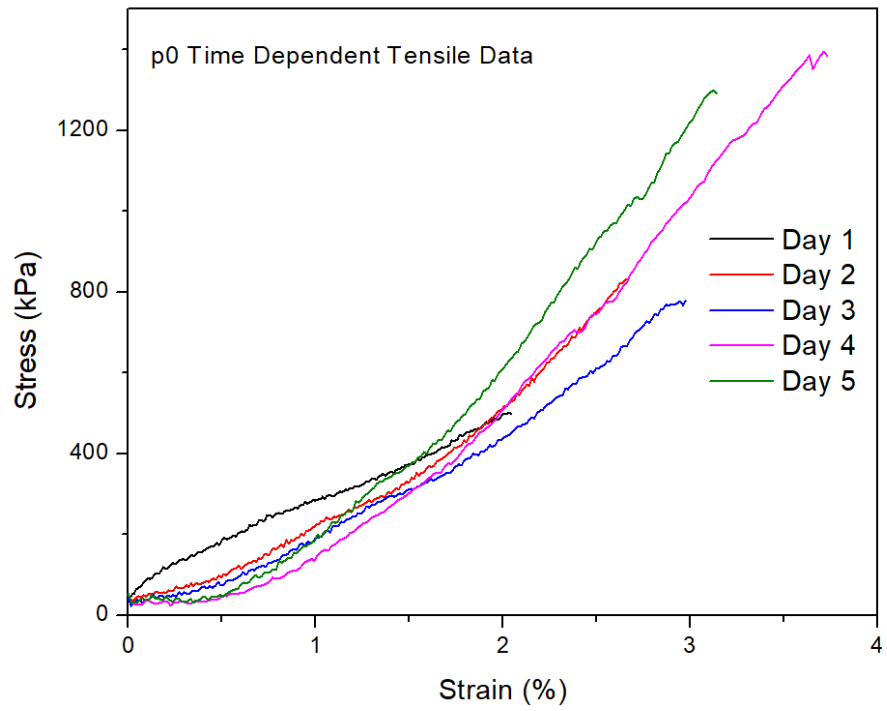


Figure 4-20: Five Day Tensile Data of p0.

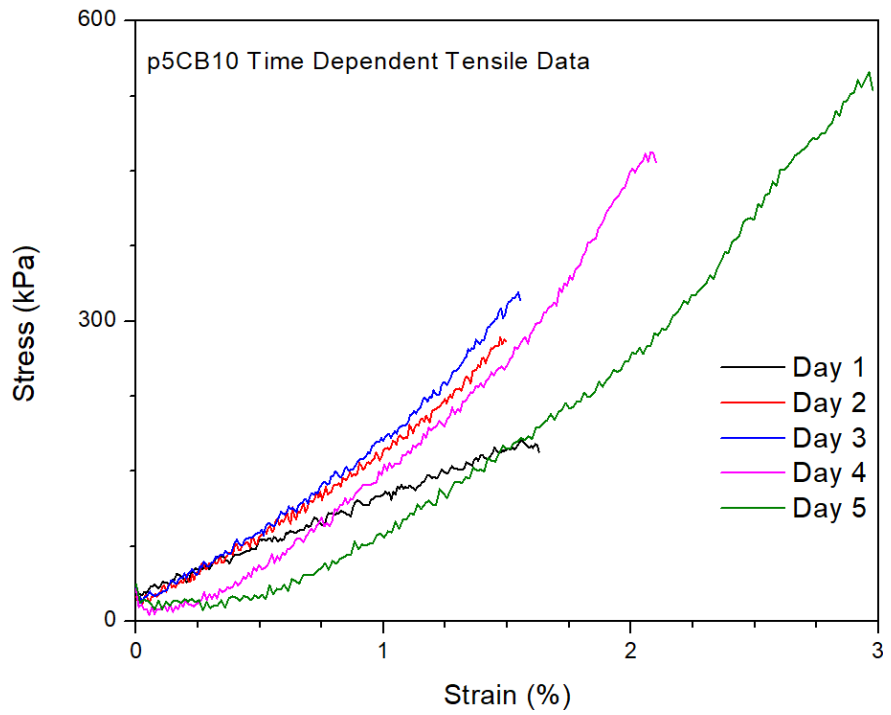


Figure 4-21: Five Day Tensile Data of p5CB10.

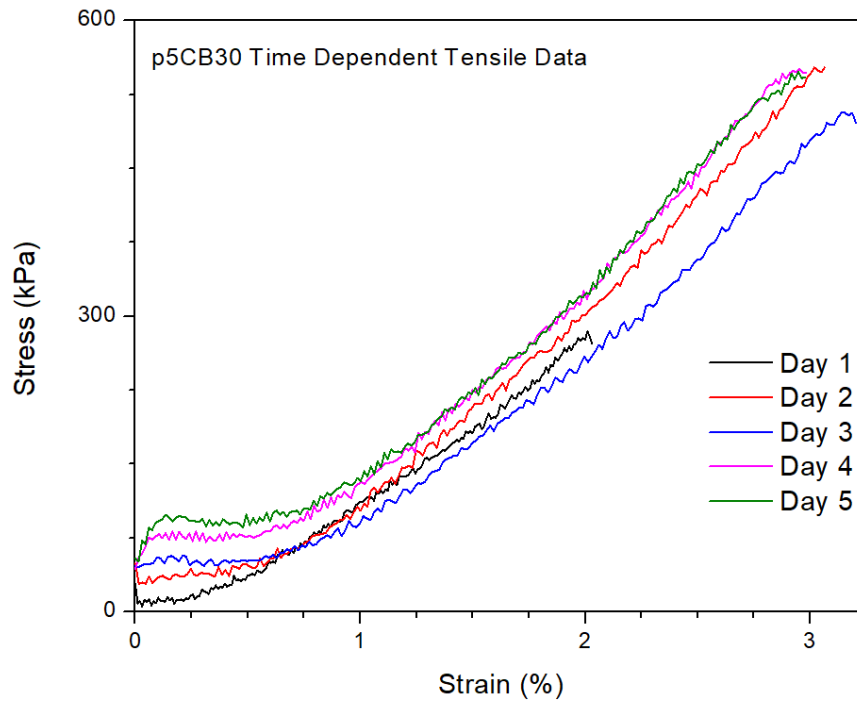


Figure 4-22: Five Day Tensile Data of p5CB30.

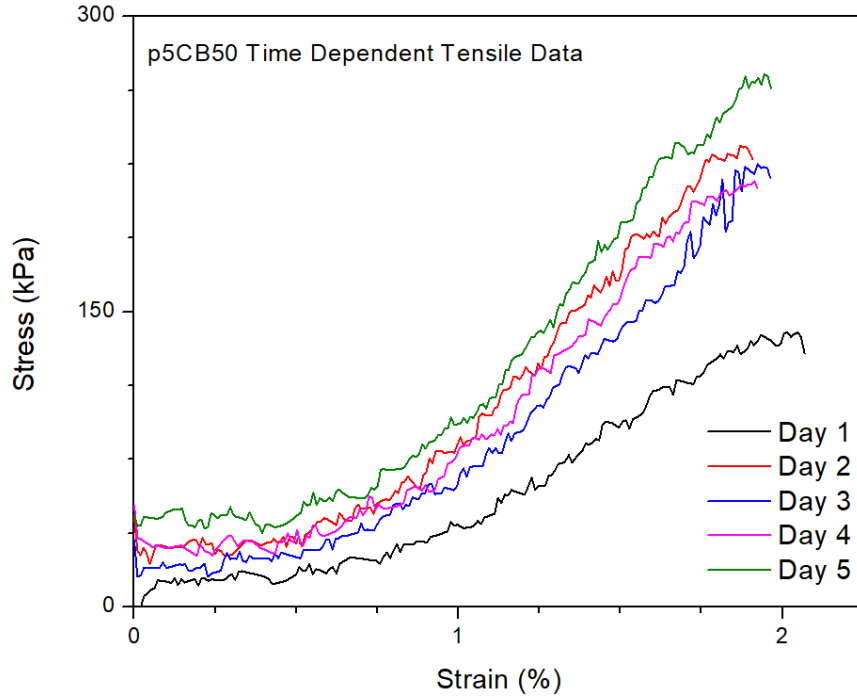


Figure 4-23: Five Day Tensile Data of p5CB50.

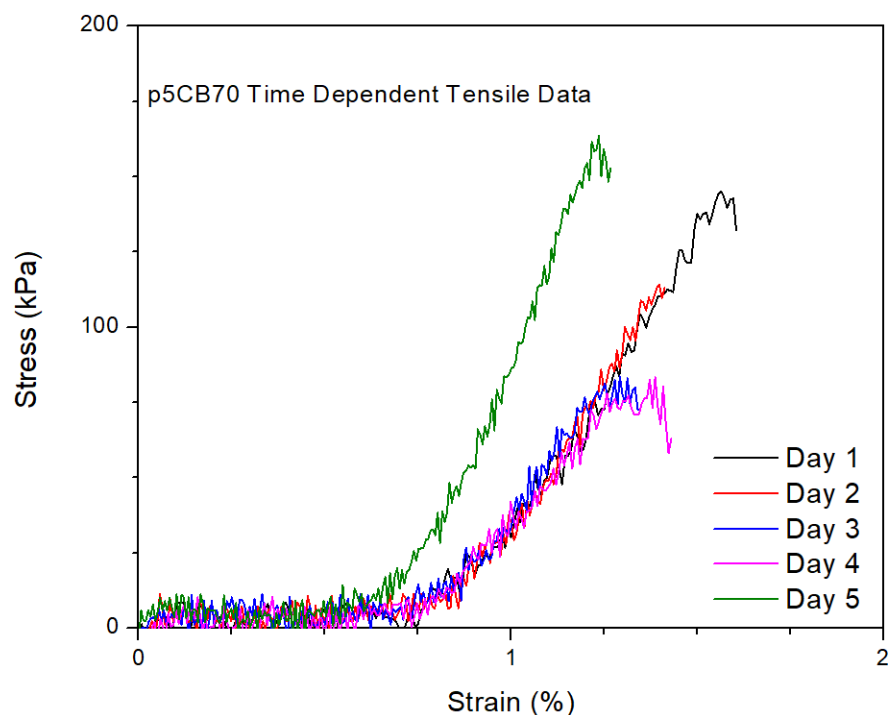


Figure 4-24: Five Day Tensile Data of p5CB70.

To compare the tensile behavior amongst all formulations, the stress-strain curve from Day 5 is overlaid below in Figure 4-25 with an inset up to 100% strain. 5CB loading decreases the failure strain—a trend expected since the fraction of polymer chains to stretch is diminished—and increases the elongation experienced at constant strain, as evidenced by flatter SEPs. P0 has the largest tensile strength since having the highest fraction of polymer chains intuitively requires a larger load for failure. Intriguingly, p5CB30 is the stiffest formulation and toughest until ~95% strain, which is explained by the WAXS and thermal studies. The elastic modulus for p5CB30 is 413kPa. Since p0 has no LER, its moduli are reported for comparison to p5CB30 at p5CB30’s yield point, 100% strain, and the respective failure strains in Table 4-8. The toughness for p0 and p5CB30 are measured as 2035 kJ/M³ and 758 kJ/M³. It is understood that p0 is tougher on account of its larger polymer fraction providing superior energy absorption. Additionally, the trade-off between these augmentations and failure strain is not substantial, since p5CB30 fails at only 80% of p0’s maximum strain. In overview, loading a nematic elastomer with 30wt% 5CB yields a stiffer, tougher, and more resilient LCE possessing properties of smectic LCEs.

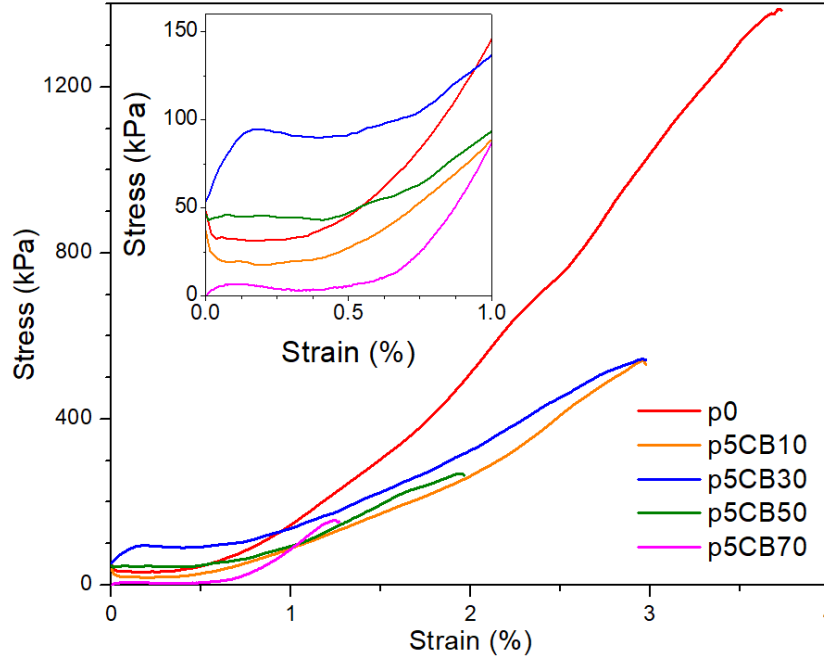


Figure 4-25: Overlaid Stress-Strain Data of all Polydomain 5CB Formulations.

Table 4-8: Comparison of Moduli between P0 and P5CB30. The failure strains for p0 and p5CB30 are 370% and 297%, respectively.

Modulus/formulation	E_{16} (kPa)	E_{100} (kPa)	$E_{failure}$ (kPa)
P0	31	144	1384
P5CB30	94	136	544

4.2.5.2 Polydomain LCE Stiffening with Liquid Inclusions

The enhanced mechanical properties between polydomain formulations returned us to the originally posed question of whether anisotropic liquids can be harnessed as a liquid inclusion to stiffen an anisotropic solid. The phase-separated 5CB regions detailed in section 4.2.4.4 are analogous to the liquid inclusion droplets contained within the compliant solid in Dufresne’s work. To stiffen the host matrix, droplets must be smaller than the elastocapillary length, γ , which is a ratio of the solid’s modulus to the liquid’s surface tension (0.03508 N/m at 31.5°C) (105). In the polydomain case, for phase-

separated regions of 5CB, $L < \frac{\gamma}{E} = \frac{.0351N}{31\text{ kPa}} = 1.13\mu m$. As the radii derived in section 4.2.4.4 yield a diameter of 43.2Å, we believe the stiffening enhancements can be attributed to the interfacial tension of these phase-separated regions alongside the expected stiffening endowed by higher order LC domains.

4.2.5.3 Choice of Monodomain Programming Strain

We wanted to study if the monodomain LCEs were also conferred with enhanced mechanical properties since soft actuator applications often involve monodomain LCEs (19, 99, 124, 125). This is because the shape change resulting from the order-disorder transition is larger in aligned LCEs, and they are stiffer than their polydomain counterparts on account of the polymer chains being globally aligned. As thiol-acrylate LCEs can be programmed via UV photopolymerization, characterization of the monodomain behavior first requires the selection of the strain at which to program the formulations. Since all 5CB formulations had their SEP terminate at a different strain value, and the SEP shows when the polydomain-monodomain transition (PMT) takes place, it was necessary to find the strain begetting this alignment. During WAXS tests, this was qualitatively explored by finding the strain at which each LCE became transparent by eye. However, this was not an exact measurement as it was done visually. A more quantitative measurement of the PMT is performed by using incident linearly polarized light in directions both parallel and perpendicular to the uniaxial strain in separate instances (100). Since mesogens are geometrically anisotropic, the polarized light's transmittance will change as they rotate with loading.

The evolution of transmittance with strain for light polarized parallel (T_{\parallel}) and perpendicular (T_{\perp}) to the stretch directions are shown below in Figure 4-26. Both transmission coefficients show that for high and low loadings of 5CB, the sharp increase in slope is at lower strains than moderate loadings (i.e., 30 and 50wt%). Competing alignment between loaded 5CB and LCE chains can justify why moderate loadings have larger onset strains for transmission. Also, the sharp increase in the perpendicular transmission coefficient's slope onsets at lower strains than the parallel one. Importantly, p5CB30 has the largest onset strain for transmission regardless of polarization, which is evidence for p5CB30 having LC domains with the highest energy barrier for reorientation. P5CB30 also has the largest difference in perpendicular and parallel transmission coefficient onsets. P5CB70 has the steepest increase in transmission since substantially less energy is required to reorient the majority fraction of liquid. This data comprehensively supports the qualitative examination obtained during WAXS studies

of the strain required for inducing the PMT. It also provides strains beyond which the formulations should be stretched and programmed to ensure a fully monodomain LCE is obtained.

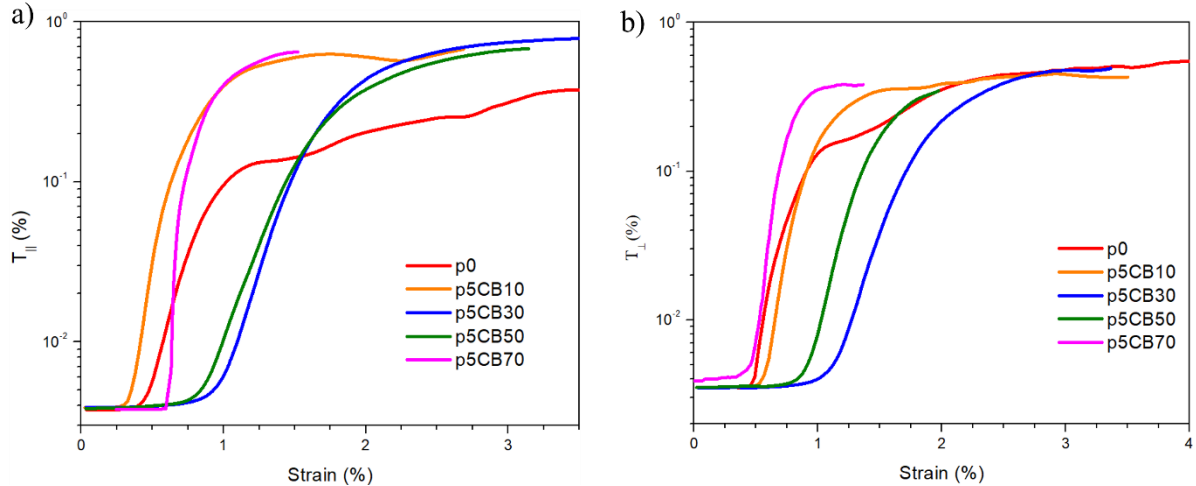


Figure 4-26: Transmission Coefficient Evolution with Strain.

Of noteworthy importance is how the strains used for WAXS differ from the strains measured here. The strain for the opaque-transparent PMT most closely resembles the transmission onset of light polarized parallel to the stretching direction. With this in mind, p5CB10 and p5CB30 were the only formulations where the strain for ensuring the WAXS sample was monodomain is in the transmission coefficients' plateaus. This initial observation may appear to be a major discrepancy since strain-induced cybotacticity is being claimed. However, this is not an issue since all 5CB-loaded formulations' WAXS profiles show the smectic pattern when strained. Moreover, in section 4.2.4 the peaks' d-spacings do not change beyond 40% strain, indicating that even though the p0, p5CB50, and p5CB70 LCEs were not in their fully monodomain state during WAXS per the transmission data, the smectic layering was still observed even if not fully monodomain. To remain relatively consistent with the strains used for WAXS, 235% was kept as the programming strain for p5CB30, while 194% was decided upon for p0. This decision for p0 was made since beyond that strain the parallel transmission coefficient roughly begins to plateau, just as with 235% in p5CB30.

4.2.5.4 Monodomain Tensile Tests

Knowing the threshold strains beyond which to polymerize the LCE formulations facilitated the creation of monodomain samples. At this point it was known with certainty that p5CB30 is the most

robust 5CB-doped formulation; it was only endeavored to create monodomain formulations of p5CB30 and p0 to study the highest degree of mechanical property enhancement. Fabrication of monodomain LCEs involved photopolymerizing the specimens with 365nm UV light at the selected strain value, which locked in this strained state through crosslinking the excess acrylate groups. As such, other loadings of 5CB—once programmed into their monodomain state—would not become more robust than the p5CB30 monodomain formulation. Monodomain p5CB30 was prepared by straining to 235% and the p0 was polymerized at 194%.

Tensile data was collected for loading directions both parallel and perpendicular to the director, and are shown in Figure 4-27a and Figure 4-27b respectively. Examining Figure 4-27a first, both curves show no signs of a PMT, confirming that they are entirely monodomain. M5CB30 has a markedly steeper linear elastic region mirroring the polydomain tensile data, and after yielding shows strain hardening until failure. P0's tensile data shows a similar linear region followed by an extremely short plastic deformation region. The two elastic moduli are 2.4MPa (m0) and 13.6MPa (m5CB30), representing a 570% increase. Also, the toughness values measured up until m5CB30's failure are 212 kJ/M³ (m0) and 788 kJ/M³ (m5CB30), representing a 372% increase. M0's toughness at its failure is 1929 kJ/M³. Considering the elastocapillary length for the monodomain LCEs, cybotactic 5CB regions must be below 14.6nm for liquid inclusion stiffening to be responsible, which is indeed the case for the calculated 5CB ellipsoids having a long axis of 14.5nm.

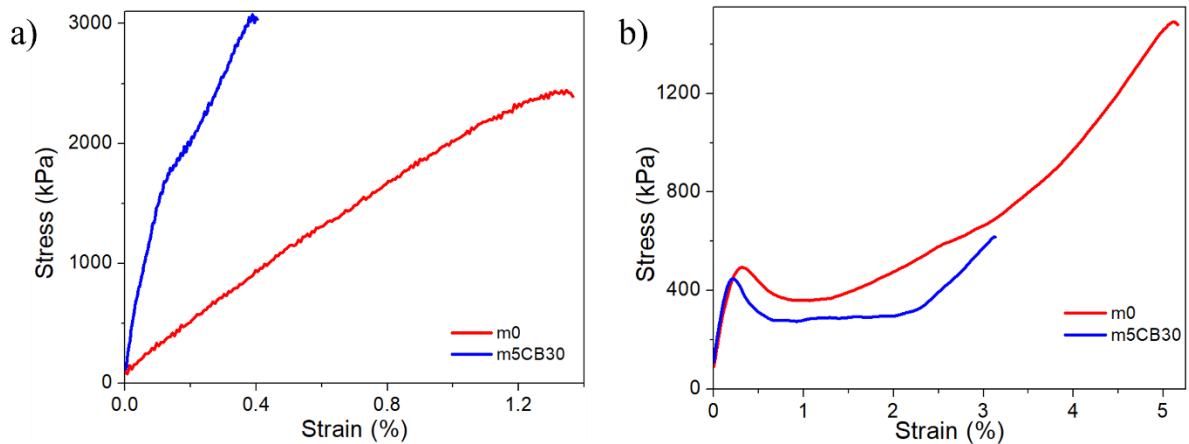


Figure 4-27: Monodomain Tensile Data for LCEs stretched a) Parallel and b) Perpendicular to the programmed Director.

Tensile data for stretching perpendicular to the director (Figure 4-27b) shows a yield point achieved in both formulations related to the stress required for domain realignment from the programmed director to the stretching direction. M0 having a larger yield point than m5CB30 implies that more loading is required to rotate aligned chains than a composite of aligned chains and LC solvent—even if cybotactic domains exist in the latter. Still, these yield strengths are not markedly different, with m0's being 494kPa and m5CB30's 448kPa. Both yield points are followed by a SEP demonstrating the mesogens rotating to becoming collinear with the stretching direction, and then subsequent strain hardening before failure. Such behavior parallels results seen in literature (126). M5CB30's longer SEP is understood to arise from the liquid fraction providing less resistance to LCE chain reorientation under zero stress, whereas m0's higher quantity of elastomer has more entanglements and crosslinked chains, which elicits more resistance to stress-free rotation.

4.3 Conclusions

In this chapter, a systematic study was conducted to determine how loading a liquid crystal solvent into a nematic liquid crystal elastomer modifies the phase behavior, molecular ordering, and mechanical properties. This action was implemented because it was hypothesized that an incorporated LC solvent could stiffen the host elastomer analogously to a liquid inclusion within a compliant solid. Particularly, if the LC solvent exists as phase-separated droplets within the LCE smaller than a critical length scale relating the host matrix's elastic modulus and the solvent's surface tension, the interfacial energy is substantial enough to increase the composite's elastic modulus. A stiffened LCE is captivating for soft actuator applications, where stiffness is correlated with eliciting a stronger contractile force.

This course of action was pursued by first selecting a thiol-acrylate LCE chemistry, which is already optimized for shape-programmability and ease of synthesis. Next, a liquid was chosen that has been documented to exist within LCEs in an immiscible state—particularly as phase-separated domains—and will not react with the LCE. LCEs polymerized with the chosen liquid, 5CB, were created with various loadings to systematically study 5CB's incorporation. First, the dopant's miscibility with the LCE was examined, which showed that though 5CB is miscible with its host matrix, there are possible signs of phase separation. Thermal analysis showcased the creation of a new mesophase below the neat LCE's nematic window that possessed more molecular order. The mesophase was revealed to have short-range smectic ordering, or cybotacticity, through WAXS and beget cybotactic ordering when

stretched. 30wt% loading of 5CB was found to be the optimal doping, showcasing the highest room temperature storage modulus and largest correlation lengths.

With the phase-separation criterion satisfied, the size of the phase-separated regions was calculated and found to be below the size scale recommended for liquid inclusion stiffening. By tensile testing the doped polydomain formulations, stiffening was demonstrated by the 30wt% loaded formulation compared to the undoped LCE. Using the neat elastomer's elastic modulus, the critical droplet size for stiffening was calculated. The cybotactic 5CB regions were three orders of magnitude smaller than the elastocapillary length required for stiffening, confirming that liquid inclusion stiffening is occurring. Monodomain tensile tests demonstrated both LCE stiffening (570%) and toughening (370%) up until m5CB30's failure strain, with the cybotactic domains' largest dimension being just below the elastocapillary length. Thus stiffening and toughening have both been achieved using a design strategy of liquid crystal inclusions.

Chapter 5

Smectogen Loaded Liquid Crystal Elastomers

The original hypothesis that spurred this work's research direction was if liquid inclusion stiffening can go beyond isotropic liquids in anisotropic solids to anisotropic liquids in anisotropic solids. By replacing dopants such as ionic liquids or eutectic indium gallium (E-GaIn) with liquids that have anisotropy both in their structure and molecular arrangement, will considerable improvements in stiffening occur? Myriad enhancements were granted by incorporating an unreactive LC solvent, 5CB, into the thiol-acrylate LCE, including considerable stiffening, toughening, and resiliency over the virgin LCE. These were due to the presence of liquid crystal inclusions. Intriguingly, phase-separated short-range smectic order (cybotacticity) is begotten from a nematogenic solvent and nematic elastomer that do not individually exhibit smecticity.

As such, it was desired to study what properties would be conferred through modification with an actual smectic-forming LC solvent, and if liquid inclusion stiffening was also observed. To ensure a relatively similar comparison and not warrant large experimental changes, 8CB was chosen for its nigh-congruent molecular structure with 5CB. Distinguished by only a propyl chain, it is also possible that 8CB can reside within the LCE in phase-separated domains just as with 5CB. 8CB's properties at room temperature are more complicated than its nematogenic analog; the additional smectic phase from 21-33.5°C means 8CB can exist in four physical states near ambient conditions (85). It is also extremely viscous at room temperature since its crystalline phase is up to 21°C. As such, it is essential to commence this investigation with how 8CB mixes with the LCE and if polymerizations proceed as expected.

5.1 Polymerization with 8CB

Differences from the neat LCE's 1st stage polymerization detailed in 4.2.1 are now discussed. Whereas 5CB was added with all monomers before dissolving in chloroform through heating, 8CB had to be incorporated after the monomers and inhibitor were dissolved. If added with the monomers and dissolved together, portions of the precursor mixture would prematurely gelate into a solid while the remainder dissolved. This effectively removed a substantial percentage of reactants from polymerizing inside the glass cell. Once dissolved into the isotropic state and allowed to cool down, the precursor mixture was clear and not viscous just as with 5CB loading. This mixture did not noticeably change

viscosity in the time between catalyst solution injection and cell infiltration, and residues outside the cell remained viscous for 2-3 days post-injection. 8CB-doped formulations were allowed to react for 48 hours before vacuuming to remove the chloroform and quench the reaction. Similarly to 5CB, the tested doping percentages were 10, 30, 50, and 70wt%.

Post-vacuuming, the 8CB-loaded LCEs with completed 1st stage polymerization were a cloudier and milkier white than the neat LCE—just as with 5CB loaded samples. No differences in appearance or manipulation with forceps existed between 8CB and 5CB-doped formulations except the following. Higher loadings of 8CB (p8CB50 and p8CB70) felt slippery and 8CB would readily come off the LCE surface upon contact with gloves or forceps. Comparatively, no 5CB loadings were this sebaceous. This phenomenon doubled as a qualitative test of 8CB leakage. P8CB70 visibly left greasy residues on its glass slide, and would not stick to forceps or glass slides when pressed by hand. Despite these qualitative differences, it was important to amass a more complete understanding of whether its interaction with the LCE resembled that of 5CB.

All 8CB formulations contained sufficient chain length for undergoing the polydomain-monodomain transition. Congruent with the 5CB-doped LCEs, the 30, 50, and 70wt% 5CB formulations initially resisted the applied stress but then stretched and retained their stretched length for small strains. The 10wt% loading (p8CB10) did not display this behavior.

5.2 Selection of Dopant Loading: Optimal Mechanical Properties

Rather than conducting a systematic study of 10, 30, 50, and 70wt% 8CB doped LCEs, it was decided to only study the loading that exhibited the most stiffening over the neat LCE. In the last chapter 30wt% was the optimal loading for 5CB; considering the similar molecular weight of 5CB and 8CB, it was hypothesized that 30wt% 8CB was also the optimal doping. Herein we discuss the polydomain tensile tests.

Polydomain specimens (n=4) of all 8CB formulations were tested the day after quenching until failure, at 23°C with the following stress-strain curves seen in Figure 5-1. A higher degree of replication was chosen in light of 8CB's demonstrated leakage from the LCE. A proportional dependence between strain hardening and the amount of 8CB loaded is observed alongside an inversely proportional relationship between failure strain and dopant loading. Both trends were also displayed by the 5CB formulation tensile tests (Figure 4-25). The key difference is all the 8CB formulations boast a linear elastic region, with p8CB30 and p8CB70 having the most prominent regions, followed by p8CB50 and

finally p8CB10 with the most gradual LER. Such behavior showcases the energy barrier for smectic domain rotation and corroborates the cybotactic nature of p5CB30. The measured elastic moduli are: 267kPa (p8CB10), 747 kPa (p8CB30), 318kPa (p8CB50), and 653 kPa (p8CB70), demonstrating p8CB30 and p8CB70 are stiffer than p5CB30. Another difference from the 5CB polydomain tensile data is the 70wt% formulation, p8CB70, demonstrating markedly steeper strain hardening than the 30wt% formulation. Enhanced strain hardening is due to the majority fraction of LC solvent contributing to considerably higher smecticity than p8CB30, such that for strains beyond where the small fraction of chains is already extended, the load is met with markedly larger resistance. Overall, Figure 5-1 confirms that the largest elastic modulus and toughness are both inherent to the 30wt% formulations of 5CB and 8CB loading. Recounting that both dopants differ only by a three-carbon chain, 30wt% of either LC solvent is a similar mole fraction of the LCE. Subsequent sections will only study p8CB30 against the optimal 5CB formulation (p5CB30) and the undoped LCE (p0) rather than a systematic study of all 8CB loadings. Such an analysis aims to assess the properties endowed from doping with an LC solvent having a room-temperature nematic or smectic phase.

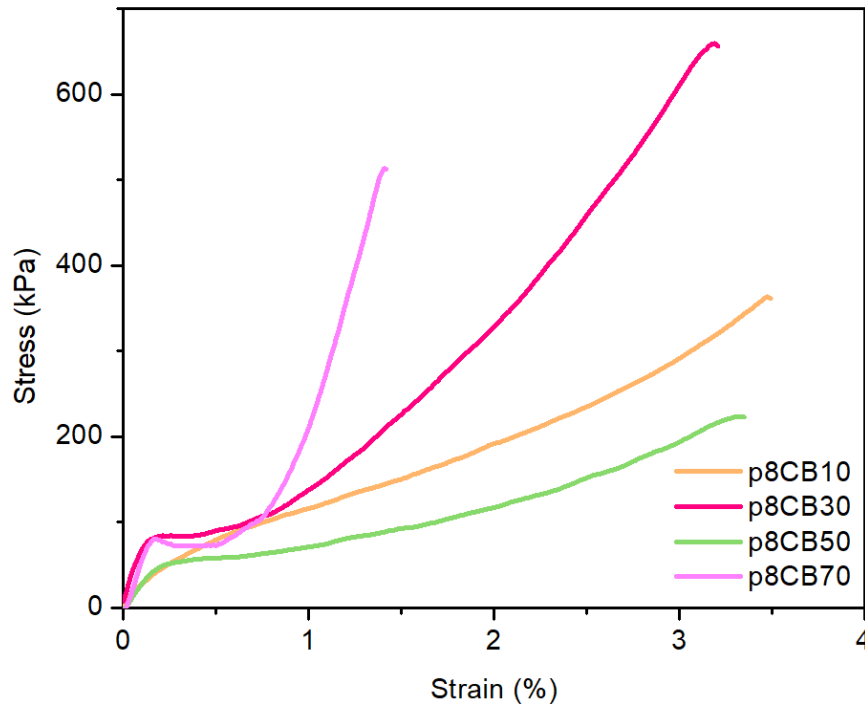


Figure 5-1: Polydomain Tensile test of 8CB-doped Formulations.

5.3 Miscibility

Just as demonstrated with 5CB, the miscibility will help gauge if 8CB satisfies the design criteria for liquid inclusion stiffening, whether through immiscibility with the LCE or by adopting phase-separated domains. In this section, 8CB's swelling behavior, surface energy relative to the neat LCE, solubility via GCT, and existence within the LCE via SEM are all studied. Dopant leakage is not studied as in the 5CB chapter since p8CB50 and p8CB70 formulations were already found to leak 8CB through residues left behind on gloves and trays after the polymerization. 8CB's contact angle with the LCE is not studied since its surface tension is already known, and γ considered alongside the LCE's surface energy is more comprehensive. Also, 8CB at ambient temperatures (22-25°C) is much too viscous to readily flow through the goniometer needle, and the goniometer setup did not allow for heating the 8CB to decrease its viscosity.

5.3.1 Swelling

The LCE's swelling behavior with 8CB was studied using a monodomain specimen of the neat LCE placed on top of a small pool (~0.1mL) of 8CB, and the ambient temperature was 23°C, indicating 8CB was in its smectic window. In Figure 5-2 we see the change in sample dimensions over 20 hours. Considerably less swelling occurred as compared to p0 in 5CB, with .7% and 1.6% length changes in directions parallel and perpendicular to the director, respectively. These values result in an equilibrium swelling degree of 1.02. This behavior can be attributed to 8CB being much more viscous than 5CB at the study temperature and perhaps that 8CB is less miscible with the LCE. 8CB's miscibility is examined in more detail in the next section. To determine if 8CB uptake perhaps occurred over a longer timescale the sample was left for another 20 hours. Noting that the LCE length changes were less than 0.1mm over the second 20-hour period, the length changes are considered marginal.

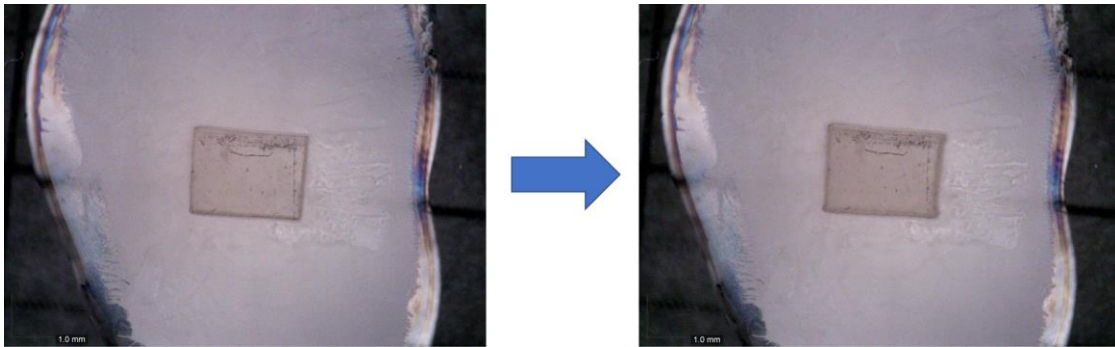


Figure 5-2: Digital Microscope Images of m0 before (left) and after (right) immersion in 8CB.

5.3.2 8CB Surface Energy and Group Contribution Theory

8CB's surface energy, γ_{8CB} , has been documented by Tintaru and colleagues at room temperature as $\sim 29.6\text{mN/m}$, which does not starkly contrast 5CB's of 35.1mN/m . Recalling from section 4.2.2.3 the calculated LCE surface energies from the Owens-Wendt (30.7mN/m) and Wu theories (34.5mN/m), 8CB's surface tension is quite similar, suggesting 8CB would readily wet the LCE surface if its viscosity was lower. Group contribution theory serves as a more informative comparison of the affinity between 8CB and the LCE matrix. Using the molar attractive coefficients reported by Small, 8CB's solubility parameter is detailed in Table 5-1 below (96). Being slightly larger than 5CB's, the solubility parameter confirms 8CB is less miscible with the LCE as was noted in the swelling experiments. Regardless, 8CB's solubility parameter is still sufficiently close to the LCE's δ to meet the cutoff criterion, indicating that the elastomer is miscible with 8CB.

Table 5-1: Solubility Parameters for 5CB, 8CB, and the LCE

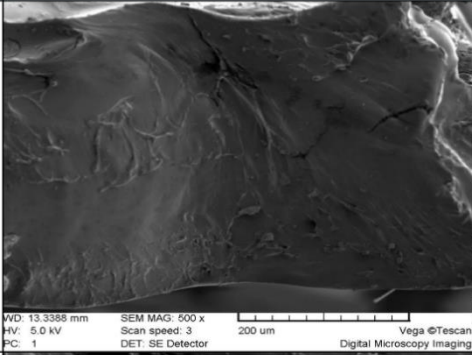
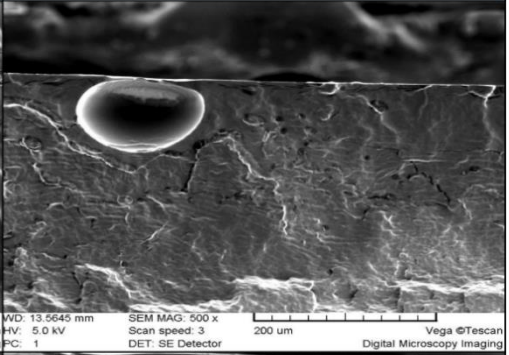
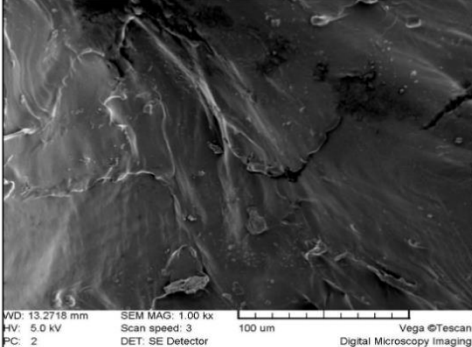
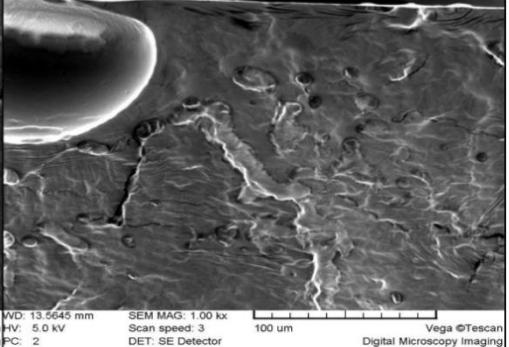
Component	$\delta_p (\text{cal} \cdot \text{cm}^{-3})^{.5}$	$\delta_s (\text{cal} \cdot \text{cm}^{-3})^{.5}$	$(\delta_s - \delta_p)^2$
LCE	9.52	-	-
5CB	-	10.01	0.24
8CB	-	10.1	0.33

5.3.3 Cross-Sectional Cryo-SEM

Cross-sectional SEM on cryo-fractured 8CB doped LCEs was only performed on specimens that had their LC solvent extracted before fracture. This was because a) the cryo-fractured 5CB samples that did not undergo extraction showed no evidence of phase separation, and b) samples that underwent extraction after fracturing were more likely to have collapsed voids at the cross-sectional interface due to capillary forces from solvent evaporation. As in section 4.2.2.5, 8CB was studied at optimal (p8CB30) and high (p8CB70) loadings. Table 5-2 below shows the secondary electron SEM images at $500\times$ and $1000\times$ magnification. Congruent to the 5CB-doped LCE SEM images are microscale lines in both formulations created from crack propagation during the fracturing process. However, the pattern of dark and light voids seen in p5CB70 was not observed in either 8CB formulation. Moreover, evidence of phase separation was not visible when the magnification was increased to $25000\times$ ($5\mu\text{m}$ scale). This absence suggests that the speckled pattern may not be indicative of cyanobiphenyl phase

separation from the LCE matrix. Curved features are observed in the top of p8CB70 images: the large ellipsoid in the top left is an air bubble, while the spheres to the right could perhaps be evidence of phase-separated regions. These features are only visible in this small area and do not pervade the LCE—just as with the speckled pattern in p5CB70—implying that such patterns may not be the strongest indication of phase separation. Notably, this does not detract from the existence of phase-separated LC solvent domains within the LCE. This is because it is plausible that 8CB at high loadings displays similar behavior to 5CB, where 8CB exists both as phase-separated regions and swells the LCE. It is anticipated that DSC, DMA, and WAXS data together will show signs of phase separation to a greater extent than 5CB. 8CB’s phase behavior within the LCE is examined more comprehensively in subsequent studies.

Table 5-2: SEM Images of p8CB30 and p8CB70 cross-sections at 500× and 1000× magnification

Formulation/ Magnification	p8CB30	p8CB70
500		
~1000		

5.4 Thermal Analysis

5.4.1 Differential Scanning Calorimetry (DSC)

As a starting point for probing the mesophase behavior endowed by doping with 8CB, we compare p8CB30's heat flow with the p5CB30—the optimal doping of 5CB—and p0, the control formulation. Using heating and cooling rates of 5°C/min, the results shown in Figure 5-3 were obtained. Just as in p5CB30, two endothermic peaks are recorded in p8CB30 above its T_g , though with more separation. These two transitions also resemble smectic-nematic LCE heat flows documented in literature (57, 59). P8CB30's glass transition occurs at a higher temperature than p5CB30's and is attributed to 8CB's larger intermolecular forces requiring more kinetic energy to facilitate chain movement.

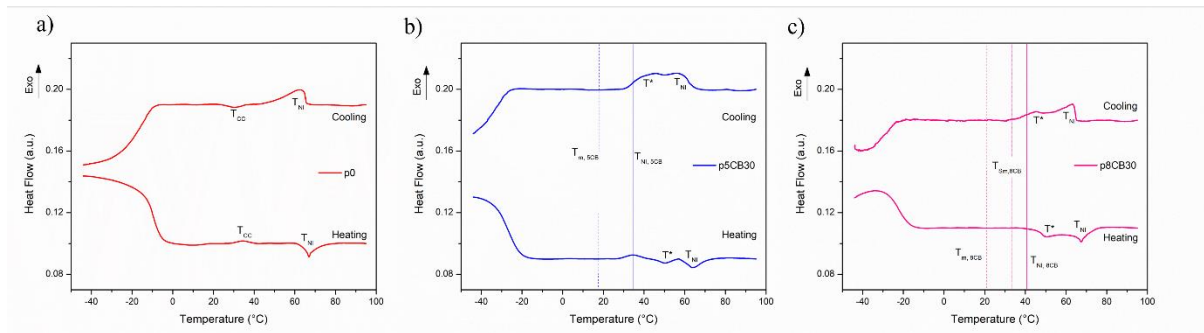


Figure 5-3: Heating and Cooling Cycles of a) p0, b) p5CB30, and c) p8CB30.

For clarity, p8CB30's higher temperature peak is called the primary peak, and the lower temperature transition is the secondary peak. The same naming convention will be used for p5CB30. Since p5CB30 and p8CB30's transitions occur at similar temperatures, the temperatures associated with each peak are tabulated below.

Table 5-3: Transition Temperatures of p8CB30 and p5CB30

	Heating		Cooling	
	T^* (°C)	T_{NI} (°C)	T^* (°C)	T_{NI} (°C)
p0	-	67	-	62
p5CB30	49	64	46	56
p8CB30	50	67	45	63

P8CB30 has a higher T_{NI} than both p5CB30 and the control LCE, which can be attributed to more thermal energy required for overcoming the greater intermolecular forces and dimeric nature of 8CB (85). However, the enthalpies for all p5CB30 transitions are larger than p8CB30's, indicating more heat must be absorbed to facilitate the order-disorder transitions. P8CB30's T^* is almost the same temperature as p5CB30's T^* (the cybotactic-nematic transition), and notably no peaks are detected at 8CB's transition temperatures just as with 5CB in p5CB30. The striking similarities in behavior to p5CB30 suggest that perhaps a similar mesophase exists from 8CB loading. As discussed before, cooling cycle transitions are expectedly shifted to lower temperatures due to their dependence on kinetics.

5.4.2 Dynamic Mechanical Analysis (DMA)

DSC data for p5CB30 and p8CB30 showed high-congruent transition temperatures between each formulation's T^* and similar ranges for T_{NI} . Consequently, Dynamic Mechanical Analysis was employed to better distinguish the transition temperatures of p8CB30 from its 5CB-doped analog. By testing polydomain specimens in triplicate, the following storage moduli and $\tan\delta$ data were obtained for p8CB30, and plotted against the p5CB30 and p0 for comparison in Figure 5-4 and Figure 5-5, respectively. The transition temperatures of 8CB and 5CB are also labeled on the relevant storage moduli curves to reinforce that the loaded LCE transitions do not coincide with those of the native dopant. P8CB30 displays steeper crystalline-amorphous transitions than p5CB30 at its T_g and T^* , which can be attributed to 8CB's smectic phase and higher intermolecular interactions. In stark contrast to p5CB30's behavior is p8CB30's mechanical property development in between T^* and T_{NI} as evidenced by the increase in E' between the two minima. An elevated rubbery plateau between T_g and T_{NI} is observed in p8CB30 compared to p5CB30 due to its higher degree of crystallinity at moderate temperatures.

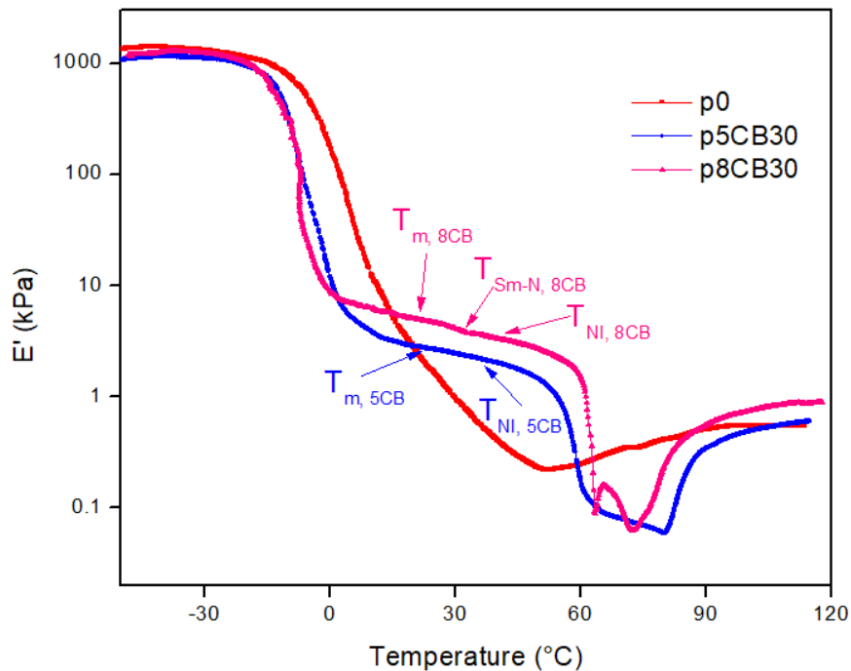


Figure 5-4: p0, p5CB30, p8CB30 temperature dependent storage moduli.

P8CB30's $\tan\delta$ graph, shown in Figure 5-5, displays much sharper peaks than p5CB30's transition temperatures, which is due to the higher degree of crystalline order loss at each transition. Concerning the transition temperatures, the displayed $\tan\delta$ curves show p5CB30 having a higher T_g and T_{NI} than p8CB30. Understanding that these displayed curves were from the trial that best represented the three replicates for each formulation, the average transition temperatures taken from $\tan\delta$ peaks are now discussed. Tabulated in Table 5-4, both p5CB30 and p8CB30 have congruent T_g and T_{NI} when measured to tenths of a degree (the instrument's resolution) (114). However, considering the larger standard deviation of p5CB30 specimens, p8CB30's T_g and T_{NI} are concluded to occur at higher temperatures than p5CB30. The transition temperature resemblance is perhaps attributed to the proximity of 5CB and 8CB's respective melting temperatures. The two T^* are distinct—with p8CB30's occurring at an elevated temperature—and T^* is associated with 8CB's additional mesophase. If p8CB30 also displays cybotactic ordering, the dopant possessing a smectic mesophase shifts the cybotactic-nematic transition to a higher temperature than p5CB30. Overall, 8CB's impact on increasing the LCE transition temperatures compared to 5CB stems from 8CB's enhanced intermolecular interactions and smecticity. Recalling how DMA provides a more precise measurement of amorphous-crystalline transition

temperatures than DSC due to larger changes in mechanical properties occurring as compared to heat capacity, there is greater confidence in the DMA measurements than those from DSC.

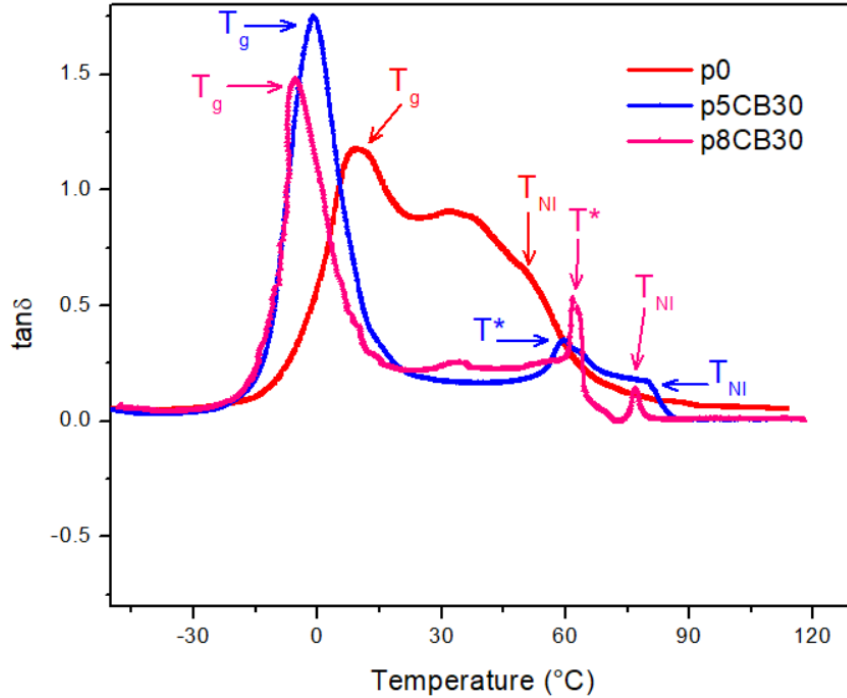


Figure 5-5: p0, p5CB0, and p8CB30 $\tan\delta$ with labeled T_g , T^* , T_{NI} .

Table 5-4: Transition Temperature Comparison for p8CB30 and p5CB30

	P5CB30			P8CB30		
	T_g (°C)	T^* (°C)	T_{NI} (°C)	T_g (°C)	T^* (°C)	T_{NI} (°C)
Average	-5.7	56.7	76.3	-5.7	62.1	76.3
Standard Deviation	4.00	4.46	3.56	1.25	2.48	1.62

5.4.3 Coefficient of Thermal Expansion

Recalling 8CB's additional smectic mesophase compared to 5CB, it was important to understand the influence higher order mesophases have on LCE thermal expansion. In kind with sections 5.4.1 and

5.4.2, only the optimal formulation of 8CB was tested, with the results shown in Figure 5-6. The strain chosen for monodomain programming of the 8CB formulation was 194% and is described in 5.6.2. Two slope changes are visible in m8CB30 and are labeled with vertical lines, mirroring the behavior of m5CB30 with T^* and T_{NI} . By comparing the neat LCE with the optimally loaded 5CB and 8CB formulations, a higher thermal barrier is required to onset thermal expansion/contraction for m8CB30. This observed behavior is expected due to 8CB's higher degree of molecular ordering. Interestingly, m8CB30's T^* is markedly elevated as a result of the secondary crosslinking masking the transition temperatures. This contrasts with m5CB30, where its T^* is close to that of p5CB30 measured in DSC or DMA. A higher onset temperature for length changes produces a faster expansion/contraction rate in m8CB30, though conversely, slightly smaller actuation strains are observed in m8CB30 than in m5CB30. Overall, the thermal analyses confirm the presence of a new phase that resembles the 5CB-doped LCEs' cybotacticity in both polydomain and monodomain formulations.

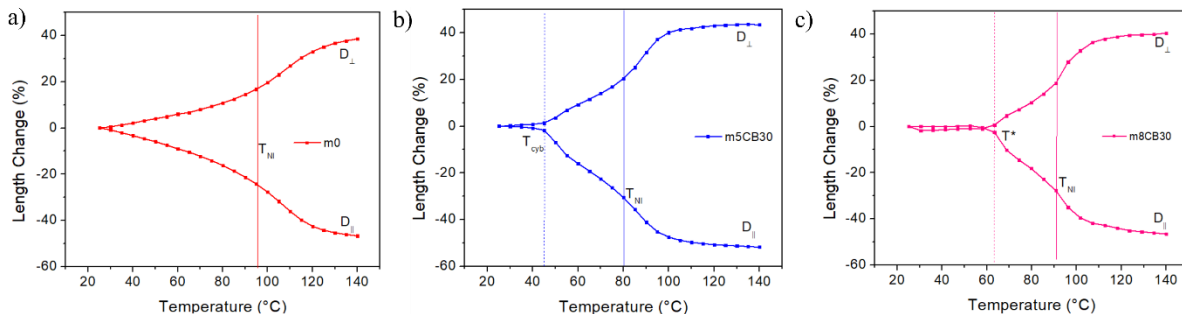


Figure 5-6: Thermal Expansion Graphs for 5CB0, m5CB30, and m8CB30 formulations. Length changes parallel (perpendicular) to the director are denoted as negative (positive) strains.

5.5 Investigating 8CB's Endowed Microstructure

The thermal analysis section described p8CB30's marked resemblance to p5CB30's DSC, DMA, and coefficient of thermal expansion data. DSC heat flows displayed a similar introduction of a new mesophase in the same temperature window as p5CB30's cybotactic window. Temperature sweep DMA confirmed a heightened rubbery plateau compared to the control, evidencing enhanced crystallinity in p8CB30. Thermal expansion data reveals that the new mesophase seen in p8CB30 is also retained after monodomain programming and an increased rate of thermal deformation. These high congruencies taken together with the dopant similarities suggest that perhaps p8CB30 has a similar

molecular arrangement in the studied temperature windows to p5CB30. To thoroughly study this inference, p8CB30's X-ray crystallography is studied.

5.5.1 WAXS and Order Parameter

Using the same instrument operating conditions as for the formulations studied in Chapter 4, p8CB30 was studied in the polydomain state (at 0% strain), at a strain consistent with the other formulations (50%), and the strain required for becoming fully transparent (185%). Figure 5-7 documents the 2D diffraction patterns and 1D radially integrated curves for p8CB30 alongside p0 and p5CB30's results from the last chapter. Each row of data corresponds to the aforementioned three strains, where the top row contains the polydomain data and the bottom the strain conditions for being monodomain. Concerning the polydomain data in Figure 5-7a and Figure 5-7d, p8CB30 displays two wide-angle rings/peaks stemming from disordered mesogens and chain extenders. P8CB30 does not display any small angle peaks in the polydomain state but shows a more gradual decline in the integrated curve's slope up to 0.6\AA^{-1} than the control. A higher degree of molecular ordering exists over this reciprocal space window, though it is insufficient for a new mesophase to exist. Effectively in the polydomain state, p8CB30 data resemble p5CB30, except p5CB30 has a more gradual decline between $0.1\text{-}0.5\text{\AA}^{-1}$ and a sharper nematic peak.

Upon straining p8CB30 to 50%, differing behavior is observed whereby more intense pseudo-Bragg peaks develop at the same q-space values than in p5CB30. The same naming convention observed in Chapter 4 is used for WAXS peaks, where ones relevant to mesogens are labeled p_1 ($\sim 0.17\text{\AA}^{-1}$), p_2 ($\sim 0.35\text{\AA}^{-1}$), and p_3 ($\sim 1.4\text{\AA}^{-1}$). Heightened intensities of p8CB30's p_2 suggest a greater degree of smectic A layering than p5CB30 since p_2 is a reflection of p_1 . This is expected to be due to 8CB's smecticity. p_3 is still widest for p8CB30 under strain, on account of this formulation containing the least amount of nematogen. As the LCEs are stretched to being fully monodomain, p8CB30's behavior is markedly different from p5CB30's as its small angle peaks become considerably more intense. This implies that superior smectic A ordering is exhibited by p8CB30, which is predicted to be due to 8CB's smectic nature. Since these small angle intensities are not seen in the control, it is proposed that 8CB begets these peaks. This implication could parallel p5CB30's behavior where the phase-separated cyanobiphenyl regions also adopt smectic-like arrangements—a notion further explored later through the d-spacing and correlation lengths. P8CB30's wide-angle peaks expectedly collapse due to strain-induced alignment of the LCE chains to become even sharper than the control's p_3 . The LCE stretching

direction relative to the 2D diffraction patterns is shown in the first column of Figure 5-7c and is the same as observed in Chapter 4. Together, WAXS patterns have shown that when straining p8CB30 SmA ordering is introduced to a higher degree.

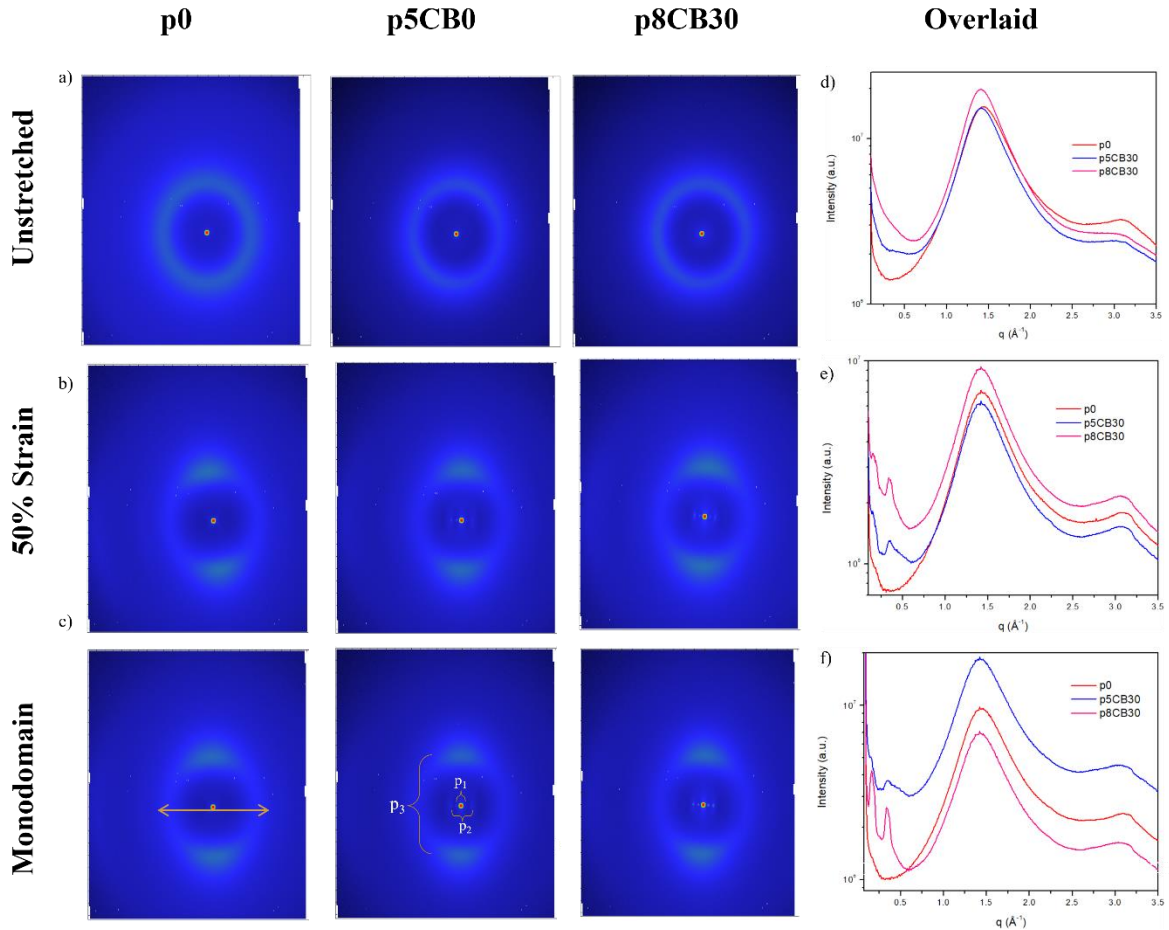


Figure 5-7: 2D Diffraction Patterns and 1D Radially Integrated Curves for p0, p5CB30, p8CB30.

The evolution of the p8CB30's orientational order parameter, S , is recorded in Table 5-5, with the values for p0 and p5CB30 borrowed from Chapter 4. P8CB30 also displays the smallest value for S in the polydomain state of all tested formulations. This is in analogy to p5CB30 having the smallest polydomain S value, where smectic regions not aligned with the director detract from the order parameter more than unaligned nematic regions. Smecticity is larger in p8CB30 than in p5CB30 and should yield a smaller polydomain order parameter. Through straining to 50% p8CB30's order

parameter increases to a lesser extent than the control or p5CB30, a trend likely due to the higher fraction of smectic domains having a larger entropy barrier to overcome for rotation and realignment (59). Only at high strains does p8CB30's order parameter become the second largest after p5CB30, exceeding the values of all 5CB formulations seen in Table 4-6. Smectic domains aligned with the director should reinforce the stretched LCE chains such that an augmented order parameter is observed. However, p5CB30's p_3 is still narrower on account of 5CB's nematicity. Overall it is observed that a higher degree of smecticity can reinforce chain alignment and give rise to a larger order parameter.

Table 5-5: Strain-Dependent Order Parameters for p0, p5CB30, and p8CB30

Formulation (Strain)	Column 1	Column 2	Column 3
p0 (0%, 50%, 60%)	0.34	0.64	0.63
p5CB30 (0%, 50%, 235%)	0.28	0.65	0.67
p8CB30 (0%, 50%, 185%)	0.14	0.62	0.66

5.5.2 D-Spacings and Correlation Length

Quantitative examination of p8CB30's x-ray patterns is necessary for a proper comparison with p5CB30's strain-induced cybotacticity. This will allow exact labeling of the endowed mesophase below p8CB30's nematic window. The same naming convention for d-spacings and correlations from Chapter 4 is employed here. For example, $\zeta_{p_3, p5CB30}$ refers to the correlation length of Peak 3 for p5CB30. The metrics for p8CB30, p5CB30, and p0 are seen in Table 5-6. Peak 2 is not included since it is a reflection of Peak 1—a characteristic that denotes multiple smectic layer stacking (118, 119).

P8CB30's polydomain p_3 has an associated d-spacing and correlation length of 4.5Å and 12.6Å respectively—values which are quite similar to those for p0 and p5CB30's third peak. The longer correlation length can be attributed to 8CB's increased van der Waal interactions resulting in transverse order over slightly larger distances. However, just as seen in Chapter 4, peak 3's correlation length remains between 11-12 Å as strain is developed. This correlation length is strain-independent since p_3 arises from the width of aromatic rings in RM257 (97). As p8CB30 is strained to 50%, Peak 1 develops with a d-spacing commensurate to p5CB30 and a correlation length 4 Å shorter. The smaller correlation length is understandable since a greater force is required to reorient 8CB's smectic domains. Once

stretched into an entirely monodomain state, p8CB30's correlation length increases to considerably more than 200Å. Such a larger correlation length is indicative of extensive smectic layering parallel to the stretch axis; the threshold energy barrier required for smectic domain reorientation with the stretching direction has been surpassed. This correlation length is thus understandably larger than $\xi_{1,p5CB30}$ at this strain value.

Considering p8CB30's d-spacing for Peak 1, this interlayer spacing has decreased below the 37-39Å range observed for all formulations. 36Å is remarkably close to the length of the 8CB dimer, implying that p8CB30's smectic layers are comprised of primarily 8CB dimers (127). 8CB is known to exist in a dimer conformation due to its strong cyano dipole and delocalized π orbitals, supporting this proposed smectic layer packing (120, 128). Moreover, the dimeric molecular arrangement is indicative of a special case of smectic ordering observed by 8CB called the smectic A_d (SmA_d) phase (25). Of intrigue was how the d-spacing decreases to such a value in p8CB30 but none of the 5CB loaded formulations. This is discussed in the upcoming section 5.5.3. Almost seven dimeric layers fit into p8CB30's monodomain correlation length, which is substantially greater than the smectic domains in p5CB30 observed (four stacked smectic layers). However, considering that fully-fledged smectic phases are seen to possess longitudinal correlation lengths more than 50× larger than the associated d-spacing, p8CB30 is demonstrative of short-range smectic—in essence, cybotactic—ordering within the nematic LCE (97, 122).

Table 5-6: D-spacing and Correlation Length Comparison for p8CB30, p5CB30, p0

	$d_{1,x}$ (Å)	$d_{3,x}$ (Å)	$\xi_{1,x}$ (Å)	$\xi_{3,x}$ (Å)	$\frac{\xi_{1,x}}{d_{1,x}}$	$\frac{\xi_{3,x}}{d_{3,x}}$
Polydomain (0% strain)						
p0	-	4.4	-	11.6	-	2.6
p5CB30	-	4.5	-	12.0	-	2.7
p8CB30	-	4.5	-	12.6	-	2.8
Stretched to 50%						
p0	-	4.5	-	10.9	-	2.4
p5CB30	39.0	4.5	101.3	11.3	2.6	2.5

p8CB30	38.6	4.5	97.0	11.5	2.5	2.6
	Stretched to Entirely Monodomain Strain					
p0	-	4.5	-	11.5	-	2.6
p5CB30	38.6	4.5	144.9	11.7	3.8	2.6
p8CB30	36	4.5	237.4	12.0	6.6	2.7

Overall, discussion of the x-ray scattering data for p8CB30, and comparison with p5CB30 has shown similar strain-induced cybotactic ordering, but with markedly larger longitudinal correlation lengths and a smaller interlayer spacing. These enhancements stem from 8CB's smecticity being responsible for the SmA_d ordering and larger correlation length than p5CB30's smectic regions.

5.5.3 FTIR-ATR

We aim to address differences in the smectic layer spacing between p5CB30 and p8CB30. Considering $d_{1,x}$ for all formulations, this d-spacing for 5CB doped formulations remained between 37-39Å, with no formulation's $d_{1,x}$ changing by more than 2 Angstroms. In contrast, $d_{1,p8CB30}$ decreased 2.6Å when stretched from 50 to 185% strain. Cyanobiphenyls that form a Smectic A phase are known to adopt bilayer structures due to the cyano group's strong dipole and steric ease of aromatic ring stacking (21, 25). In a separate vein, induced smectic phases are known to be stabilized by dipole-dipole interactions and charge transfer between electron-donating and withdrawing groups (129). Taken together, 8CB's dimeric nature may give rise to enhanced charge transfer interactions, which shorten the d-spacing compared to 5CB. Charge transfer in these LCEs would involve the cyano group functioning as a strong electron acceptor, and the LCE's phenyl rings serving as electron-donating groups. Charge transfer can be detected through reductions in the cyano group's stretching frequency through Fourier Transfer Infrared Spectroscopy with Attenuated Total Reflection (FTIR-ATR).

FTIR-ATR was performed on the control (p0), p5CB30, and p8CB30 in their polydomain and visibly monodomain states, and the wavenumber of the cyano group's stretch is recorded in Figure 5-8. P0 is shown as the reference spectra without any cyano group stretch. Comparing the change in labeled wavenumbers for ν_{CN} across the polydomain-monodomain transition (PMT), this frequency decreases by 1.63 cm⁻¹ and 3.61 cm⁻¹ for p5CB30 and p8CB30, respectively. P8CB30's cyano group absorbance frequency reduces more than double that of p5CB30, confirming larger charge redistribution in the 8CB

loaded formulation. This is because 8CB is more prone to close packing than 5CB since it has larger van der Waal interactions stemming from the longer alkyl chain. 8CB can more readily adopt the dimeric arrangement, producing stronger charge transfer and dipole-dipole/induced dipole interactions when compressed laterally from chain stretching. A shorter d-spacing is thus created, as seen with p8CB30's d-spacing (~the 8CB dimer, 36Å) contrasting p5CB30's d-spacing (~two 5CB molecular lengths, 38 Å).

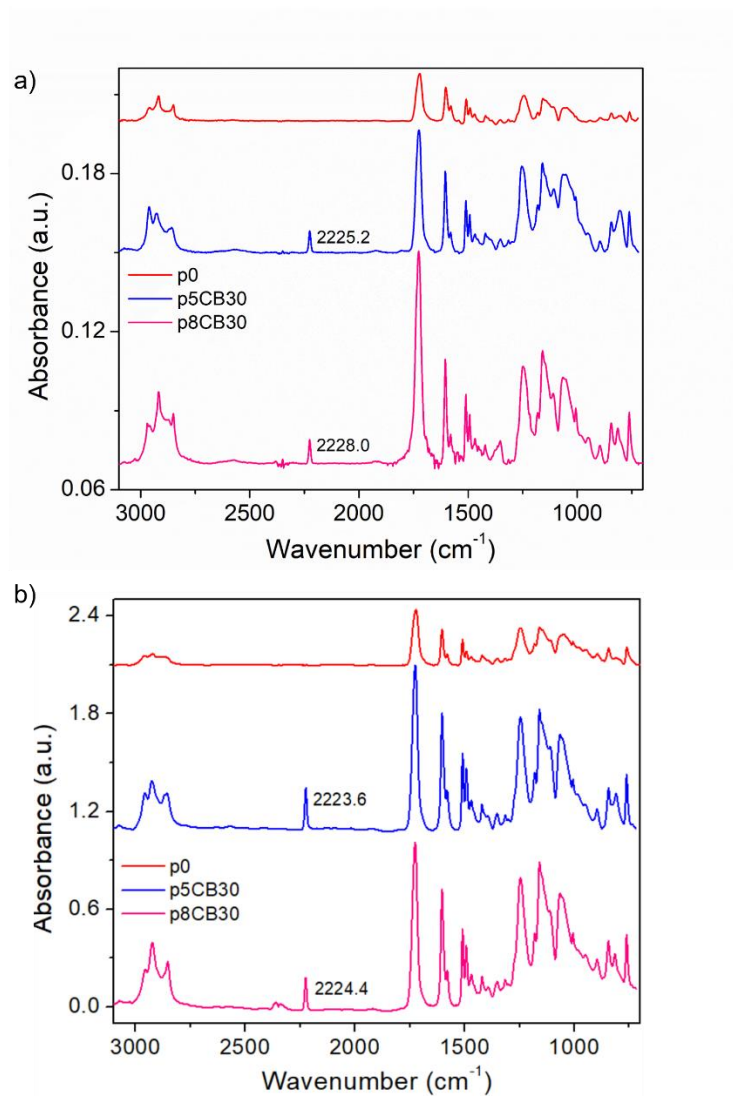


Figure 5-8: FTIR Spectra of a) Polydomain and b) Stretched to monodomain p0, p5CB30, p8CB30.

5.5.4 Size of Phase Separated Domains

So far p8CB30 bears remarkable similarity to p5CB30 in its induced mesophase structure, with the main difference being the longitudinal smectic layer spacing and correlation lengths. Since p8CB30 also shows phase separation, we strive to determine the size of these phase-separated short-range smectic domains through the same procedure in 4.2.4.4. Calculating the domain size can inform if liquid inclusion stiffening is possible, provided that these domains are below the elastocapillary length of 8CB for the neat LCE. This critical length scale that phase-separated regions must be below is 955nm, based on the 8CB's surface energy of 29.6mN/m and p0's initially measured elastic modulus from **Error! Reference source not found.** (31 kPa).

Back-calculating the phase-separated 8CB spherical domain size in the polydomain state yields $r_{poly,p8CB30} = 41.7\text{\AA}$. For the transformed domain in the monodomain state, $r_{mono,p8CB30} = 24.7\text{\AA}$ for the short axes of the ellipsoid, where $\zeta_{1,p8CB30}$ (237\AA) is the ellipsoid's long axis. Comparison with $r_{poly,p8CB30}$ (21.6\AA) and $r_{mono,p8CB30}$ (11.8\AA) shows that 8CB exists as larger phase-separated regions within the LCE.

To clarify 8CB's ordering in the polydomain and monodomain state, we build on Figure 4-19 by schematically showing the molecular arrangement in the two states within a cybotactic 8CB region. Below in Figure 5-9, polydomain and monodomain states of the bulk LCE are shown in Figure 5-9a and Figure 5-9b, respectively. Figure 5-9c and Figure 5-9d show the phase-separated 8CB domain elongation, and Figure 5-9e and Figure 5-9f depict the molecular arrangement with relevant dimensions labeled. Particularly, Figure 5-9e shows 8CB exists in its dimeric and single molecule conformation, and Figure 5-9f shows how lateral compression from chain elongation induces the adoption of the SmA_d mesophase.

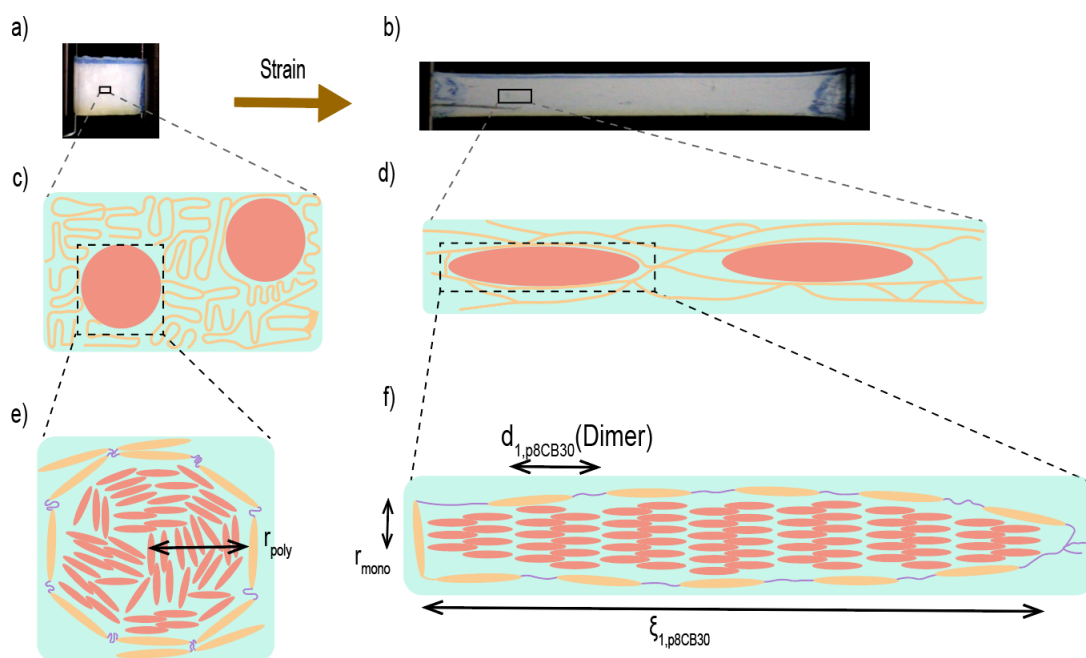


Figure 5-9: Strain-induced molecular packing schematic for p8CB30.

We briefly revisit the cryo-SEM image of p8CB70 in Table 4-3 and the possibility of the spherical features representing phase-separated 8CB. Just as with p5CB70, 8CB's miscibility with the LCE and its high loading percentage suggest that both swelling and phase separation occur. Together they beget the phase-separation evidenced by cryo-SEM and the nanoscale phase-separation of the 8CB domains.

5.6 Bulk Mechanical Properties

Returning to p8CB30's candidacy for the presence of liquid inclusion stiffening, the phase-separated regions of 8CB are considerably smaller than the 955nm elastocapillary length calculated in the last section. P8CB30's polydomain tensile test was introduced in Figure 5-1, where it was seen that one day after synthesis p8CB30 had a larger elastic modulus than what p5CB30 developed over seven days. Taken together, the interfacial tension of the phase-separated 8CB regions is not negligible and produces liquid inclusion stiffening similar to p5CB30. In this section, we examine how p8CB30's polydomain mechanical properties develop over time, and then compare them against p5CB30 and p0's optimal tensile data. We then study the evolution of p8CB30's transmission coefficients to determine the threshold strain beyond which the formulation is fully monodomain—this is necessary for designing a truly monodomain LCE.

5.6.1 Polydomain Tensile Property Evolution with Time

Figure 5-10 shows the time dependence of mechanical property development for five days commencing immediately after quenching and was tested at room temperature with $n=2$ trials per day. Evolution of the LER occurs within 48 hours for p8CB30, which is more rapid than that measured for p5CB30. The elastic modulus is similarly maximized five days afterward, mirroring the 5CB-loaded formulations. The parallelism is attributed to their small difference in molecular weight. We discuss differences between this test, and p8CB30's polydomain tensile test in section 5.2. While the current experiment shows the LER develops over 48 hours post-quenching, the polydomain tensile test in 5.2 demonstrated an LER the day after quenching. This is due to batch variability inherent to the polydomain LCE synthesis, just as discussed in section 4.2.5.1. Importantly, a steeper LER develops than in the optimally doped 5CB formulation and the neat LCE within a reasonable timeframe, producing a stiffened LCE.

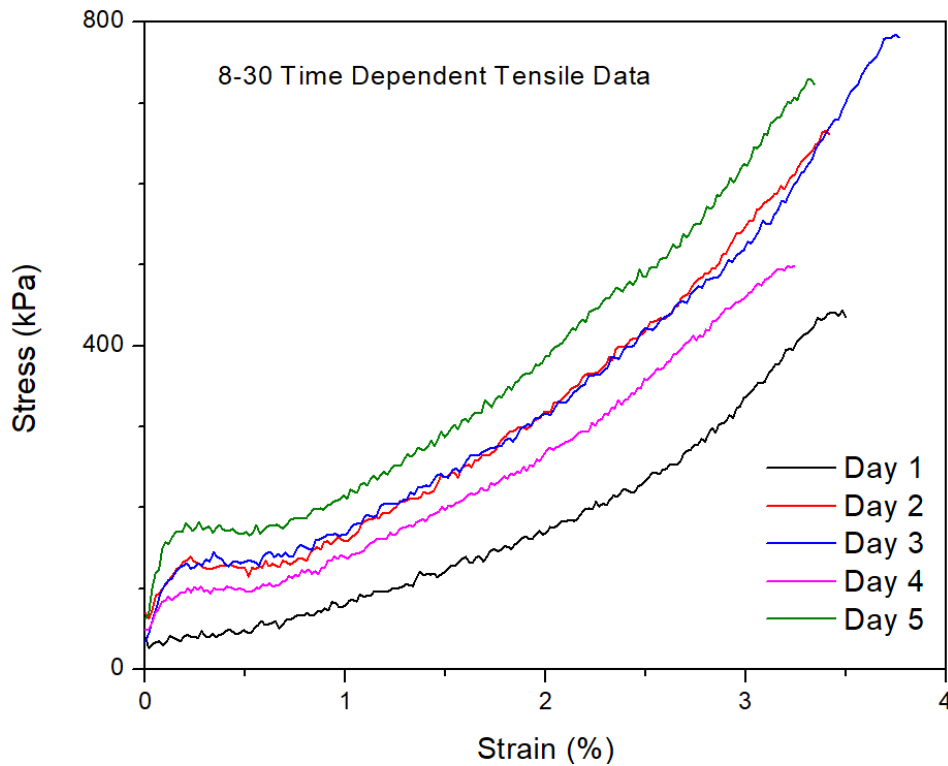


Figure 5-10: Five Day Polydomain Tensile Data of p8CB30.

Below the polydomain tensile data from day five are plotted for p8CB30, p5CB30, and p0. Alongside the elastic modulus of 413kPa for p5CB30 respectively, p8CB30's is recorded at 970 kPa. 8CB's smecticity engenders heightened charge transfer and dipole-dipole interactions, resulting in an LCE

with more than twice the stiffness brought about by 5CB. Additionally, 8CB endows the elastomer with greater extensibility as shown by the larger failure strain compared to 5CB. Analyzing p8CB30's toughness, we measure 1198 kJ/m³. At p8CB30's failure strain, p0's toughness is 1517 kJ/m³, and at its own failure strain, p0's toughness is 2035 kJ/m³. Batch variability is also present in p8CB30, yet the stiffening behavior provided by 8CB loading is always observed. Incorporating 8CB doubles the LCE's toughness, which is a similar margin to the augmentations by 5CB on the neat elastomer.

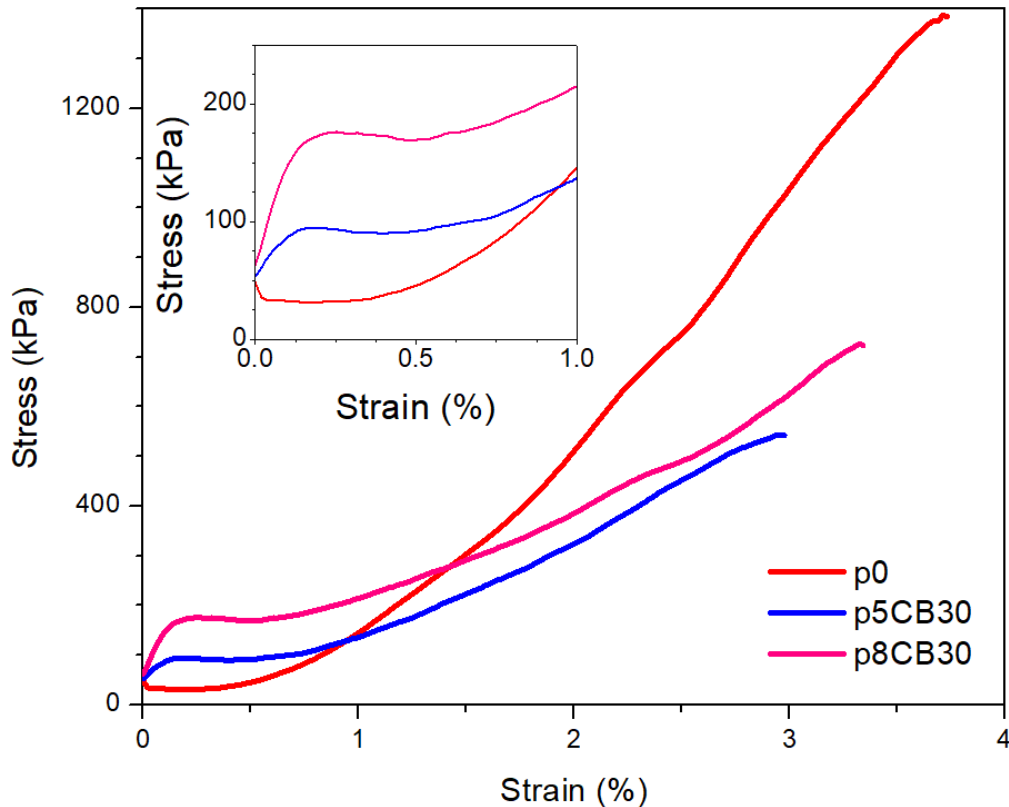


Figure 5-11: Polydomain Tensile Data from Day 5 for p8CB30, p5CB30, p0.

5.6.2 Polydomain-Monodomain Alignment Onset

To find the threshold strain beyond which p8CB30 was fully monodomain, the same transmission experiment from 4.2.5.3 was conducted. The transmission coefficients parallel and perpendicular to the stretch direction are shown in Figure 5-12 in solid and dashed lines, respectively. Compared with p5CB10 and p5CB30, p8CB30 displays even greater anisotropy in the onset of light transmission through the LCE. This phenomenon is due to 8CB-rich domains existing within the LCE as larger regions than 5CB in p5CB30 as calculated in 4.2.4.4 and 5.5.4. P5CB30 and p8CB30's transmission

anisotropy is contrasted by the control LCE, which is seen to have transmission onset at similar strains in both the parallel and perpendicular directions. The perpendicular transmission coefficient for p8CB30 was not observed to reach a plateau, unlike the other five curves. Programming p8CB30 beyond 96% strain would elicit a fully monodomain LCE. The failure strain for p8CB30 is smaller in this dataset than in the polydomain data—this is due to the inconsistent nature of how LC domains reorient. Since polydomain formation is a stochastic process, different batches of LCE will be polydomain to different extents, resulting in different degrees of domain rotation and extensibility. Considering this batch reached failure at lower strain values than the p8CB30 batch used for polydomain tensile tests, it was elected to program in a strain of 185% (i.e., where the parallel transmission coefficient begins its final plateau) to remain consistent with analyzed WAXS strains, and to ensure that the monodomain 8CB formulation was past the threshold 96% strain.

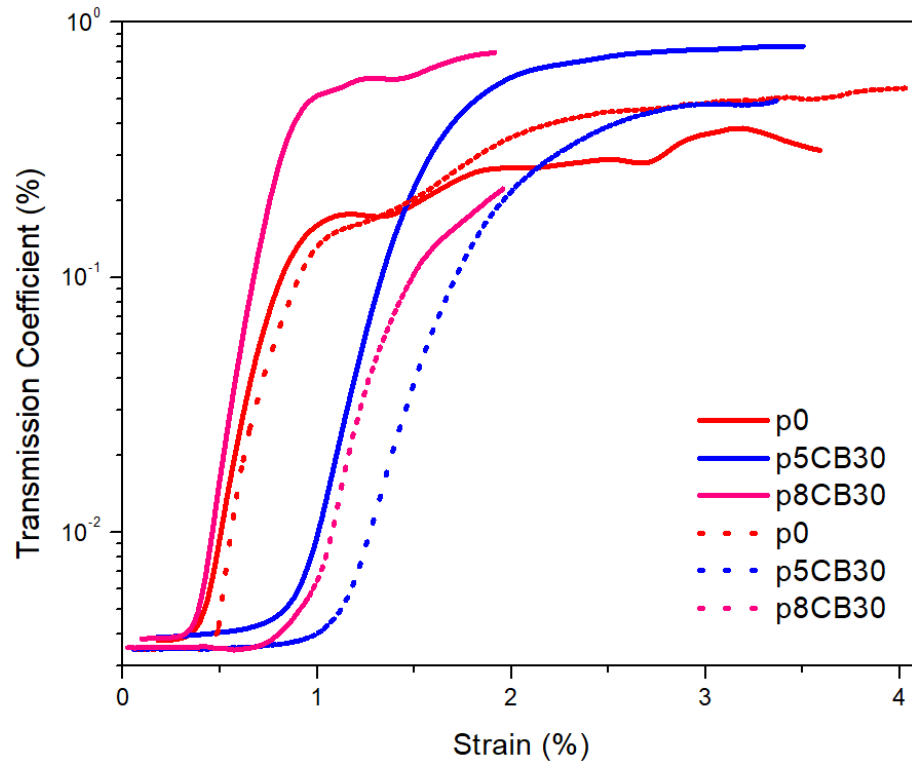


Figure 5-12: Strain Dependence of Transmission Coefficient. Solid (dashed) lines show the parallel (perpendicular) coefficients.

As before, it is important to detail how the strains used for WAXS differ from the transmission strains measured here. The strain for the opaque-transparent PMT most closely resembles the transmission

onset of light polarized parallel to the stretching direction. As such, p8CB30 was tested at a strain ensuring that during WAXS the formulation was fully monodomain. This is similar to the situation for p5CB30, where being strained to 235% was past the threshold strain for being fully monodomain. Therefore a like comparison was performed during WAXS between the two formulations.

5.6.3 Monodomain Tensile Tests

P8CB30's monodomain state was programmed in at 185% strain, the same value it was strained to in WAXS for monodomain onset. The monodomain tensile data for m8CB30, m5CB30, and m0 are graphed in Figure 5-13. For tensile tests conducted parallel to the director, m8CB30 has Young's modulus of 18.2MPa and toughness of 879kJ/m³, representing 758% and 415% increases compared to the control. As predicted, optimal doping with a smectic LC solvent generates mechanical properties outperforming those of the optimally doped nematogen-loaded LCE. The elastocapillary length for the undoped monodomain LCE—when 8CB is the dopant—is 12.3nm. Recounting that phase-separated 8CB droplets have their longest dimension 23.7nm, stiffening can be attributed to surface tension dominance since the sizes are of the same order in magnitude.

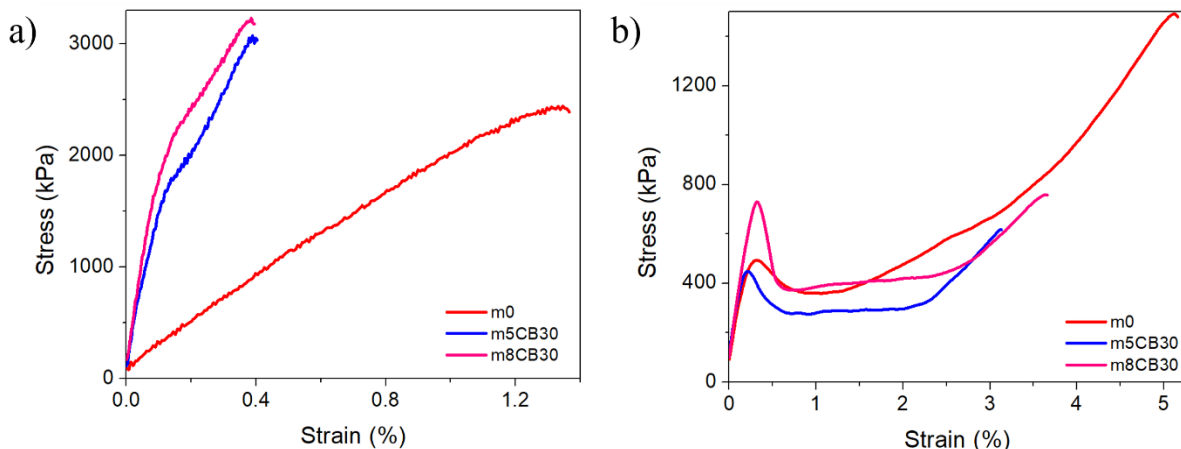


Figure 5-13: Monodomain Tensile Curves for m8CB30, m5CB30, m0

For tensile tests perpendicular to the director, a markedly larger energy barrier must be overcome for rotating the larger smectic domains observed in m8CB30 as seen through m8CB30's yield point in Figure 5-13b. M8CB30's yield point occurs at 727 kPa, whereas m5CB30's happens at 448kPa. Comparing these values sheds light on a trade-off between the lower energy barrier to reorient unreactive mesogens compared to polymerized ones, and the difficulty in rotating domains of higher

order. Seemingly, it is less energy-intensive to realign smectic domains on the order of 100Å than an equivalent weight percentage of aligned LCE chains—at least for the crosslinking density and composition in this work. However for smectic domains nearly double the size (200Å), a larger reorientation force is required than for an equivalent mass of LCE chains.

5.7 Conclusions

Motivated by the strain-induced cybotactic nature that occurs from doping a thiol-acrylate LCE with the nematogen 5CB, this Chapter studied how incorporating a smectic LC solvent, 8CB, modulates the LCE's properties. The dopant concentration that produces superior mechanical properties was discovered as being the same for both solvents (30wt%), a result attributable to their comparable molecular weights. Next, miscibility studies, thermal analysis, and x-ray crystallography showcased nigh identical phase behavior between the optimally loaded 5CB and 8CB LCEs. A similar cybotactic phase is developed below the LCE's nematic phase. In contrast to 5CB, uniaxially straining the LCE enhances the cybotactic nature considerably more to produce smectic A_d domains almost double the size of 5CB cybotactic domains. Nevertheless, these domains are sufficiently small such that their interfacial tension can stiffen the polydomain LCE comparable to a liquid inclusion. It was discovered that strain-induced charge transfer to the dopant cyano groups also manifests in both the 5CB and 8CB loaded LCE, which helps reinforce this higher order LC phase in conjunction with mechanical compression. Short-range SmA_d ordering gives rise to macroscopic stiffening (758%) and toughening (415%) of the polydomain and monodomain LCE beyond the enhancements demonstrated by 5CB-doped LCEs. The unique interplay of liquid crystal inclusions and strain-induced cybotacticity and charge transfer produces a considerably more robust LCE.

Chapter 6

Conclusion and Outlook

6.1 Conclusion

There is a continuously growing demand for soft-bodied robots because of their plethora of advantages over conventional rigid-bodied robots. Having a compliant body endows the robot with more degrees of freedom, better adaptability, and safer interaction with humans. Comparatively inferior mechanical properties are the principal drawback of soft robots, which are characteristics necessary for successfully performing effective work. As liquid crystal elastomers hold great potential for compliant body materials on account of their large, fast, and asymmetric actuation that is controllable through multiple stimuli, improving their mechanical properties has become the subject of intense research.

To improve their propensity for functional work, LCEs have been modified with solid fillers, interpenetrating polymer networks, crystallization techniques, and liquid metals. While these have augmented the stiffness, toughness, or actuation stress, such techniques generally diminish the liquid crystalline order responsible for their captivating actuation capabilities. Recently, a method for stiffening compliant solids through matching the elastic modulus with a liquid dopant's interfacial tension has been used to considerably enhance the LCE's work density. However, an isotropic liquid inherently obstructs mesogen packing. Could a liquid that did not obstruct orientational ordering such as a liquid crystal solvent function similarly to a liquid inclusion and markedly enhance the LCE's mechanical properties?

In this thesis, the development of an LCE stiffened toughened via liquid crystal inclusions is documented. This was accomplished through doping a thiol-acrylate nematic LCE with two ubiquitous LC solvent homologs—5CB and 8CB. A systematic study of modifications to the thermal properties, mechanical properties, and molecular ordering was conducted. It was discovered that the nematogenic 5CB fosters strain-induced cybotacticity and charge transfer within the LCE. Moreover, 5CB was revealed to phase separate from the network into droplets below the elastocapillary length required for liquid inclusion stiffening. The synergy amongst cybotacticity, charge transfer, and liquid crystalline inclusions resulted in the doped LCE being 570% stiffer and 370% tougher than the neat LCE while retaining 80% of the failure strain. These quantities were increased even further to stiffening by 760%, toughening by 415%, and retaining 90% of the neat LCE's extensibility by doping instead with the

smectogen 8CB. 8CB's smecticity ingrains the LCE with a more ordered smectic mesophase and heightened charge transfer beyond 5CB's endowments. Ultimately, strain-induced cybotacticity, strain-induced charge transfer, and liquid crystal inclusions represent a unique and robust three-pronged methodology to cultivate enriched mechanical properties.

6.2 Outlook

The utility of this cyanobiphenyl-loaded LCE can be studied for its ability as a soft robotic actuator beyond tensile tests and dynamic mechanical analysis conducted in this work. For stimuli-responsive actuation beyond thermoresponsiveness, such as through introducing light-responsive monomers (e.g., azobenzene derivatives or photothermal agents), it is important to analyze how incorporating such motifs modulates the mesophase behavior and intermolecular interactions. Such additives could disrupt the cybotactic domains. Considering aquatic robotic locomotion, both 5CB and 8CB having densities similar to water could dispose the higher loaded formulations to actuation in flooded environments. To examine particular use cases and environments, the strain-induced cybotacticity's dependence on loading rate could be an informative study to understand for which types of loadings this system is best suited.

An undesirable property of cyanobiphenyl incorporation into the LCE was the diminished failure strain compared to the control formulation. Methods for mitigating this trade-off between extensibility and toughness should be studied. Avenues applied to other polymers include the introduction of metal-ligand coordination chemistries and hydrogen bonding moieties. These strategies must be carefully tailored to mitigate adverse impacts on the three facets that stiffen and toughen the LCE.

References

1. A. M. Okamura, M. J. Matarić, H. I. Christensen, Medical and Health-Care Robotics. *IEEE Robotics & Automation Magazine* **17**, 26–37 (2010).
2. D. Duong, L. Vogel, Overworked health workers are “past the point of exhaustion.” *CMAJ* **195**, E309–E310 (2023).
3. G. R. Sutherland, P. B. McBeth, D. F. Louw, NeuroArm: an MR compatible robot for microsurgery. *International Congress Series* **1256**, 504–508 (2003).
4. What is da Vinci Robotic Surgery? A Complete Overview. Available at: <https://www.intuitive.com/en-us/patients/da-vinci-robotic-surgery> [Accessed 1 April 2024].
5. D. Rus, M. T. Tolley, Design, fabrication and control of soft robots. *Nature* **521**, 467–475 (2015).
6. C. Majidi, Soft Robotics: A Perspective—Current Trends and Prospects for the Future. *Soft Robotics* **1**, 5–11 (2014).
7. F. Hartmann, M. Baumgartner, M. Kaltenbrunner, Becoming Sustainable, The New Frontier in Soft Robotics. *Advanced Materials* **33**, 2004413 (2021).
8. T. J. White, D. J. Broer, Programmable and adaptive mechanics with liquid crystal polymer networks and elastomers. *Nature Mater* **14**, 1087–1098 (2015).
9. Y.-Y. Xiao, Z.-C. Jiang, Y. Zhao, Liquid Crystal Polymer-Based Soft Robots. *Advanced Intelligent Systems* **2**, 2000148 (2020).
10. C. M. Yakacki, *et al.*, Tailorable and programmable liquid-crystalline elastomers using a two-stage thiol–acrylate reaction. *RSC Adv.* **5**, 18997–19001 (2015).
11. D. P. Nair, *et al.*, The Thiol-Michael Addition Click Reaction: A Powerful and Widely Used Tool in Materials Chemistry. *Chem. Mater.* **26**, 724–744 (2014).
12. M. J. Ford, M. Palaniswamy, C. P. Ambulo, T. H. Ware, C. Majidi, Size of liquid metal particles influences actuation properties of a liquid crystal elastomer composite. *Soft Matter* **16**, 5878–5885 (2020).
13. Y. Li, H. Yu, K. Yu, X. Guo, X. Wang, Reconfigurable Three-Dimensional Messtructures of Spatially Programmed Liquid Crystal Elastomers and Their Ferromagnetic Composites. *Advanced Functional Materials* **31**, 2100338 (2021).
14. H. Kim, J. M. Boothby, S. Ramachandran, C. D. Lee, T. H. Ware, Tough, Shape-Changing Materials: Crystallized Liquid Crystal Elastomers. *Macromolecules* **50**, 4267–4275 (2017).

15. H.-F. Lu, M. Wang, X.-M. Chen, B.-P. Lin, H. Yang, Interpenetrating Liquid-Crystal Polyurethane/Polyacrylate Elastomer with Ultrastrong Mechanical Property. *J. Am. Chem. Soc.* **141**, 14364–14369 (2019).
16. R. W. Style, *et al.*, Stiffening solids with liquid inclusions. *Nature Phys* **11**, 82–87 (2015).
17. H.-F. Lu, *et al.*, An ultrahigh fatigue resistant liquid crystal elastomer-based material enabled by liquid metal. *Sci. China Mater.* **65**, 1679–1686 (2022).
18. R. A. M. Hikmet, From Liquid Crystalline Molecules to Anisotropic Gels. *Molecular Crystals and Liquid Crystals* **198**, 357–370 (1991).
19. H. Shahsavan, *et al.*, Bioinspired underwater locomotion of light-driven liquid crystal gels. *Proceedings of the National Academy of Sciences of the United States of America* **117**, 5125–5133 (2020).
20. P. J. Collings, M. Hird, *Introduction to Liquid Crystals: Chemistry and Physics* (CRC Press, 2017).
21. P. J. Collings, *Liquid Crystals: Nature's Delicate Phase of Matter* (Princeton University Press, 2002).
22. H. K. Bisoyi, Q. Li, Liquid Crystals: Versatile Self-Organized Smart Soft Materials. *Chemical Reviews* **122**, 4887–4926 (2022).
23. P. L. Praveen, D. P. Ojha, Role of molecular rigidity on phase organization of a smectic liquid crystal—A theoretical model. *Materials Chemistry and Physics* **126**, 248–252 (2011).
24. S. K. Prasad, Photostimulated and Photosuppressed Phase Transitions in Liquid Crystals. *Angewandte Chemie International Edition* **51**, 10708–10710 (2012).
25. G. W. Gray, J. W. G. Goodby, *Smectic Liquid Crystals: Textures and Structures* (Leonard Hill, 1984).
26. Y. Wang, J. Liu, S. Yang, Multi-functional liquid crystal elastomer composites. *Applied Physics Reviews* **9**, 011301 (2022).
27. G. Baxter, *et al.*, Highly programmable wavelength selective switch based on liquid crystal on silicon switching elements in *2006 Optical Fiber Communication Conference and the National Fiber Optic Engineers Conference*, (2006), p. 3 pp.-.
28. H. R. Morris, C. C. Hoyt, P. J. Treado, Imaging Spectrometers for Fluorescence and Raman Microscopy: Acousto-Optic and Liquid Crystal Tunable Filters. *Appl Spectrosc* **48**, 857–866 (1994).
29. Y.-H. Lin, Y.-J. Wang, V. Reshetnyak, Liquid crystal lenses with tunable focal length. *Liquid Crystals Reviews* **5**, 111–143 (2017).

30. V. I. Kopp, B. Fan, H. K. M. Vithana, A. Z. Genack, Low-threshold lasing at the edge of a photonic stop band in cholesteric liquid crystals. *Opt. Lett.* **23**, 1707 (1998).
31. J. M. Brake, M. K. Daschner, Y.-Y. Luk, N. L. Abbott, Biomolecular Interactions at Phospholipid-Decorated Surfaces of Liquid Crystals. *Science* **302**, 2094–2097 (2003).
32. B. H. Clare, N. L. Abbott, Orientations of Nematic Liquid Crystals on Surfaces Presenting Controlled Densities of Peptides: Amplification of Protein–Peptide Binding Events. *Langmuir* **21**, 6451–6461 (2005).
33. W. Pisula, M. Zorn, J. Y. Chang, K. Müllen, R. Zentel, Liquid Crystalline Ordering and Charge Transport in Semiconducting Materials. *Macromolecular Rapid Communications* **30**, 1179–1202 (2009).
34. J. Harden, *et al.*, Giant Flexoelectricity of Bent-Core Nematic Liquid Crystals. *Phys. Rev. Lett.* **97**, 157802 (2006).
35. J. P. F. Lagerwall, G. Scalia, A new era for liquid crystal research: Applications of liquid crystals in soft matter nano-, bio- and microtechnology. *Current Applied Physics* **12**, 1387–1412 (2012).
36. M. Nakata, M. Sato, Y. Matsuo, S. Maeda, S. Hayashi, Hollow fibers containing various display elements: A novel structure for electronic paper. *Journal of the Society for Information Display* **14**, 723–727 (2006).
37. W. J. Jackson JR., H. F. Kuhfuss, Liquid crystal polymers. I. Preparation and properties of p-hydroxybenzoic acid copolyesters. *Journal of Polymer Science Part A: Polymer Chemistry* **34**, 3031–3046 (1996).
38. J. F. D’Allest, *et al.*, Experimental Evidence of Chain Extension at the Transition Temperature of a Nematic Polymer. *Phys. Rev. Lett.* **61**, 2562–2565 (1988).
39. P. De Gennes, Réflexions sur un type de polymères nématiques. *CR Acad. Sci. Ser., B* **281**, 101–103 (1975).
40. H. Finkelmann, H.-J. Kock, G. Rehage, Investigations on liquid crystalline polysiloxanes 3. Liquid crystalline elastomers — a new type of liquid crystalline material. *Die Makromolekulare Chemie, Rapid Communications* **2**, 317–322 (1981).
41. M. Portugall, H. Ringsdorf, R. Zentel, Synthesis and phase behaviour of liquid crystalline polyacrylates. *Die Makromolekulare Chemie* **183**, 2311–2321 (1982).
42. J. Küpfer, H. Finkelmann, Nematic liquid single crystal elastomers. *Die Makromolekulare Chemie, Rapid Communications* **12**, 717–726 (1991).
43. M. Warner, E. M. Terentjev, *Liquid crystal elastomers* (Oxford University Press, 2003).

44. C. Ohm, M. Brehmer, R. Zentel, Liquid crystalline elastomers as actuators and sensors. *Advanced Materials* **22**, 3366–3387 (2010).
45. K. M. Herbert, *et al.*, Synthesis and alignment of liquid crystalline elastomers. *Nature Reviews Materials* **7**, 23–38 (2022).
46. D. L. Thomsen, *et al.*, Liquid Crystal Elastomers with Mechanical Properties of a Muscle. *Macromolecules* **34**, 5868–5875 (2001).
47. H. Yang, G. Ye, X. Wang, P. Keller, Micron-sized liquid crystalline elastomer actuators. *Soft Matter* **7**, 815–823 (2011).
48. C. L. Van Oosten, C. W. M. Bastiaansen, D. J. Broer, Printed artificial cilia from liquid-crystal network actuators modularly driven by light. *Nature Materials* **8**, 677–682 (2009).
49. M. O. Saed, *et al.*, Molecularly-Engineered, 4D-Printed Liquid Crystal Elastomer Actuators. *Advanced Functional Materials* **29** (2019).
50. M. Warner, P. Bladon, E. M. Terentjev, “Soft elasticity” — deformation without resistance in liquid crystal elastomers. *J. Phys. II France* **4**, 93–102 (1994).
51. C. Ortiz, M. Wagner, N. Bhargava, C. K. Ober, E. J. Kramer, Deformation of a Polydomain, Smectic Liquid Crystalline Elastomer. *Macromolecules* **31**, 8531–8539 (1998).
52. D. Mistry, *et al.*, Soft elasticity optimises dissipation in 3D-printed liquid crystal elastomers. *Nat Commun* **12**, 6677 (2021).
53. H. Shahsavan, L. Yu, A. Jákli, B. Zhao, Smart biomimetic micro/nanostructures based on liquid crystal elastomers and networks. *Soft Matter* **13**, 8006–8022 (2017).
54. M. O. Saed, A. H. Torbati, D. P. Nair, C. M. Yakacki, Synthesis of Programmable Main-chain Liquid-crystalline Elastomers Using a Two-stage Thiol-acrylate Reaction. *JoVE (Journal of Visualized Experiments)* e53546 (2016). <https://doi.org/10.3791/53546>.
55. C. E. Hoyle, A. B. Lowe, C. N. Bowman, Thiol-click chemistry: a multifaceted toolbox for small molecule and polymer synthesis. *Chem. Soc. Rev.* **39**, 1355–1387 (2010).
56. M. Barnes, R. Verduzco, Direct shape programming of liquid crystal elastomers. *Soft Matter* **15**, 870–879 (2019).
57. M. O. Saed, *et al.*, High strain actuation liquid crystal elastomers via modulation of mesophase structure. *Soft Matter* **13**, 7537–7547 (2017).
58. A. M. Martinez, M. K. McBride, T. J. White, C. N. Bowman, Reconfigurable and Spatially Programmable Chameleon Skin-Like Material Utilizing Light Responsive Covalent Adaptable Cholesteric Liquid Crystal Elastomers. *Advanced Functional Materials* **30**, 2003150 (2020).

59. H. Guo, M. O. Saed, E. M. Terentjev, Main-Chain Nematic Side-Chain Smectic Composite Liquid Crystalline Elastomers. *Advanced Functional Materials* **33**, 2214918 (2023).
60. K. R. Schlafmann, T. J. White, Retention and deformation of the blue phases in liquid crystalline elastomers. *Nat Commun* **12**, 4916 (2021).
61. M. del Pozo, L. Liu, M. Pilz da Cunha, D. J. Broer, A. P. H. J. Schenning, Direct Ink Writing of a Light-Responsive Underwater Liquid Crystal Actuator with Atypical Temperature-Dependent Shape Changes. *Advanced Functional Materials* **30**, 2005560 (2020).
62. R. H. Volpe, D. Mistry, V. V. Patel, R. R. Patel, C. M. Yakacki, Dynamically Crystallizing Liquid-Crystal Elastomers for an Expandable Endplate-Conforming Interbody Fusion Cage. *Advanced Healthcare Materials* **9**, 1901136 (2020).
63. T. Guin, *et al.*, Layered liquid crystal elastomer actuators. *Nat Commun* **9**, 2531 (2018).
64. T. Ohzono, Y. Norikane, M. O. Saed, E. M. Terentjev, Light-Driven Dynamic Adhesion on Photosensitized Nematic Liquid Crystalline Elastomers. *ACS Appl. Mater. Interfaces* **12**, 31992–31997 (2020).
65. N. A. Traugutt, *et al.*, Liquid-Crystal-Elastomer-Based Dissipative Structures by Digital Light Processing 3D Printing. *Advanced Materials* **32**, 2000797 (2020).
66. M. del Pozo, *et al.*, Patterned Actuators via Direct Ink Writing of Liquid Crystals. *ACS Appl. Mater. Interfaces* **13**, 59381–59391 (2021).
67. A. H. Gelebart, M. Mc Bride, A. P. H. J. Schenning, C. N. Bowman, D. J. Broer, Photoresponsive Fiber Array: Toward Mimicking the Collective Motion of Cilia for Transport Applications. *Advanced Functional Materials* **26**, 5322–5327 (2016).
68. J. Liu, *et al.*, Shaping and Locomotion of Soft Robots Using Filament Actuators Made from Liquid Crystal Elastomer–Carbon Nanotube Composites. *Advanced Intelligent Systems* **2**, 1900163 (2020).
69. R. Yadav, M. Singh, D. Shekhawat, S.-Y. Lee, S.-J. Park, The role of fillers to enhance the mechanical, thermal, and wear characteristics of polymer composite materials: A review. *Composites Part A: Applied Science and Manufacturing* **175**, 107775 (2023).
70. X. Liu, *et al.*, Reversible and Rapid Laser Actuation of Liquid Crystalline Elastomer Micropillars with Inclusion of Gold Nanoparticles. *Advanced Functional Materials* **25**, 3022–3032 (2015).
71. G. C. Lama, *et al.*, Controlled Actuation of a Carbon Nanotube/Epoxy Shape-Memory Liquid Crystalline Elastomer. *J. Phys. Chem. C* **120**, 24417–24426 (2016).
72. S. Courty, J. Mine, A. R. Tajbakhsh, E. M. Terentjev, Nematic elastomers with aligned carbon nanotubes: New electromechanical actuators. *EPL* **64**, 654 (2003).

73. Y. Yang, *et al.*, Graphene-Enabled Superior and Tunable Photomechanical Actuation in Liquid Crystalline Elastomer Nanocomposites. *Advanced Materials* **27**, 6376–6381 (2015).
74. Z. Li, *et al.*, Polydopamine nanoparticles doped in liquid crystal elastomers for producing dynamic 3D structures. *Journal of Materials Chemistry A* **5**, 6740–6746 (2017).
75. R. Annapooranan, Y. Wang, S. Cai, Highly Durable and Tough Liquid Crystal Elastomers. *ACS Appl. Mater. Interfaces* **14**, 2006–2014 (2022).
76. T. Ube, K. Minagawa, T. Ikeda, Interpenetrating polymer networks of liquid-crystalline azobenzene polymers and poly(dimethylsiloxane) as photomobile materials. *Soft Matter* **13**, 5820–5823 (2017).
77. T. Ube, K. Takado, T. Ikeda, Photomobile materials with interpenetrating polymer networks composed of liquid-crystalline and amorphous polymers. *J. Mater. Chem. C* **3**, 8006–8009 (2015).
78. X. Lin, W. Zou, E. M. Terentjev, Double Networks of Liquid-Crystalline Elastomers with Enhanced Mechanical Strength. *Macromolecules* **55**, 810–820 (2022).
79. Y. Deng, *et al.*, Interpenetrating Liquid Crystal Elastomer and Ionogel as Tunable Electroactive Actuators and Sensors. *Advanced Functional Materials* **n/a**, 2403892.
80. M. J. Ford, *et al.*, A multifunctional shape-morphing elastomer with liquid metal inclusions. *Proceedings of the National Academy of Sciences* **116**, 21438–21444 (2019).
81. J. Lee, S. Jung, W. Kim, Dependence of the effective surface tension of liquid phase eutectic gallium indium on wrinkles of the surface oxide. *Extreme Mechanics Letters* **48**, 101386 (2021).
82. Synthon Chemicals Liquid Crystals 2019. (2019).
83. J. P. F. Lagerwall, The good, the bad and the ugly faces of cyanobiphenyl mesogens in selected tracks of fundamental and applied liquid crystal research. *Liquid Crystals* **0**, 1–15 (2023).
84. M. Sadati, *et al.*, Molecular Structure of Canonical Liquid Crystal Interfaces. *J. Am. Chem. Soc.* **139**, 3841–3850 (2017).
85. A. J. Leadbetter, J. L. A. Durrant, M. Rugman, The Density Of 4 n-Octyl-4-Cyano-Biphenyl (8CB). *Molecular Crystals and Liquid Crystals* **34**, 231–235 (1976).
86. A. H. Gelebart, *et al.*, Photoresponsive Sponge-Like Coating for On-Demand Liquid Release. *Advanced Functional Materials* **28**, 1705942 (2018).
87. D. Mistry, *et al.*, Coincident molecular auxeticity and negative order parameter in a liquid crystal elastomer. *Nat Commun* **9**, 5095 (2018).
88. H. Wilderbeek, *et al.*, Photo-Polymerization of Liquid Crystalline Monomers in Anisotropic Solvents under Dynamic Conditions. *Jpn. J. Appl. Phys.* **41**, 2128 (2002).

89. I. Hegoburu, E. R. Soulé, Characterisation of polymerisation-induced phase separation process in polymer-dispersed liquid crystals based on hydroxyalkyl-methacrylate matrices. *Liquid Crystals* **44**, 1525–1533 (2017).
90. S. Wu, *Polymer Interface and Adhesion* (Routledge, 2017).
91. X. Xie, T. Gegenbach, H. Griesser, K. Mittal, Contact Angle. Wettability and Adhesion. *Utrecht, The Netherlands* (1993).
92. Surface Tension Components and Molecular Weight of Selected Liquids. Available at: https://www.accudynetest.com/surface_tension_table.html#007 [Accessed 7 July 2024].
93. R. Nasser Pourtakalo, Development and Characterization of Poly (lactic acid)/Acetylated Starch Blends. (2018).
94. D. K. Owens, R. C. Wendt, Estimation of the surface free energy of polymers. *Journal of Applied Polymer Science* **13**, 1741–1747 (1969).
95. S. Wu, Calculation of interfacial tension in polymer systems. *Journal of Polymer Science Part C: Polymer Symposia* **34**, 19–30 (1971).
96. P. A. Small, SOME FACTORS AFFECTING THE SOLUBILITY OF POLYMERS. *Journal of Applied Chemistry* **4**, 1–23 (1953).
97. F. Vita, *et al.*, Molecular ordering in the high-temperature nematic phase of an all-aromatic liquid crystal. *Soft Matter* **12**, 2309–2314 (2016).
98. C. R. Bridges, M. J. Ford, B. C. Popere, G. C. Bazan, R. A. Segalman, Formation and Structure of Lyotropic Liquid Crystalline Mesophases in Donor–Acceptor Semiconducting Polymers. *Macromolecules* **49**, 7220–7229 (2016).
99. L. Yu, *et al.*, Programmable 3D Shape Changes in Liquid Crystal Polymer Networks of Uniaxial Orientation. *Advanced Functional Materials* **28**, 1–8 (2018).
100. C. Luo, C. Chung, C. M. Yakacki, K. Long, K. Yu, Real-Time Alignment and Reorientation of Polymer Chains in Liquid Crystal Elastomers. *ACS Applied Materials & Interfaces* (2021). <https://doi.org/10.1021/acsami.1c20082>.
101. N. Lebovka, *et al.*, Low-temperature phase transformations in 4-cyano-4'-pentyl-biphenyl (5CB) filled by multiwalled carbon nanotubes. *Physica E: Low-dimensional Systems and Nanostructures* **52**, 65–69 (2013).
102. N. Bouchikhi, L. Alachaher-Bedjaoui, T. Bouchaour, G.-J. F. Tabieguia, U. Maschke, Experimental Study on the Swelling Behavior of Polymer Networks in a Nematic Solvent. *Macromolecular Symposia* **336**, 68–74 (2014).

103. N. Bouchikhi, F. Semdani, L. A. Bedjaoui, U. Maschke, Elaboration of Side-Chain Liquid-Crystalline Elastomers and Study of Their Swelling Behavior in Anisotropic Solvents. *Molecular Crystals and Liquid Crystals* **560**, 159–169 (2012).
104. Y. Yusuf, *et al.*, Swelling dynamics of liquid crystal elastomers swollen with low molecular weight liquid crystals. *Phys. Rev. E* **69**, 021710 (2004).
105. M. Tintaru, R. Moldovan, T. Beica, S. Frunza, Surface tension of some liquid crystals in the cyanobiphenyl series. *Liquid Crystals* **28**, 793–797 (2001).
106. T. Kamal, S.-Y. Park, A liquid crystal polymer based single layer chemo-responsive actuator. *Chemical Communications* **50**, 2030–2033 (2014).
107. N. A. Traugutt, *et al.*, Liquid-crystal order during synthesis affects main-chain liquid-crystal elastomer behavior. *Soft Matter* **13**, 7013–7025 (2017).
108. S. Li, *et al.*, Digital light processing of liquid crystal elastomers for self-sensing artificial muscles. *Science Advances* **7**, eabg3677 (2021).
109. H. Duran, B. Gazdecki, A. Yamashita, T. Kyu, Effect of carbon nanotubes on phase transitions of nematic liquid crystals. *Liquid Crystals* **32**, 815–821 (2005).
110. S. Ebnesajjad, “Chapter 4 - Surface and Material Characterization Techniques” in *Surface Treatment of Materials for Adhesive Bonding (Second Edition)*, S. Ebnesajjad, Ed. (William Andrew Publishing, 2014), pp. 39–75.
111. C. A. Mahieux, “2 - EFFECT OF TEMPERATURE ON POLYMER MATRIX COMPOSITES” in *Environmental Degradation of Industrial Composites*, C. A. Mahieux, Ed. (Elsevier Science, 2006), pp. 17–83.
112. A. Hotta, E. M. Terentjev, Dynamic soft elasticity in monodomain nematic elastomers. *Eur Phys J E* **10**, 291–301 (2003).
113. T. Ohzono, M. O. Saed, E. M. Terentjev, Enhanced Dynamic Adhesion in Nematic Liquid Crystal Elastomers. *Advanced Materials* **31**, 1902642 (2019).
114. T. Instruments, Dynamic Mechanical Analysis: Basic Theory & Applications Training. *TA Instruments* 85 (2018).
115. M. Zhang, *et al.*, Liquid-Crystal-Elastomer-Actuated Reconfigurable Microscale Kirigami Metastructures. *Advanced Materials* **33**, 2008605 (2021).
116. Y. Li, *et al.*, Multiscale Structural Characterization of a Smectic Liquid Crystalline Elastomer upon Mechanical Deformation Using Neutron Scattering. *Macromolecules* **54**, 10574–10582 (2021).

117. R. J. Mandle, S. J. Cowling, J. W. Goodby, Combined Microscopy, Calorimetry and X-ray Scattering Study of Fluorinated Dimesogens. *Sci Rep* **7**, 13323 (2017).
118. P. Figueiredo, W. Gronski, M. Bach, Preparation of Oriented Liquid-Crystalline/Isotropic Block Copolymer Films with Parallel or Perpendicular Arrangement of Smectic Layers and Lamellar Microdomains. *Macromolecular Rapid Communications* **23**, 38–43 (2002).
119. A. Gujral, *et al.*, Highly Organized Smectic-like Packing in Vapor-Deposited Glasses of a Liquid Crystal. *Chem. Mater.* **29**, 849–858 (2017).
120. M. Ruths, S. Steinberg, J. N. Israelachvili, Effects of Confinement and Shear on the Properties of Thin Films of Thermotropic Liquid Crystal. *Langmuir* **12**, 6637–6650 (1996).
121. N. I. Lebovka, *et al.*, Anomalous selective reflection in cholesteryl oleyl carbonate - nematic 5CB mixtures and effects of their doping by single-walled carbon nanotubes. [Preprint] (2013). Available at: <http://arxiv.org/abs/1303.0558> [Accessed 9 February 2024].
122. S. H. Hong, *et al.*, Short-range smectic order in bent-core nematic liquid crystals. *Soft Matter* **6**, 4819 (2010).
123. H. P. Patil, D. M. Lentz, R. C. Hedden, Necking Instability during Polydomain–Monodomain Transition in a Smectic Main-Chain Elastomer. *Macromolecules* **42**, 3525–3531 (2009).
124. H. Zeng, *et al.*, Light-fuelled freestyle self-oscillators. *Nature Communications* **10**, 1–9 (2019).
125. Y. Yu, M. Nakano, T. Ikeda, Photoinduced bending and unbending behavior of liquid-crystalline gels and elastomers. *Pure and Applied Chemistry* **76**, 1467–1477 (2004).
126. and M. S. Mingchao Zhang, Hamed Shahsavan, Yubing Guo, Abdon Pena-Francesch, Yingying Zhang, Liquid-Crystal-Elastomer-Actuated Reconfigurable Microscale Kirigami Metastructures. (2021).
127. J. Noh, B. Henx, J. P. F. Lagerwall, Taming Liquid Crystal Self-Assembly: The Multifaceted Response of Nematic and Smectic Shells to Polymerization. *Advanced Materials* **28**, 10170–10174 (2016).
128. T. A. Krentsel Lobko, O. D. Lavrentovich, S. Kumar, In-Situ X-Ray Measurements of Light-Controlled Layer Spacing in a Smectic-A Liquid Crystal. *Molecular Crystals and Liquid Crystals Science and Technology. Section A. Molecular Crystals and Liquid Crystals* **304**, 463–469 (1997).
129. S. Sugisawa, Y. Tabe, Induced smectic phases of stoichiometric liquid crystal mixtures. *Soft Matter* **12**, 3103–3109 (2016).